

ABSTRACT

FOSTER, RYAN DEAN. A Measurement of the Longitudinal Spin-Dependent Total Cross Section Difference, $\Delta\sigma_L$, in the $\vec{n} - \vec{d}$ System. (Under the direction of David G. Haase and Christopher R. Gould.)

Three recent experiments in the nd system, each with a different observable, have produced results that do not agree with theoretical predictions. The discrepancies have typically been ascribed to the poorly determined strength of the three-nucleon force. However, in the case of the recent high precision n-d scattering length measurement, the validity of some of the nucleon-nucleon force models has been questioned. To study these disagreements, we have initiated a program of measurements of the longitudinal spin-dependent total cross section difference, $\Delta\sigma_L$, using a polarized neutron beam and a polarized deuteron target for incident neutron energies of 1.18, 5.0, 6.88, and 9.0 MeV. Calculations have shown that $\Delta\sigma_L$ should be sensitive to the three-nucleon force.

We performed these measurements at Triangle Universities Nuclear Laboratory in Durham, NC. A polarized neutron beam was produced as a secondary beam from polarized proton or deuteron beams. The charged particle beams were created in the TUNL Atomic Beam Polarized Ion Source and were accelerated by a tandem Van de Graaff accelerator. The charged particle and neutron polarizations were determined from elastic scattering measurements.

The deuteron target was polarized via dynamic nuclear polarization. A ${}^3\text{He}$ - ${}^4\text{He}$ dilution refrigerator cooled the target to 250 mK and a superconducting magnet produced the 2.5 T magnetic field that is necessary to polarize the target. The target was irradiated with 69 GHz microwaves to achieve 20–30% polarization. The polarization was monitored by nuclear magnetic resonance and calibrated by reference to a $\Delta\sigma_L$ measurement at 1.18 MeV. The measurements of $\Delta\sigma_L$ show good agreement with potential models at 6.88 and 9.0 MeV neutron energy, indicating no large disagreements with theory. However, the results are not precise enough to rule out the presence or absence of three nucleon forces.

A MEASUREMENT OF THE LONGITUDINAL SPIN-DEPENDENT
TOTAL CROSS SECTION
DIFFERENCE, $\Delta\sigma_L$, IN THE $\vec{n} - \vec{d}$ SYSTEM

by
RYAN DEAN FOSTER

A dissertation submitted to the Graduate Faculty of
North Carolina State University
in partial fulfillment of the
requirements for the Degree of
Doctor of Philosophy

Department of Physics

Raleigh
2004

APPROVED BY:

Hugon Karwowski

Dean J. Lee

Werner Tornow

David G. Haase, Co-Chairman

Christopher R. Gould, Co-Chairman

In memory of my father

Larry Don Foster

1945–1997

Biography

Ryan Dean Foster

Personal

Born in Salisbury, NC, October 2, 1976

Married Amanda Jo Wagoner Rogers, May 26, 2001

Education

B.S. Physics, Western Carolina University, 1998

M.S. Physics, North Carolina State University, 2003

Thesis Title: *A Measurement of the Longitudinal Spin-Dependent Total Cross*

Section Difference, $\Delta\sigma_L$, in the $\vec{n} - \vec{d}$ System

Academic Positions

Teaching Assistant, NCSU, 1998–2001

Research Assistant, NCSU, 2001–2004

Memberships

American Physical Society

Publications

Contributed Abstracts

A Measurement of $\Delta\sigma_L$ in the $\vec{n} - \vec{d}$ System. R.D. Foster, C.R. Gould, D.G. Haase, J.H. Kelley, D.M. Markoff, and W. Tornow. 17th International IUPAP Conference on Few Body Problems in Physics, Book of Abstracts, 267 (May 2003).

Upgrade and Testing of the TUNL Dynamically Polarized Deuteron Target. R.D. Foster, D.G. Haase, C.R. Gould, D.M. Markoff, J.O. Poole, and W. Tornow. Bulletin of the American Physical Society **46**, 14 (2001).

An Upgrade of the TUNL Dynamically Polarized Deuteron Target. R.D. Foster, C.R. Gould, D.G. Haase, D.M. Markoff, J. Messimore, G. Palmquist, E. Pearson, J.O. Poole, and W. Tornow. Bulletin of the American Physical Society **44**, 11 (1999).

Co-Authored Abstracts

$\vec{n} - \vec{d}$ Scattering Measurements with the TUNL Dynamically Polarized Deuteron Target. D.M. Markoff, R.D. Foster, C.R. Gould, D.G. Haase, J.O. Poole, B.W. Raichle, and W. Tornow. Proceedings of the Ninth International Workshop on Polarized Sources and Targets, Nashville, Indiana (September 2001), 344. World Scientific, Singapore.

Oral Presentations

A Measurement of $\Delta\sigma_L$ in the $\vec{n} - \vec{d}$ System. R.D. Foster. Presented at the 15th National Nuclear Physics Summer School, Knoxville, TN (June 2003).

Acknowledgements

Writing these acknowledgements is something I have looked forward to for six years. For starters, it means I have finished my graduate studies and my dissertation, but most importantly, it gives me an opportunity to thank the people who have helped me get to this point. Without them, this dissertation would not have been possible.

I would first like to express my gratitude to Dr. David Haase for his guidance throughout my graduate studies. Despite being busy with the Science House, he was always willing to drop everything to help me and probably wishes that I had called him a little more than I did. He passed along not only his knowledge of physics, but also the professionalism that I hope to mimic in my career. Dr. Chris Gould shared his knowledge of nuclear physics and detectors and could always be counted on to find the silver lining in any situation. Dr. Werner Tornow could come into the control room and unfailingly find more beam hiding somewhere in the beam transport system. His assistance with the neutron polarimetry and the neutron production targets was also invaluable. I appreciate Dr. Dean Lee taking time out of his schedule to be on my committee and making the trip to Durham for my prelim and defense. I also want to thank Dr. Hugon Karwowski for agreeing to be a last minute addition to my committee.

This experiment could not have been performed without Drs. Diane Markoff and John Kelley. Dr. Markoff was an invaluable resource when I first joined the Polarized Target group. She guided me through the data acquisition software and electronics setup and could always be counted on to help set up for an experiment. Dr. Kelley graciously

joined our group for these experiments and agreed to work several overnight shifts. He also proved to be an expert at tuning beam.

The excellent technical staff at TUNL also deserves recognition. John Dunham kept the ABPIS running and could be counted on to give me grief when the target wasn't working. Richard O'Quinn and Paul Carter kept the accelerator in working order and Richard made sure I had liquid helium when I needed it. The Duke University Instrument Shop should be commended for its workmanship on the dilution refrigerator parts and various other projects that I brought to them. Bret Carlin and Sidney Edwards kept the data acquisition computers running and could be counted on to fix any problem I could throw at them. Pat Mulkey could find or build cables, rheostats, or anything else I was looking for.

Finally, I would not have been able to complete this degree without the love and support from my family. My parents provided the love and faith in me that are the foundation of my education. My mother has had to go it alone the last several years, but her support and strength have been unwavering. I only wish my father was here to share it with us. My brother Derek and his wife Jen have always been interested in how my research was going and I have truly enjoyed their friendship the last few years. My in-laws have accepted me into their family as one of their own and politely listened and nodded as I gave them a tour of the lab.

My wife Mandy has endured lonely nights at home, calls from the cryostat at 2 a.m., and has brought me supper at the lab too many times to count. I am not sure she knew what she was getting into when she married a graduate student pursuing a Ph. D. in experimental physics, but she has handled everything that has come her way with patience and understanding. She has brought so much love, laughter, and joy into my life and I couldn't have accomplished this without her.

Contents

List of Figures	x
List of Tables	xii
Chapter 1 Introduction	1
Chapter 2 Theory	4
2.1 The Spin-Dependent Total Cross Section	4
2.2 Polarized Neutron Beam Transmission	7
2.3 Polarized Neutron Transmission Measurement	9
2.3.1 Neutron Asymmetry Measurements	9
2.3.2 Beam Polarization Measurements	11
2.3.3 Deuteron Target Polarization Measurement	13
Chapter 3 Polarized Neutron Beam	14
3.1 The TUNL Atomic Beam Polarized Ion Source	14
3.2 Beam Acceleration and Transport	18
3.3 Proton Polarimetry	20
3.4 Neutron Production	22
3.5 Neutron Polarimetry	25

Chapter 4 Polarized Deuteron Target	27
4.1 Dynamic Nuclear Polarization	28
4.1.1 Theory	28
4.1.2 DNP Equipment	33
4.2 Dilution Refrigerator	34
4.2.1 Theory of Operation	34
4.2.2 ^4He Cryostat	36
4.2.3 Dilution Refrigerator Insert	38
4.2.4 Target Insert	39
4.2.5 Operating Procedures and Characteristics	41
4.3 Thermometry	42
4.4 Target Material	44
4.4.1 Target Material Batch Comparisons	44
4.4.2 Determination of Target Thickness	44
4.5 Nuclear Magnetic Resonance	46
4.5.1 Signal Acquisition	47
4.5.2 Shape Fitting and Signal Analysis	48
Chapter 5 Data Acquisition	52
5.1 Neutron Detectors and Electronics	52
5.1.1 Zero Degree Main Detector	52
5.1.2 Monitor Detector	53
5.2 Data Acquisition Electronics	54
Chapter 6 Data and Analysis	57
6.1 Beam Polarization	57
6.1.1 Proton Beam Polarization	57
6.1.2 Neutron Beam Polarization	59
6.2 Target Polarization	62

6.3 Neutron Asymmetries	64
6.4 Calculation of $\Delta\sigma_L$	67
Chapter 7 Summary and Discussion	72
Appendix A Nucleon-Nucleon Potential Models	74
Appendix B The Two-Pion-Exchange Three-Nucleon Force	81
Appendix C Proton Polarimetry Test	85
Appendix D The program npinit.com	86
Appendix E The program go.com	92
Appendix F The program neutasym.for	95
Bibliography	104

List of Figures

2.1	$\Delta\sigma_L$ predictions for the CD-Bonn NN Potential with and without the TM 3NF.[Wit99]	6
2.2	Schematic of the equipment used for the polarized neutron transmission experiment.	9
3.1	Schematic of the the TUNL Atomic Beam Polarized Ion Source.	15
3.2	Energy level splitting of the nuclear hyperfine states of hydrogen and deuterium atoms in a magnetic field.	16
3.3	The TUNL low-energy beam transport facility.	18
3.4	The TUNL high-energy beam transport facility.	19
3.5	The polarimeter scattering chamber	21
3.6	The deuterium gas cell neutron-production target.	23
3.7	The tritiated titanium neutron-production target.	24
3.8	The neutron polarimetry setup	26
4.1	Spin-temperature theory of dynamic nuclear polarization	31
4.2	Experimental ESR spectrum.	33
4.3	A simple dilution refrigerator.	35
4.4	The ^4He cryostat.	37
4.5	The target insert and dilution refrigerator insert	40
4.6	Calibration curve for the germanium resistance thermometer.	43

4.7	The TUNL polarized deuteron target NMR system.	47
4.8	Energy-level splitting of a deuteron in a magnetic field.	49
4.9	A plot of a typical NMR signal.	51
5.1	Online histograms of main and monitor detectors and BCI counts	56
6.1	Energy spectra for 2.52 MeV protons elastically scattered from ^4He	58
6.2	$K_z^{z'}(0^\circ)$ data from [Wal98]	59
6.3	Energy spectra for 6.88 MeV neutrons elastically scattered from ^4He	60
6.4	Comparison of $K_z^{z'}(0^\circ)$ values.	62
6.5	Plot of neutron asymmetry vs. BCI asymmetry	66
6.6	Plot of $\Delta\sigma_L$ vs. E_n	69
6.7	Plot of $\Delta\sigma_L$ vs. E_n	70
6.8	Plot of $\Delta\sigma_L$ vs. E_n	71
B.1	The two-pion-exchange 3NF force with a Δ isobar.	82
B.2	General two-pion exchange three-nucleon force.	83

List of Tables

3.1	Energy-loss calculations through the deuterium gas cell	23
3.2	Energy-loss calculations through the tritium foil	24
4.1	Typical operating parameters for the dilution refrigerator.	42
4.2	Values used in the calculation of the target thickness for each experiment. .	45
6.1	Proton beam polarimetry data.	58
6.2	Neutron polarimetry data.	61
6.3	Longitudinal neutron beam polarization calculations.	61
6.4	Calculation of spin temperature.	63
6.5	Calculation of NMR calibration constant	63
6.6	Calculation of average target polarizations for October experiment.	64
6.7	Summary of neutron asymmetry measurements.	64
6.8	Acceptable ranges for October 2003 data.	65
6.9	Neutron asymmetry data.	65
6.10	Calculation of $(\Delta\sigma_L)_C$	68
6.11	Calculation of $\Delta\sigma_L$	68
A.1	Summary of properties and predictions of NN interaction models	80
B.1	The cutoff parameter Λ used in the given potential combinations.	84

C.1 Proton-beam polarization measurements taken in the longitudinal orientation
during the $E_n = 1.18$ MeV experimental run in December 2003. 85

Chapter 1

Introduction

Many of the current nucleon-nucleon (NN) potential models describe neutron-proton and proton-proton scattering data with remarkable precision [Wit99]. However, when these potential models are used to calculate the binding energy of the triton, the predictions are 500-800 keV below the measured value of 8.48 MeV. Three-nucleon forces (3NF) correct the problem, but do not eliminate discrepancies in other 3 nucleon systems. For example, in N-d elastic scattering, the differential cross section minima are underpredicted by NN interactions starting at 60 MeV and extending to higher energies. Adding the 3NF fills up the minima, but does not eliminate the disagreement. This is known as the Sagara discrepancy [Wit98]. The analyzing power (A_y) calculated from NN potentials in neutron-deuteron scattering at low energies is also 25-30% too small. This is the so-called “ A_y puzzle”. Reasonable changes in the NN interaction and the inclusion of current three nucleon forces do not rectify the situation¹. Finally, in very precise measurements of the nd coherent neutron scattering length [Bla03], it was found that almost all theories were in disagreement with the experiment. It is clear from these disagreements between theory and experiment that the three body system is not well understood and that the current 3NF does not always correct apparent deficiencies in NN interactions.

¹However, new three body forces which have not yet been taken into account, such as the spin-orbit type, may resolve the disagreement [Hub98].

The investigation of the longitudinal spin-dependent total cross section difference, $\Delta\sigma_L$, was motivated by these discrepancies. $\Delta\sigma_L$ is the difference in the $\vec{n} - \vec{d}$ total cross section for spins parallel and anti-parallel to each other, with both spins aligned with the beam momentum axis.

The purpose of the present measurement was twofold. First, to confirm if standard NN interaction calculations were able to reproduce experimental values for $\Delta\sigma_L$ to an accuracy of order 10 to 20% , indicating no radical disagreements with the two-body calculations. And second, to see if a clear distinction could be made between calculations with and without 3NF effects. Theoretical calculations predict that the Tucson-Melbourne three-nucleon force ([Coo79] and [Coo81]) changes $\Delta\sigma_L$ by 5-10% [Wit99] from its value calculated using only NN interaction potentials. Early experiments at TUNL in 1998-1999 had indicated large discrepancies with all theories [Mar02] [Mar99], but were not considered definitive because of low polarization of the target and the lack of scattering measurement determinations of the target and beam polarizations.

To improve the reliability of the $\Delta\sigma_L$ measurements, a number of improvements were made to the experimental apparatus. The ^3He evaporation refrigerator used in 1998/99 was converted to a dilution refrigerator in order to achieve lower target temperatures and higher target polarizations. The NMR system, which is used to measure target polarization, was improved in order to increase the signal to noise ratio and modified to measure directly the deuteron NMR signal and polarization. The target material used was fully deuterated 1,2-propanediol D8 as opposed to partially deuterated D6, providing a higher deuteron concentration and target thickness. Finally, $\Delta\sigma_L$ was measured relative to a low energy value based on the average of a set of calculations made with and without 3NF effects.

This thesis reports measurements of the spin-dependent neutron transmission asymmetry for neutron energies of 1.18, 5.0, 6.88, and 9.0 MeV. By comparison to theoretical values of $\Delta\sigma_L$ at low energies, the 1.18 MeV asymmetries were used to calibrate the nuclear magnetic resonance measurement of the deuteron target polarization. Then $\Delta\sigma_L$ was calculated from transmission asymmetries for neutron energies of 5.0, 6.88, and 9.0 MeV and

was compared to theoretical predictions.

The following chapters discuss in greater detail each aspect of the experiment. Chapter 2 contains the theoretical formalism behind the measurements. The derivation of the expression for $\Delta\sigma_L$ is shown and the theory of the measurement is explained. Chapter 3 describes the production and transport of the polarized charged particle beam and the neutron production reactions. Beam polarimetry is also discussed. The polarized deuteron target is discussed in detail in Chapter 4. The theory of dynamic nuclear polarization and the necessary equipment are described. Testing of the new ^3He - ^4He dilution refrigerator is also covered. Chapter 5 contains the experimental procedure, including the neutron detection and data acquisition electronics. The data and analysis are presented in Chapter 6 and a summary in Chapter 7.

Chapter 2

Theory

This chapter provides the theoretical framework for the determination of $\Delta\sigma_L$, concentrating mainly on scattering theory and the theory of the measurement. An in-depth discussion of the meson-exchange nucleon-nucleon (NN) potential models, their properties, and their predictions of the triton binding energy is found in Appendix A. The two-pion exchange three-nucleon force and its effect on the triton binding energy are discussed in detail in Appendix B. Section 2.1 of this chapter examines the spin-dependent total cross section. Section 2.2 describes the transmission of a polarized neutron beam through a polarized target and contains the derivation of $\Delta\sigma_L$. This chapter concludes with the theory of the measurements that were required for the determination of $\Delta\sigma_L$. Section 2.3.1 contains the discussion of the neutron transmission asymmetry measurements and Section 2.3.2 describes the beam polarization measurements. Finally, the measurement of the deuteron target polarization is found in Section 2.3.3.

2.1 The Spin-Dependent Total Cross Section

Experimental data have shown that the nucleon-nucleon (NN) interaction has a tensor component [Wal98]. The existence of the tensor part of the NN interaction means that the nuclear potential contains non-central terms, so the spins of the particles must

be included when deriving the total cross section. The orbital angular momentum ℓ is no longer conserved when both particles have spin. The conserved quantity for the interaction between two particles with spin is \vec{J} , the total angular momentum, which is given by

$$\vec{J} = \vec{\ell} + \vec{I}_a + \vec{I}_A = \vec{\ell} + \vec{s} \quad (2.1)$$

where $\vec{I}_{a(A)}$ is the projectile (target) spin and \vec{s} is the channel spin.

The optical theorem relates the total cross section σ_T to the forward elastic scattering amplitude $f_{m'M',mM}(\theta = 0)$ by

$$\sigma_T = 4\pi\lambda Im \sum_{mm'MM'} \rho_{mm'} \rho_{MM'} f_{m'M',mM}(0^\circ) \quad (2.2)$$

where λ is the reduced wavelength, $\rho_{mm'}$ and $\rho_{MM'}$ are the density matrices of the projectile and target nuclei [Hni94] and the primes represent the final states. The polarization states of the beam and target can be described by statistical tensors calculated in the “spin-axis” coordinate system rather than density matrices [Sat83] and the total cross section is (following the derivation in [Kei94])

$$\sigma_T = \sum_{kK} \sigma_{kK} \tilde{t}_{K0}(I_A) \tilde{t}_{k0}(I_a) \quad (2.3)$$

where

$$\begin{aligned} \sigma_{kK} = & \frac{2\pi}{k^2} Re \left\{ \sum_J \sum_{\ell\ell'} \sum_{ss'} \sum_q \frac{2J+1}{(2I_a+1)(2I_A+1)} F_q(J\ell s\ell' s') \right. \\ & \left. \times [\delta_{\ell\ell'} \delta_{ss'} - S_{\ell s\ell' s'}^J] C_{Kq}^*(\beta_A, \phi_A) C_{kq}(\beta_a, \phi_a) \right\} \end{aligned} \quad (2.4)$$

are the partial-wave cross sections summed over the initial and final states. The $C(\beta, \phi)$ terms are geometric terms specifying the orientation of the spin axes and β and ϕ are the polar and azimuthal angles of the spin axis, respectively. The scattering amplitudes F_q are

$$\begin{aligned} F_q(J\ell s\ell' s') = & \sum_{\Lambda} (-1)^K (-1)^{(J-s')} \hat{\Lambda} \hat{I}_a \hat{I}_A \hat{\ell} \hat{\ell}' \hat{s} \hat{s}' \hat{k} \langle \Lambda k 0 q | K q \rangle \\ & \times \langle \ell' \ell 0 0 | \Lambda 0 \rangle W(s' s \ell \ell', \Lambda J) \begin{Bmatrix} I_a & s & I_A \\ I_a & s' & I_A \\ k & \Lambda & K \end{Bmatrix} \end{aligned} \quad (2.5)$$

where the terms in angular brackets are Clebsch-Gordon coefficients, $W(s's\ell\ell', \Lambda J)$ is a Racah angular momentum coupling coefficient, $\vec{\Lambda}$ is the angular momentum transfer, $\vec{\Lambda} = \vec{\ell}' - \vec{\ell}$, and the expression in curly brackets is a 9-j symbol.

The longitudinal spin-dependent total cross section difference $\Delta\sigma_L$ is defined as the difference between the anti-parallel and the parallel total cross sections for spins aligned along the beam momentum axis:

$$\Delta\sigma_L = \sigma_a - \sigma_p. \quad (2.6)$$

Calculations of $\Delta\sigma_L$ with and without the 3NF (Appendix B) are shown in Figure 2.1 for the CD-Bonn potential [Wit99].

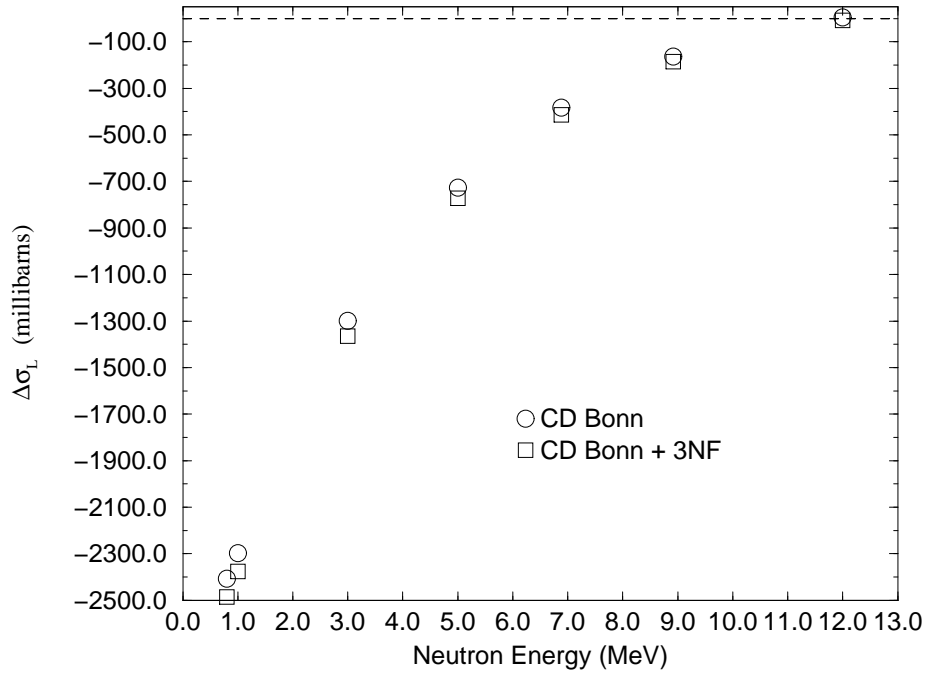


Figure 2.1: $\Delta\sigma_L$ predictions for the CD-Bonn NN Potential with and without the TM 3NF.[Wit99]

2.2 Polarized Neutron Beam Transmission

While pd scattering can be measured to high precision, the most popular system for exploring the three-body interaction is nd scattering, since it is free of electromagnetic effects. This section derives the transmission asymmetry for a beam of polarized neutrons transmitted through a polarized target.

The intensity of a beam of 100% polarized neutrons passing through a target containing polarized nuclei is exponentially attenuated according to

$$\Phi = \Phi_0 e^{-x\sigma_{p(a)}} \quad (2.7)$$

where x is the target thickness in nuclei/barn and $\sigma_{p(a)}$ are the cross sections for neutron and target polarizations parallel and anti-parallel, respectively. In terms of $\Delta\sigma_L$,

$$\sigma_p = \sigma_0 - \frac{1}{2}\Delta\sigma_L \quad (2.8)$$

and

$$\sigma_a = \sigma_0 + \frac{1}{2}\Delta\sigma_L \quad (2.9)$$

where σ_0 is the unpolarized total cross section. If the beam is not 100% polarized, then the transmission is a weighted sum of spin “p” and spin “a” neutrons, giving

$$\Phi = \Phi_0^+ [e^{-N_d^+ x\sigma_p} e^{-N_d^- x\sigma_a} e^{-N_d^0 x\sigma_0}] + \Phi_0^- [e^{-N_d^+ x\sigma_a} e^{-N_d^- x\sigma_p} e^{-N_d^0 x\sigma_0}] \quad (2.10)$$

where Φ_0^\pm are the fraction of incident neutrons with spin up or down and N_d^\pm and N_d^0 are the fraction of deuterons in the +1, -1, or 0 magnetic substates. These are given by

$$N_d^\pm = \frac{1}{2}(1 \pm P_T - N_d^0) \quad (2.11)$$

where P_T is the target polarization defined by

$$P_T = \frac{N_d^+ - N_d^-}{N_d^+ + N_d^- + N_d^0} \quad (2.12)$$

and

$$\Phi_0^\pm = \frac{1}{2}(1 \pm P_n) \quad (2.13)$$

where P_n is the neutron beam polarization defined as

$$P_n = \frac{\Phi_0^+ - \Phi_0^-}{\Phi_0^+ + \Phi_0^-}. \quad (2.14)$$

Substituting the expressions for Φ_0^\pm , N_d^\pm , and $\sigma_{a(p)}$ into Equation 2.10 we get for the transmitted neutron flux

$$\begin{aligned} \Phi = & \frac{1}{2}(1 + P_n) \left[e^{-\frac{1}{2}(1+P_T)x(\sigma_0 - \frac{1}{2}\Delta\sigma_L)} e^{-\frac{1}{2}(1-P_T)x(\sigma_0 + \frac{1}{2}\Delta\sigma_L)} \right] \\ & + \frac{1}{2}(1 - P_n) \left[e^{-\frac{1}{2}(1+P_T)x(\sigma_0 + \frac{1}{2}\Delta\sigma_L)} e^{-\frac{1}{2}(1-P_T)x(\sigma_0 - \frac{1}{2}\Delta\sigma_L)} \right]. \end{aligned} \quad (2.15)$$

We are interested in measuring the neutron transmission asymmetry due to reversing the neutron polarization, i.e.

$$\epsilon = \frac{\Phi(P_n) - \Phi(-P_n)}{\Phi(P_n) + \Phi(-P_n)}. \quad (2.16)$$

The experimental conditions are such that if the positive and negative beam polarizations are equal

$$\epsilon = \frac{P_n \left[e^{\frac{1}{2}P_T x \Delta\sigma_L} - e^{-\frac{1}{2}P_T x \Delta\sigma_L} \right]}{e^{\frac{1}{2}P_T x \Delta\sigma_L} + e^{-\frac{1}{2}P_T x \Delta\sigma_L}} \quad (2.17)$$

$$= P_n \tanh \left[\frac{1}{2} P_T x \Delta\sigma_L \right] \quad (2.18)$$

$$\approx \frac{1}{2} P_n P_T x \Delta\sigma_L. \quad (2.19)$$

The last step is made because the argument is so small the the rest of the terms in the expansion can be safely ignored. If P_n^+ and P_n^- are not equal, then Equation 2.19 is still valid if P_n is the *average* neutron beam polarization [Rai97]

$$P_n = \frac{1}{2}(|P_n^+| + |P_n^-|). \quad (2.20)$$

The observable that is being tested in the $\vec{n} - \vec{d}$ system for 3NF effects is the longitudinal spin-dependent total cross section difference, $\Delta\sigma_L$. Solving Equation 2.19 for $\Delta\sigma_L$ we obtain

$$\Delta\sigma_L = \frac{2\epsilon}{P_n P_T x} \quad (2.21)$$

so that if the transmission asymmetry is measured and P_n , P_T , and x are known, then the cross section difference can be determined.

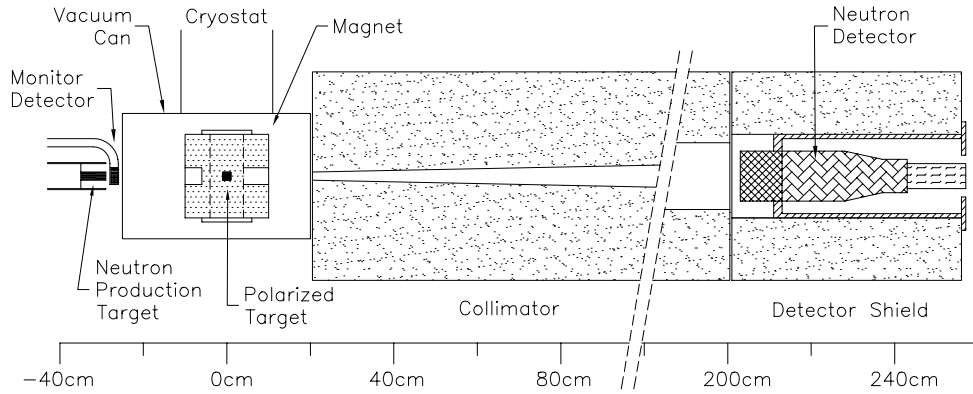


Figure 2.2: Schematic of the equipment used for the polarized neutron transmission experiment.

2.3 Polarized Neutron Transmission Measurement

The longitudinal spin-dependent total cross section difference is extracted from the spin-dependent neutron transmission asymmetries and measurement of the neutron beam and target polarizations and target thickness. The following sections describe the measurements that are required for the determination of $\Delta\sigma_L$, including how we accounted for systematic variations from the ideal case described in Section 2.2.

2.3.1 Neutron Asymmetry Measurements

The “ideal” asymmetry excludes any systematic variations from neutron beam production, charged particle beam current, or charged particle beam polarization. This section will describe how these effects are accounted for in the monitoring of the experiment and analysis of the data.

As shown in Figure 2.2, the polarized neutrons are produced, pass through the polarized target, and are detected at 0° . The actual opening angle is $\pm 1.27^\circ$ about 0° . Two different neutron production targets were used to produce neutrons in the energy range of 1.18 to 9 MeV. The polarized target is located in the center of the superconducting magnet inside the cryostat. A polyethylene collimator between the cryostat and detector allows only neutrons that pass through the target to be detected. The monitor detector is used

for normalization of incident neutron flux for the ${}^2\text{H}(\vec{d}, \vec{n}){}^3\text{He}$ reaction and to remove any systematic asymmetries due to the beam.

The measured neutron transmission asymmetry is

$$\epsilon_{\Phi} = \epsilon_I + \epsilon_n + \epsilon_{P_{zz}} \quad (2.22)$$

where ϵ_I is the beam current asymmetry, ϵ_n is the true spin-dependent asymmetry, and $\epsilon_{P_{zz}}$ is an asymmetry dependent on the deuteron beam tensor polarization. See [Rai97] and [Wal98] for derivations of these beam-dependent asymmetries. Because the monitor detector is upstream from the target, the neutron beam has not interacted with the target and the monitor detector measures an asymmetry

$$\epsilon_{\Phi'} = \epsilon_I + \epsilon_{P_{zz}} \quad (2.23)$$

where the prime denotes a monitor detector asymmetry. By subtracting the monitor asymmetry from the transmission asymmetry, the beam-dependent terms cancel out and the true asymmetry ϵ_n is left.

Instrumental asymmetries can be removed by reversing the target polarization. Consider the neutron transmission asymmetry for positive target polarization

$$\epsilon_n = \frac{N_+ - N_-}{N_+ + N_-} \quad (2.24)$$

where N_{\pm} are the number of neutron counts in the main detector with polarization parallel (+, positive polarization) or antiparallel (-, negative polarization) to the target polarization. Now, if the target polarization is flipped, the neutrons that *were* parallel to target polarization are now anti-parallel and vice-versa. Therefore, ϵ_n changes sign because the target polarization reversal does not affect the incident beam in any way. The average transmission asymmetry is

$$\bar{\epsilon}_n = \frac{1}{2}(\epsilon_n^+ - \epsilon_n^-) \quad (2.25)$$

where ϵ_n^{\pm} are the transmission asymmetries for positive and negative target polarizations, respectively. Any instrumental effects will be removed because they were not affected by the target polarization reversal.

2.3.2 Beam Polarization Measurements

To calculate $\Delta\sigma_L$, the polarization of the neutron beam must be determined. For the ${}^3\text{H}(\vec{p}, \vec{n}){}^3\text{He}$ reaction, the neutron beam polarization was calculated from the measured polarization of the proton beam. For the ${}^2\text{H}(\vec{d}, \vec{n}){}^3\text{He}$ reaction, the neutron polarization was measured directly to avoid having to determine the tensor polarization of the deuteron beam.

Proton Beam Polarimetry

For the 1.18 MeV measurement, the ${}^3\text{H}(\vec{p}, \vec{n}){}^3\text{He}$ neutron production reaction was used. To determine the neutron beam polarization, the proton beam polarization was measured using the scattering chamber that is described in Chapter 3. The scattered protons from the ${}^4\text{He}(\vec{p}, p){}^4\text{He}$ reaction produced a left-right scattering asymmetry. The measurement of the proton beam polarization and the subsequent calculation of the neutron beam polarization are described below.

A charged-particle polarimeter was used for proton polarimetry. A left and a right detector measured spin-up and spin-down protons. The four measured quantities were N_L^+ , N_L^- , N_R^+ , and N_R^- which are the spin-up(+) and spin-down(-) counts in the left(L) and right(R) detectors, respectively. A scattering asymmetry γ is calculated

$$\gamma = \frac{N_L^+ N_R^-}{N_L^- N_R^+} \quad (2.26)$$

where N is the total number of counts for a run of 256 8-step spin-flip sequences. The proton beam polarization is calculated from the asymmetry using

$$P_p = \frac{1}{A_y} \frac{\sqrt{\gamma} - 1}{\sqrt{\gamma} + 1} \quad (2.27)$$

where A_y is the reaction analyzing power calculated for the proton energy at the center of the polarimeter gas cell and detector angle using the Fortran code Ay [Rai97]. The uncertainty in the proton beam polarization is calculated from the standard deviation σ of

the distribution of the measurements and is given by

$$\sigma_{P_p} = \frac{\sigma}{\sqrt{N}} \quad (2.28)$$

where N is the number of measurements.

The resulting neutron beam polarization is calculated using known polarization transfer coefficients ([Jar74] and [Wal98]), which depend on incident beam polarization and energy. The neutron beam polarization is calculated from

$$P_n = P_p K_z^{z'}(0^\circ) \quad (2.29)$$

where $K_z^{z'}(0^\circ)$ is the longitudinal polarization transfer coefficient for the ${}^3\text{H}(\vec{p}, \vec{n}){}^3\text{He}$ reaction at 0° . The uncertainty in the neutron polarization is

$$\sigma_{P_n} = P_n \sqrt{\left(\frac{\sigma_{P_p}}{P_p}\right)^2 + \left(\frac{\sigma_{K_z^{z'}}}{K_z^{z'}}\right)^2}. \quad (2.30)$$

Neutron Beam Polarimetry

For the 5, 6.88, and 9 MeV measurements, the neutron beam was produced through the ${}^2\text{H}(\vec{d}, \vec{n}){}^3\text{He}$ reaction. The incident deuteron beam has vector and tensor polarizations and the neutron beam polarization depends on both according to the following relation:

$$P_n = \frac{\frac{3}{2}P_z K_z^{z'}(0^\circ)}{1 + \frac{1}{2}P_{zz} A_{zz}(0^\circ)} \quad (2.31)$$

where P_z is the deuteron beam vector polarization, $K_z^{z'}(0^\circ)$ is the longitudinal polarization transfer coefficient for the ${}^2\text{H}(\vec{d}, \vec{n}){}^3\text{He}$ reaction, P_{zz} is the deuteron beam tensor polarization, and $A_{zz}(0^\circ)$ is the analyzing power for the reaction. P_{zz} is defined as

$$P_{zz} = \frac{\langle 3I_z^2 - I(I+1) \rangle}{I(2I-1)} \quad (2.32)$$

where I_z is the z-component of the particle spin and I is the maximum value of the spin. In [Rai97], P_{zz} was measured by adding a 0° detector to the left and right detectors in the charged particle polarimeter. This method proved to give a precise measurement of the

tensor polarization. However, excessive heating due to the large beam current proved to be problematic. Walston [Wal98] determined the tensor polarization by measuring the neutron yields in the monitor detector for longitudinal and transverse beam polarizations. These measurements were not as precise as Raichle's. To overcome these difficulties, we decided to measure the neutron polarization directly.

Neutrons incident on a high-pressure cell of ^4He exhibit a left-right scattering asymmetry similar to the $^4\text{He}(\vec{p},\text{p})^4\text{He}$ reaction. A pair of left-right detectors count spin-up and spin-down neutrons that are produced by the $^2\text{H}(\vec{d},\vec{n})^3\text{He}$ reaction and scattered from a cell containing 1200 PSIG ^4He gas. The neutron beam polarization was calculated from the scattering asymmetry in the same manner as the proton beam polarization was calculated.

2.3.3 Deuteron Target Polarization Measurement

The deuteron target polarization was monitored regularly via nuclear magnetic resonance (NMR). The theory and equipment used for NMR will be detailed in Chapter 4. The deuteron target used in this experiment was polarized to approximately 25%. The NMR data consist of sets of signals, one or two per neutron data run, which were analyzed individually offline. Backgrounds were saved before polarizing the target and were subtracted in order to view the polarized deuteron signal. Each signal file name was recorded along with the neutron data run number and the target temperature.

To determine the deuteron target thickness, the target cup is removed from the refrigerator insert and is placed in a 50 ml beaker. The mouth of the beaker is sealed with aluminum foil and a rubber band and the beads are allowed to melt. The beaker and its contents are weighed, the target material is removed, and the beaker and empty target cup are weighed again to determine the difference. Details on the calculation of the target thickness will be given in Section 4.4.2.

Chapter 3

Polarized Neutron Beam

The polarized neutrons are produced as a secondary beam from the ${}^3\text{H}(\vec{p}, \vec{n}){}^3\text{He}$ reaction for neutron energies less than 5 MeV and the ${}^2\text{H}(\vec{d}, \vec{n}){}^3\text{He}$ reaction for the higher energies. The polarized proton and deuteron beams are produced by the Atomic Beam Polarized Ion Source and the axis of polarization is set by the Wien filter. The beam is accelerated by a Van de Graaff accelerator, passes through an analyzing magnet, and is steered to the production target.

3.1 The TUNL Atomic Beam Polarized Ion Source

The TUNL Atomic Beam Polarized Ion Source (ABPIS) [Cle95a] can produce beams of vector polarized protons and vector and tensor polarized deuterons. A schematic of the ABPIS is shown in Figure 3.1.

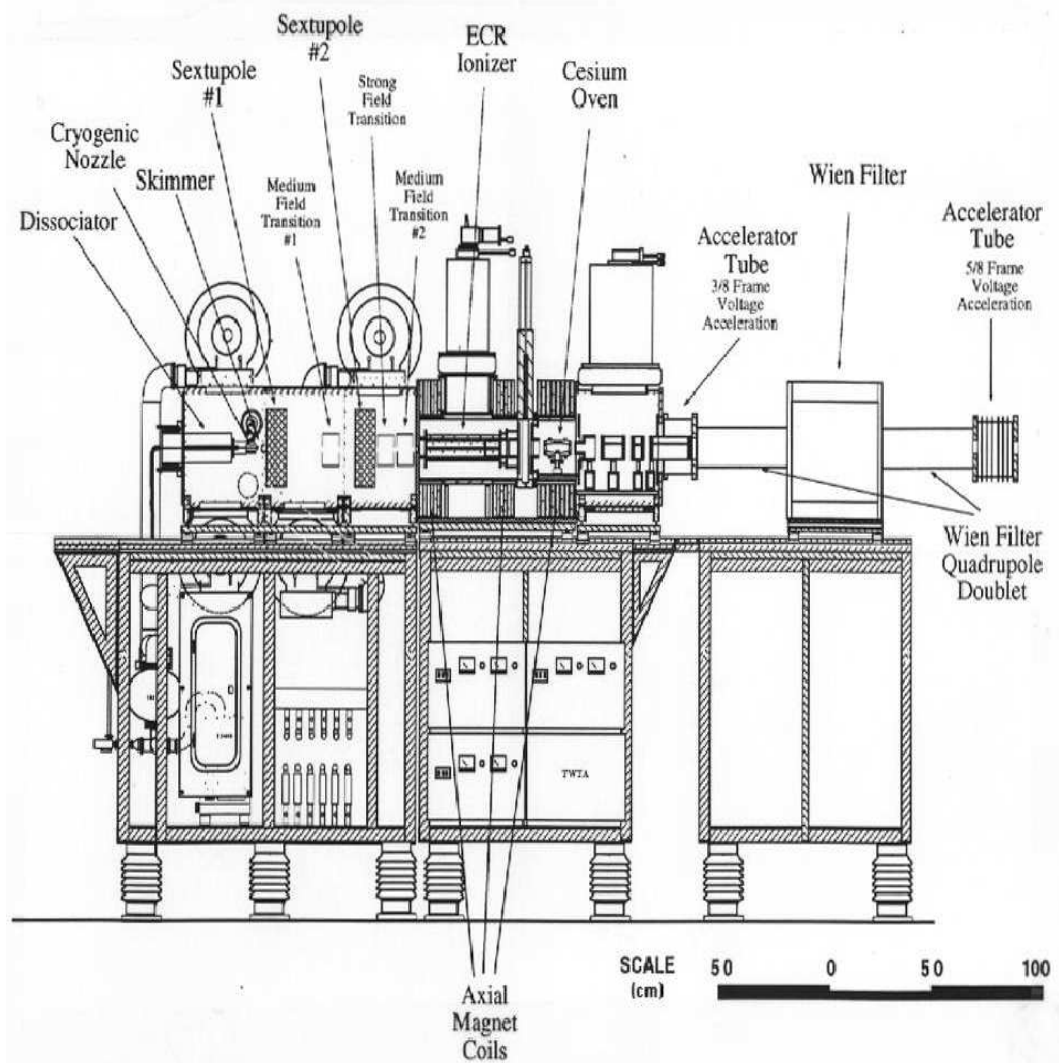


Figure 3.1: Schematic of the the TUNL Atomic Beam Polarized Ion Source.

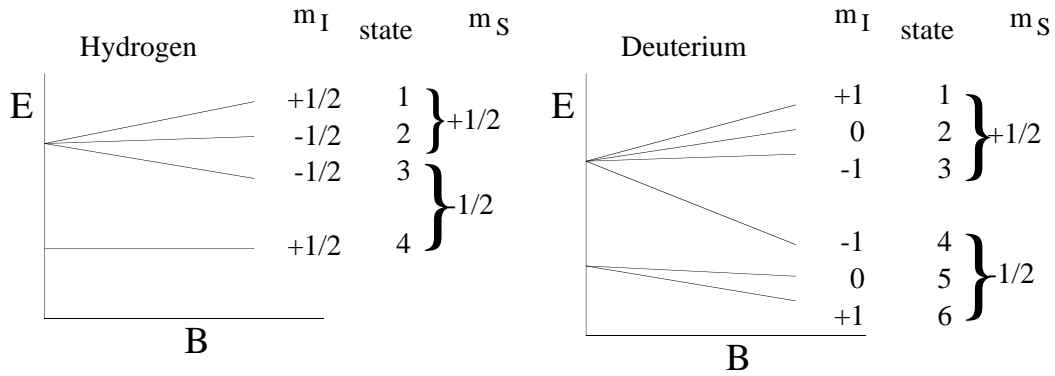


Figure 3.2: Energy level splitting of the nuclear hyperfine states of hydrogen and deuterium atoms in a magnetic field.

The source takes molecular hydrogen or deuterium and dissociates it in an rf discharge. The discharge is created by driving an rf coil at 14 MHz. This coil is wrapped around a quartz tube, which contains the gas to be dissociated. Nitrogen gas is also fed into the dissociator in order to reduce recombination of H or D. The atomic beam is slowed as it passes through a cryogenically cooled nozzle. The nozzle is cooled to 35 K by a 10 W closed-cycle Gifford-McMahan refrigerator.

The slow moving atomic beam is focused using two iron-core electromagnetic sextupoles. The sextupoles focus atoms that have electron spin parallel ($m_s = +1/2$) to the magnetic field and defocus atoms that have spin anti-parallel ($m_s = -1/2$) to the field. These defocused atoms are pumped away by four turbo pumps which have a combined pumping speed of 8800 l/s.

Three radio frequency transition units, one strong field (SF) unit and two medium field (MF1, MF2) units, are used to transfer the electron polarization to the nuclei. A magnetic field inside the units is used to produce the hyperfine splitting and an rf oscillator is tuned to a hyperfine transition frequency. The nuclei are polarized by interchanging populations of selected hyperfine states.

The polarized proton beam is produced by first polarizing the atomic hydrogen beam in electron spin by focusing states 1 and 2 and defocusing states 3 and 4 (see Figure 3.2)

as it passes through the first sextupole. Because the first transition unit, MF1, is not used, the beam passes through the second sextupole unchanged. The SF unit is tuned to induce the $2 \rightarrow 4$ transition if positive or “spin-up” polarization is desired and as a result, states 1 and 4 are populated, with $m_I = +1/2$. However, if negative, or “spin down” polarization is needed, MF2 is used to drive the $1 \rightarrow 3$ transition, leaving states 2 and 3 populated and $m_I = -1/2$.

The polarized deuteron beam is produced in a similar way. As the atomic deuterium beam passes through the first sextupole, states 1, 2, and 3 are focused while 4, 5, and 6 are defocused and pumped away (see Figure 3.2). The MF1 transition unit is used in this instance and drives the $3 \rightarrow 4$ transition. The second sextupole then defocuses state 4. To produce positive polarization, SF induces the $2 \rightarrow 6$ transition, leaving states 1 and 6 populated and $m_I = +1$. For negative polarization, MF2 drives the $1 \rightarrow 4$ and $2 \rightarrow 3$ transitions and states 3 and 4 are left populated and $m_I = -1$. The beam polarization is longitudinal or parallel to the beam momentum.

After the polarized proton or deuteron beam leaves the transition units and sextupoles, it enters the electron cyclotron resonance (ECR) ionizer where it is stripped of its electron. The ECR contains an electron plasma that is produced by irradiating nitrogen gas with an rf field. The electron plasma removes the atomic electron via atom-electron collisions.

The TUNL electrostatic accelerator requires negatively charged beam so a cesium oven directly follows the ECR and is used to produce a negative beam by adding two electrons to the polarized nuclei. A vapor is formed in the oven by heating a sample of cesium to 200° C. Electrons are transferred from the vapor to the beam with a 10% efficiency as it passes through the oven. The ECR-cesium oven combination is used because positively- or negatively-charged beams can be produced with the same system, depending on whether or not the cesium vapor is present [Cle95b].

Some of our calibration experiments required polarized beams that were not longitudinally polarized. The Wien filter uses crossed electric and magnetic fields to rotate the

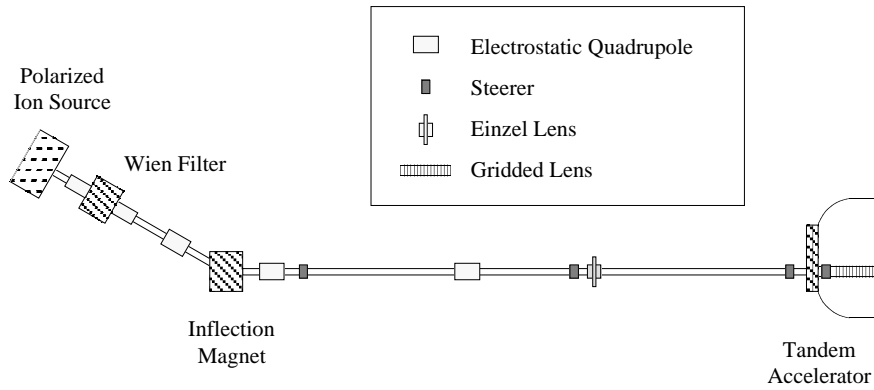


Figure 3.3: The TUNL low-energy beam transport facility.

polarization axis to any direction. The magnetic field precesses the spin axis and the electric field keeps the beam on axis. The Wien filter is physically rotated to produce the necessary polarization axis orientation. The Wien filter is also used to compensate for precession through analyzing magnets. The negatively charged nuclear polarized beam is accelerated to the source frame voltage (-75 keV) and is focused with a set of lenses.

3.2 Beam Acceleration and Transport

The low energy transport facility connects the ABPIS to the electrostatic accelerator and is shown in Figure 3.3. A 30° bending magnet bends the beam towards the accelerator where it is focused by two electrostatic quadrupoles and an Einzel lens and two magnetic steerers are tuned to control the beam position.

The TUNL tandem Van de Graaff accelerator [VdG60] is a 10 MV electrostatic accelerator. The accelerator consists of a large tank pressurized with a mixture of CO_2 , N_2 , and SF_6 gas to insulate the tank from the highly charged terminal. The terminal is held in place by a column that runs the length of the tank and is supported by compression from each end. The column also supports the beamline that runs from the entrance of the tank through the terminal and exits the tank. The column consists of alternating quartz insulators and metal spacers. A stepped voltage gradient from the terminal to each end of

the tank is created by resistors located between the metal spacers. The terminal voltage is gradually stepped down to ground at each end of the column by a total resistance of 100 gigaohms. The accelerator uses a pelletron system, which consists of a pair of charging chains with one on each end of the tank, to deposit positive charge on the terminal. Each chain consists of stainless steel links separated by nylon spacers, is charged by a high-voltage supply at the tank wall, and deposits its charge on brushes in the terminal.

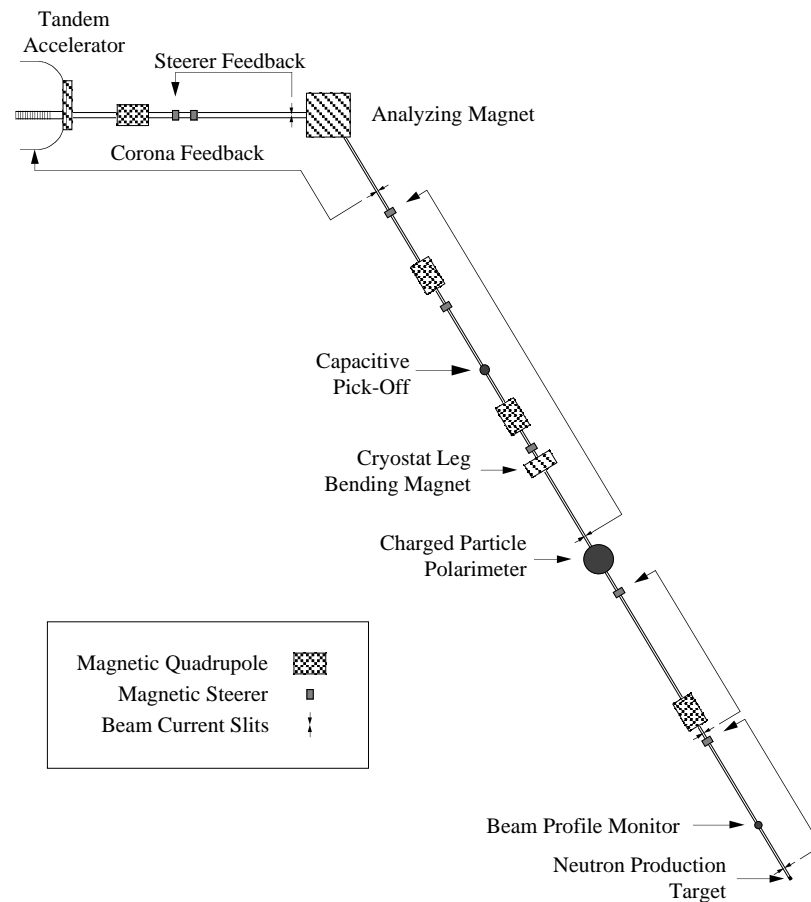


Figure 3.4: The TUNL high-energy beam transport facility.

The negatively charged beam is accelerated from the low energy end towards the accelerator terminal, which is at a high positive potential. A carbon foil inside the terminal strips off two electrons from each negatively charged ion, producing a positively charged

beam, which is accelerated away from the terminal. This produces a beam with an energy that is roughly twice the terminal potential.

The beam leaves the high energy end of the accelerator and is analyzed in energy by a bending magnet (Figure 3.4). The field of this magnet sets the beam energy and is controlled by an NMR feedback system. Two slits downstream from the magnet provide a feedback signal to the terminal voltage stabilizer circuit. The terminal potential is set to minimize the current difference between these two slits. The control signal from the slits is fed back to the corona control tube by the Terminal Voltage Stabilizer circuit. The corona is a set of sharp needles that protrude from the tank wall towards the terminal and regulates the terminal voltage by drawing current from the terminal. The slit feedback signal controls a reverse voltage that is applied to the needles in order to make fine adjustments to the terminal potential. Further down the beamline, three magnetic steerers with feedback slits guide the beam to the neutron production target.

3.3 Proton Polarimetry

The neutron polarization of the beam produced by the ${}^3\text{H}(\vec{p}, \vec{n}){}^3\text{He}$ reaction was determined by measuring the polarization of the polarized proton beam via its transverse scattering asymmetry from ${}^4\text{He}$ gas. A scattering chamber (Figure 3.5) several meters upstream from the polarized target was used for proton polarimetry. The chamber contained a ${}^4\text{He}$ gas cell that could be moved in and out of the beam. The cylindrical cell had a 2.54 μm thick Havar foil wall that was epoxied to the cell frame contained one atmosphere of ${}^4\text{He}$ gas. Transversely polarized incident protons scattered from the ${}^4\text{He}$ showed an up/down scattering asymmetry. Scattered protons were detected by two 1000 μm depletion depth silicon detectors positioned on separate support rings and biased to +97 V. The detectors could be placed in three degree increments from 45° to 135° . Collimators were placed in front of the detectors so that the detectors viewed a solid angle of 0.5 ms. The proton polarimetry was done with incident beam energy of 2.69 MeV, which gave a proton energy

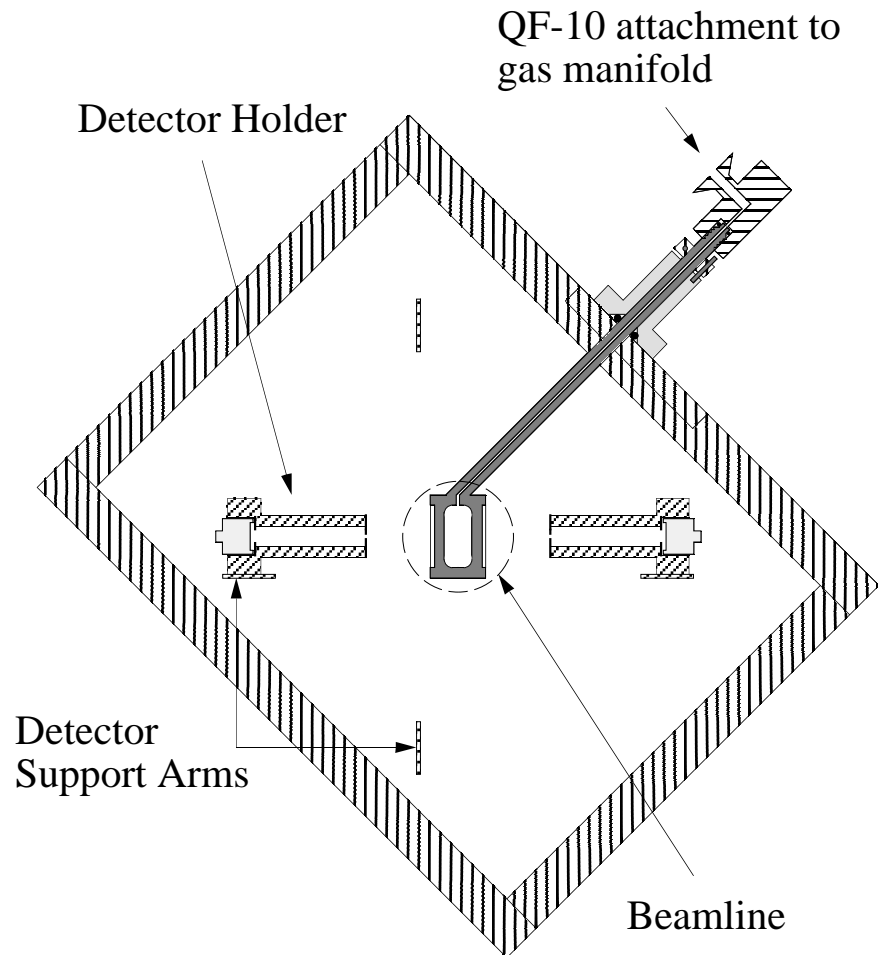


Figure 3.5: The polarimeter scattering chamber. This view is along the beam line axis. The ^4He gas cell is shown in position for performing polarimetry measurements, but can be moved out of the path of the beam for taking neutron transmission data. The detector support arms are hemispherical structures anchored to the chamber lid. The detectors are the lightly shaded areas at the rear of the detector holders.

of 2.52 MeV at the center of the ^4He gas cell. The detectors were placed at an angle of 75° , which resulted in an analyzing power of 0.721 ± 0.007 . The analyzing power was calculated with the Fortran code A_y [Rai97], which is based on the explicit partial-wave expansion of the elastic scattering amplitude for spin 1/2 particles found in [Sat83]. Phase shifts were obtained from the effective-range parametrization from [Sch71]. A 2% systematic error from Schwandt's measurements have not been included in this work because of the small effect it has on the final values of $\Delta\sigma_L$. Asymmetry measurements were also made with the beam polarized longitudinally to check for a transverse component of the polarization and to verify the Wien filter settings. Data from the proton polarimetry measurements can be found in Section 6.1.

The signals from the polarimeter detectors pass through Ortec 142A preamplifiers and Ortec 572 amplifiers before being sent to Ortec 551 timing SCA's. The signals are summed and then go to a Northern ADC. The SCA's generate gates that append detector routing information to the signals. Spin-routing bits are also added through an ADC interface. The extra routing information allows the use of one ADC for both detectors.

3.4 Neutron Production

The polarized neutron beam is created as a secondary beam from polarized protons or deuterons. For beam energies 5 MeV and greater, the $^2\text{H}(\vec{d}, \vec{n})^3\text{He}$ reaction was used to produce the neutron beam. The Q value for this reaction was 3.269 MeV. A gas cell, shown in Figure 3.6, containing 45 PSIA of deuterium gas was placed on the end of the beam line. The volume containing the deuterium was 6 cm long and 1.9 cm in diameter, producing a deuterium thickness of 4 mg/cm^2 .

The gas cell had a $6.35 \mu\text{m}$ thick Havar entrance window separating it from the beamline vacuum and a 0.51 mm thick tantalum beam stop to prevent any deuterons from exiting the gas cell. Energy loss calculations and neutron beam energies were calculated for the center of the gas cell and are found in Table 3.1. The spread in the neutron beam

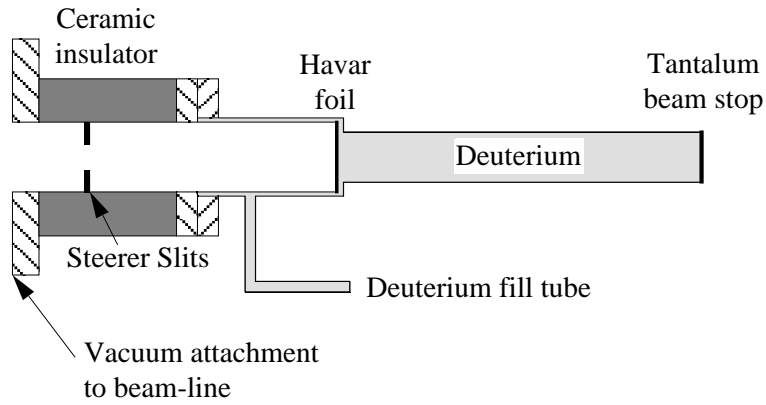


Figure 3.6: The deuterium gas cell neutron-production target.

energy is the difference in energy between neutrons produced at the start and end of the deuterium added in quadrature to the deuteron beam energy straggling through the Havar, estimated to be 10% of the energy loss through the Havar. Each neutron is not involved in the same number of collisions and as a result, does not have the same energy loss. The energy spread of the beam is a statistical distribution centered around some mean energy. This is known as straggling.

Table 3.1: Energy-loss calculations through the deuterium gas cell. Energies are in MeV.

Beam Location	E_d	E_n	E_d	E_n	E_d	E_n
Havar Entrance	3.01	—	4.46	—	6.42	—
Havar Exit	2.43	—	4.01	—	6.07	—
D ₂ Entrance	2.43	5.69	4.01	7.27	6.07	9.27
D ₂ Center	1.78	5.00	3.60	6.88	5.79	9.00
D ₂ Exit	0.820	3.92	3.15	6.41	5.49	8.71
\bar{E}_n (ΔE_n)	5.00 (1.77)		6.88 (0.86)		9.00 (0.56)	

A set of feedback slits at the entrance of the gas cell is used to keep beam steered onto the target. Beam current is measured by integrating the accumulated charge on the production target. The tantalum beam stop is cooled by blowing compressed air on the back of it. A typical neutron rate in the main detector was 60,000/s with 500 nA of 2 MeV deuteron beam.

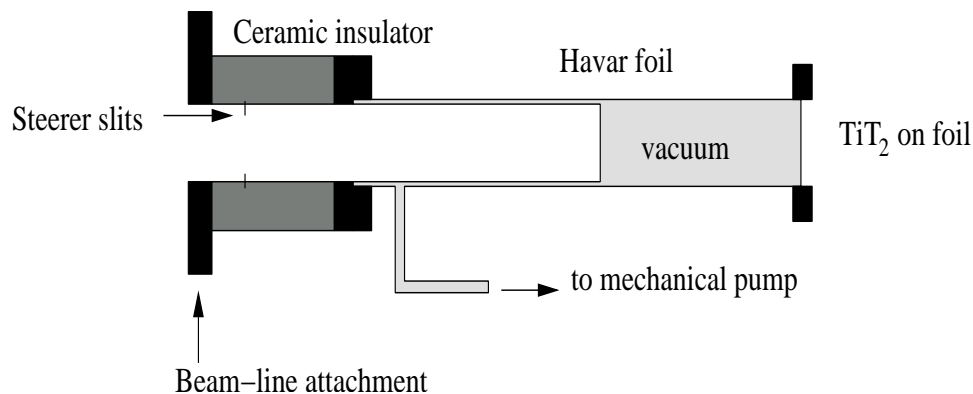


Figure 3.7: The tritiated titanium neutron-production target.

For the 1.18 MeV data, neutrons were produced via the ${}^3\text{H}(\vec{p}, \vec{n}){}^3\text{He}$ reaction, which has a Q-value of -0.764 MeV. A tritiated titanium (TiT_2) foil of thickness of 0.11 mg/cm^2 was placed at the end of the charged particle beam line and cooled by a flow of compressed air (Figure 3.7). The foil was isolated from the beam line by a $2.228 \text{ }\mu\text{m}$ thick Havar foil and a 3.0 cm long evacuated buffer space. The energy of the produced neutrons is affected by the energy loss and spread in the Havar and TiT_2 foils. As shown in Table 3.2, the final energy as calculated from the center of the TiT_2 foil was 1.18 MeV with a spread of 0.07 MeV. A neutron count rate in the main detector of 250/s was achieved with 270 nA of 1.98 MeV protons.

Table 3.2: Energy-loss calculations through the tritium foil. Energies are in MeV.

Beam Location	E_p	E_n
Havar Entrance	2.18	—
Havar Exit	2.01	—
$TiT_{1.4}$ Entrance	2.01	1.21
$TiT_{1.4}$ Center	1.98	1.18
$TiT_{1.4}$ Exit	1.94	1.14
$\bar{E}_n (\Delta E_n)$	1.18 (0.07)	

3.5 Neutron Polarimetry

In the ${}^2\text{H}(\vec{d}, \vec{n}){}^3\text{He}$ reaction, the tensor component of the deuteron beam has a significant effect on the outgoing neutron polarization. Because the tensor component is so difficult to measure reliably, the neutron polarization was measured directly for the experiments with $E_n \geq 5$ MeV.

For the neutron polarimetry the deuteron beam was steered down the 38° beam line and into the neutron time of flight room. A neutron production gas cell similar to the one used for the neutron transmission experiment was filled with 45 PSIG of deuterium gas. The neutron polarimeter consisted of a ${}^4\text{He}$ cell and neutron detector pairs arranged symmetrically about the beam axis. A scattering asymmetry is measured in the detector pairs, enabling a very accurate calculation of the neutron beam polarization since the analyzing power of elastically scattered neutrons from ${}^4\text{He}$ can be done with an accuracy of ± 0.01 .

The polarized neutron beam was produced via the ${}^2\text{H}(\vec{d}, \vec{n}){}^3\text{He}$ reaction and was collimated. The polyethylene collimator was 52.7 cm long and had an entrance that was 2.54×3.17 cm and an exit opening that was 3.81×5 cm. The distance between the neutron production cell and the collimator entrance was 10.1 cm. The ${}^4\text{He}$ cell was 1.5 m downstream from the exit of the collimator. Two scintillation detectors, right and left, were set up at 116° on a ring around the high-pressure ${}^4\text{He}$ gas cell and were approximately 21.6 cm from the center of the cell. The cell contained 1200 PSIG of ${}^4\text{He}$ gas. The analyzing power for this detector angle was calculated to be 0.92 ± 0.01 [Tor03]. Finite geometry brings the point-geometry value of A_y of 0.98 down to 0.95. Multiple scattering on He, Xe and Fe brings it further down to 0.92. The detectors counted scattered neutrons that were spin-up and spin-down. The left-right scattering asymmetry was used to calculate the neutron beam polarization for the ${}^2\text{H}(\vec{d}, \vec{n}){}^3\text{He}$ reaction. Neutron polarimetry was performed for $E_n = 6.88$ MeV and was used to calculate P_z and P_{zz} . These values were used along with

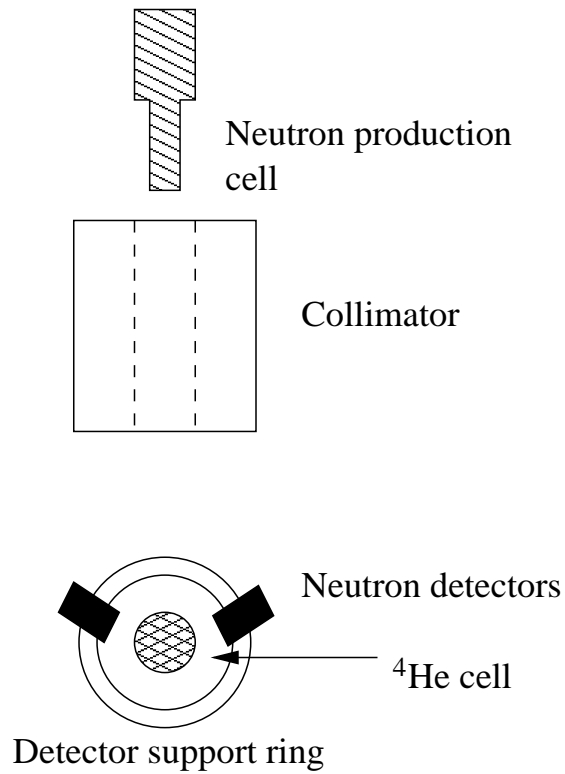


Figure 3.8: The neutron polarimetry setup. This view is from above the equipment. The scintillation neutron detectors can be placed at arbitrary angles on the support ring. A left-right scattering asymmetry is measured and used to calculate the neutron polarization.

values of $K_z^{z'}(0^\circ)$ and $A_{zz}(0^\circ)$ from [Hal98], [Sal73], and [Lis75] to calculate the neutron polarization at other energies. A schematic of the neutron polarimetry setup is shown in Figure 3.8.

Chapter 4

Polarized Deuteron Target

The deuteron target is polarized using the method of dynamic nuclear polarization (DNP). This method preferentially populates a certain magnetic substate by irradiating the target with microwaves tuned to the frequency of the substate splitting in a magnetic field. DNP allows for a relatively quick reversal of target polarization by retuning the microwave frequency. Because DNP requires that the target be at a low temperature and in a high magnetic field, the target is cooled to 250 mK using a ^3He - ^4He dilution refrigerator, as described in Section 4.2. Thermometry is described in Section 4.3. The target material is discussed in Section 4.4. The target polarization is determined by nuclear magnetic resonance, which is described in Section 4.5. The chapter begins with an introduction to dynamic nuclear polarization.

A measurement of $\Delta\sigma_L$ can be characterized by a figure of merit which is proportional to the amount of experimental time required to achieve a certain precision in $\Delta\sigma_L$. The figure of merit for a transmission experiment is proportional to $(P_T x)^2$ [Wal98]. In the present experiment, we have increased P_T by a factor of 2 to 2.5 over previous measurements [Mar02] by cooling the target with a dilution refrigerator. By choosing a fully deuterated (D8) target, the effective target thickness has been increased by one-third and the effects of extra protons have been significantly decreased.

4.1 Dynamic Nuclear Polarization

4.1.1 Theory

A polarized target can be thought of as an ensemble of nuclear and electronic spins placed in a large magnetic field and cooled to a low temperature. The interaction between the nuclear magnetic moment and the magnetic field produces $2I+1$ Zeeman sublevels, where I is the nuclear spin. If the system is in thermal equilibrium, then the populations of the m sublevels for a spin I particle are given by a Boltzmann distribution,

$$n_m = \frac{e^{-\frac{\Delta E}{kT}}}{\sum_m e^{-\frac{\Delta E}{kT}}} \quad (4.1)$$

where $\Delta E = h\nu$ is the energy level splitting, h is Planck's constant, k is Boltzmann's constant, m is the magnetic substate, and T is the temperature of the system. The substate projections are defined by the magnetic field direction. The polarization of a spin-1/2 system is defined as

$$P(1/2) = \frac{N_+ - N_-}{N_+ + N_-} \quad (4.2)$$

and the vector polarization of a spin-1 system is defined as

$$P_z(1) = \frac{N_+ - N_-}{N_+ + N_- + N_0}. \quad (4.3)$$

A spin-1 system also has alignment as defined by

$$A_d = \frac{1 - 3N_0}{N_+ + N_0 + N_-} \quad (4.4)$$

and in thermal equilibrium the alignment is related to the vector polarization by

$$A_d^2 - 4A_d + 3P_z^2 = 0. \quad (4.5)$$

Using these definitions, the thermal equilibrium polarizations can be described by

$$P(1/2) = \tanh\left(\frac{h\nu}{kT}\right) \quad (4.6)$$

and

$$P_z(1) = \frac{4\tanh\left(\frac{h\nu}{kT}\right)}{3 + \tanh^2\left(\frac{h\nu}{kT}\right)}. \quad (4.7)$$

At $T=1$ K and $B=2.5$ T, the spin $1/2$ electrons are 92% polarized due to their large magnetic moment, which is $1838\mu_N$, where μ_N is the nuclear magneton. However, the deuteron's magnetic moment is $0.857\mu_N$ and under these conditions the deuterons have no useful thermal equilibrium polarization (0.05%). The technique of dynamic nuclear polarization provides a way to obtain high nuclear polarizations.

Dynamic nuclear polarization relies on the availability of “free” electrons, which, as discussed before, have a large thermal equilibrium polarization. These unpaired electrons are provided by doping the target material with a paramagnetic radical. The dipole-dipole coupling between the nuclear spins and the electron spins produces hyperfine splitting. By irradiating the target with RF waves tuned close to the electron spin resonance frequency, the polarization can be transmitted from the electrons to the nuclei. DNP works well because the relaxation time for electrons is very short compared to that of the nuclei.

If the spin-spin interaction between the electrons is ignored, then the process of DNP can be described by the solid-state effect [Abr61]. In this case, the electron spin resonance absorption line is narrow compared to the nuclear Larmor frequency. The Zeeman splittings are given by

$$\Delta = h\nu_S \quad (4.8)$$

and

$$\delta = h\nu_I \quad (4.9)$$

where S refers to the electronic frequency, I refers to the nuclear frequency, and h is Planck's constant. Simultaneous reversals of S and I in opposite directions (flip-flops) and reversals in the same direction (flip-flips) are allowed by the dipolar interaction and change the total energy of the spin system by an amount $h(\nu_s \pm \nu_I)$. This energy is supplied by the crystalline lattice in the form of phonons and these reversals are responsible for nuclear relaxation. The rate of these processes goes as $1/T$ and is very small at low temperatures, with relaxation times on the order of several hours. The electrons are coupled to the lattice and a reversal of an electron alone occurs on the order of milliseconds via the absorption or emission of a single phonon with energy $\hbar\omega_S$. Flip-flops ($\nu = \nu_S + \nu_I$) or flip-flips ($\nu = \nu_S - \nu_I$) can be induced

if the appropriate frequency microwaves are applied. A flip-flop is a forbidden transition because of quantum mechanical selection rules, but because of the dipolar interaction, the nuclear and electronic states are mixed and the flip-flop transitions are allowed to second order.

Consider a spin I that is down. It may do a flip-flop with a spin S that is up so that I is now up and S is down. Through its coupling to the lattice, S quickly relaxes and flips back up and may be used to flip another spin I. This way, each electron can be used to flip multiple nucleons because the number of polarizable nucleons is greater than the number of available electrons. The nucleon must have a long relaxation time in order for this process to be efficient. It is clear that if $\nu = \nu_S + \nu_I$, then flip-flop transitions occur and all of the spins I end up down. The maximum nuclear polarization, P_I , can be no greater than the electron polarization, P_S .

When the concentration of electrons is large enough that the dipolar interactions among them cannot be ignored, the DNP process is described by the equal spin temperature theory [deB76]. When these interactions are considered, the Zeeman levels are no longer sharp, but are broadened. These levels can now be thought of as bands of semi-continuous states, as in Figure 4.1(a). The populations of the states in these bands are given by Boltzmann distributions, with T_Z the temperature of the electron Zeeman reservoir and T_{SS} the temperature of the electron spin-spin interaction reservoir. The introduction of the spin-spin temperature is necessary because the dipolar interactions provide an additional energy reservoir that is independent of the Zeeman reservoir and the lattice temperature.

At thermal equilibrium, T_Z and T_{SS} are equal to the lattice temperature, T_L . T_{SS} can be changed by irradiation with slightly off-resonance microwaves and the sign of T_{SS} can become positive or negative, depending on the sign of $\Delta = \nu_e - \nu$, where ν is the irradiation frequency. The equal spin temperature theory has been proven to be valid for frozen alcohols [deB76] by showing that optimal polarization for different nuclei can be attained at the same microwave frequency. If the thermal contact with the spin-spin interaction reservoir is strong enough, then the final polarizations of different nuclear spins

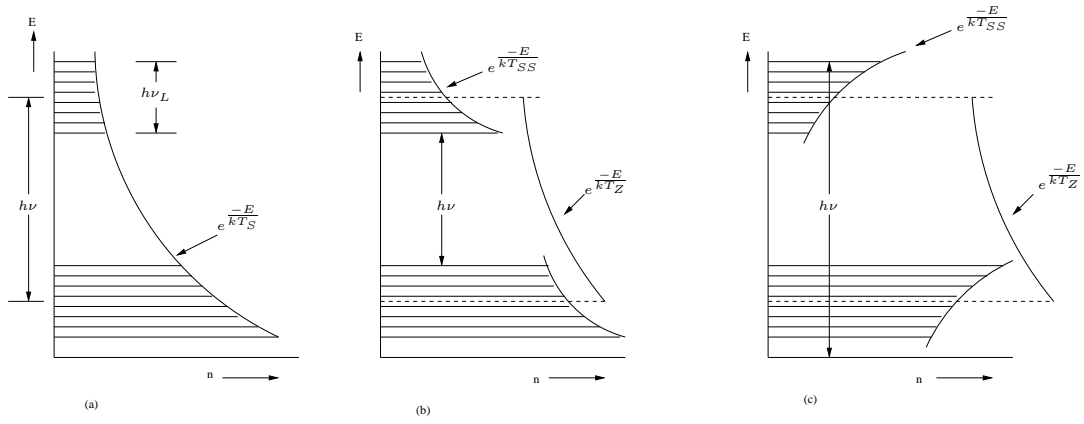


Figure 4.1: The spin-temperature theory of dynamic nuclear polarization. (a) shows the distribution of spins n in thermal equilibrium with spin-temperature T_S . (b) and (c) illustrate the separate electronic (T_Z) and nuclear (T_{SS}) spin-temperatures for positive and negative polarizations, respectively. The irradiation frequency is denoted by ν .

will correspond to the same spin temperature. Therefore, if the polarization of one nucleus is known, then the polarization of all other nuclear species in the sample can be calculated.

Dynamic nuclear polarization is a two step process in the spin-temperature case. First, the electron spin-spin reservoir absorbs an amount of energy $h(\nu_e - \Delta)$ from the microwave field. Part of this energy, $h\nu_e$, is used to change the electron Zeeman energy and the other part, $h\Delta$, is absorbed by the electron spin-spin reservoir. If $\Delta > 0$, then the spin-spin reservoir must emit energy and it cools down (See Figure 4.1(b)). A nucleon moves from the top of the distribution to the bottom, producing positive nuclear polarization and a positive T_{SS} . If $\Delta < 0$, then the spin-spin reservoir is heated and $T_{SS} < 0$ as in Figure 4.1(c). A nucleon is moved from the bottom of the distribution to the top to produce negative polarization. The second step is the thermal mixing between the electron spin-spin reservoir and the nuclear Zeeman reservoir. Consider the forbidden relaxation process in which two electron spins flip-flop together with a flip of a nucleon spin. The electron Zeeman temperature remains constant while the nuclear Zeeman energy changes by $h\nu_n$. This relaxation mechanism takes place without interaction with the lattice and the spin-spin reservoir provides the energy conservation through its thermal coupling with the nuclei. The energy $h\nu_n$ is exchanged between both reservoirs and T_{SS} and the nuclear

Zeeman temperature, T_{Zn} , are equalized.

The electron spin resonance response of the D8 propanediol target material was characterized by observing the absorption of microwave energy as a function of magnetic field. While the klystron frequency and power were held constant and the magnet current was swept stepwise, the resistance of a germanium thermometer located adjacent to the target material was observed. The resistance of the thermometer is proportional to the log of its temperature; as the temperature decreases the resistance increases.

The microwave heat input (\dot{Q}_{IN}) is absorbed through non-resonant mechanisms in the thermometer and target cavity (\dot{Q}_{NR}) and resonantly in the propanediol (\dot{Q}_{D8}) [Ade96]. The relationship between the absorbed heat and the thermometer temperature is shown in the following equation:

$$\begin{aligned}\dot{Q}_{IN} &= \dot{Q}_{NR} + \dot{Q}_{D8} \\ &= c(T_{ge}^4 - T_{He}^4) + \dot{Q}_{D8} \\ &= cT_{ge}^4 - cT_{He}^4 + \dot{Q}_{D8}\end{aligned}\tag{4.10}$$

where c is a constant, T_{ge} is the temperature of the thermometer, and T_{He} is the temperature of the liquid helium in the mixing chamber. The heat from all processes is finally transferred to the helium bath through surface conduction. Therefore, as the propanediol absorbs microwaves the heat input to the thermometer decreases and the thermometer resistance increases. Figure 4.2 displays the raw data of germanium thermometer resistance versus successive sweeps of the current of the superconducting magnet. The minima near 78.2 A and 78.8 A mark the edges of the resonant absorption.

The magnet constant was 0.0318 T/A and the central microwave frequency was 69.5 GHz. Therefore the width of the ESR absorption was about 0.001 T or 530 MHz. These values are consistent with the measurements of [Ade96], who found, as we have, that the maximum polarizations are found on the shoulders of the absorption curve.

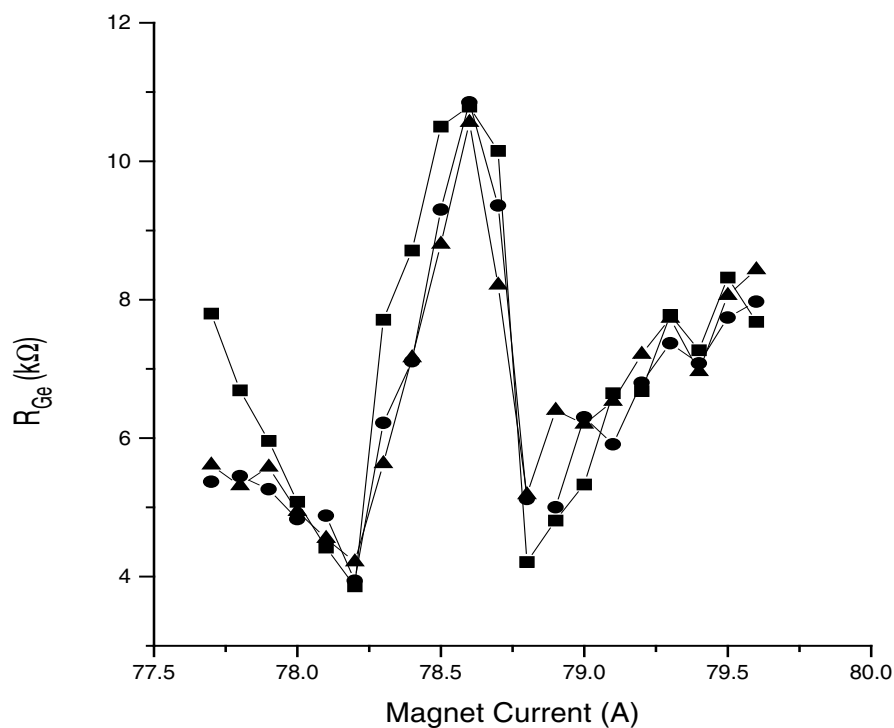


Figure 4.2: Experimental ESR spectrum. The magnetic field was swept up or down in 0.1 A increments and the resistance of the germanium thermometer was recorded at each step. Larger resistance values correspond to lower temperatures.

4.1.2 DNP Equipment

The magnet used in this experiment is a 10.16 cm bore split-coil superconducting magnet, oriented to provide a longitudinal field. The magnet is wound with Ni-Ti wire and is operated in persistent mode with 80 amps of current. Persistent mode provides a rated field homogeneity that is better than 0.01% over a volume of 1 cm³.

A Micro-Now model 756 power supply and a Varian VC-1112 model klystron provide the 69 GHz microwaves for DNP. By adjusting the physical volume of the klystron, the

microwave frequency can be tuned so that positive and negative deuteron polarizations can be achieved near 69.3 and 69.7 GHz, respectively. These frequencies can be determined from the ESR absorption. The klystron settings for positive and negative polarizations were recorded as settings on a micrometer that was used for tuning. The frequency is fine tuned using the reflector voltage control on the power supply and a beat frequency between the microwaves and a reference frequency (11.5 GHz, the 6th harmonic of the 69 GHz microwave frequency) is observed on a frequency meter. Beat frequencies in the ranges 100-140 and 500-550 MHz were observed for positive and negative polarizations, respectively.

The klystron is connected to the target material via a 0.635 cm diameter cylindrical waveguide. The waveguide terminates in a microwave horn that is directly above the target material. An attenuator between the klystron and the waveguide allowed a fine adjustment of the delivered microwave power. The attenuator was adjusted so that the mixing chamber stayed below 350 mK.

4.2 Dilution Refrigerator

4.2.1 Theory of Operation

Liquid mixtures of ^3He and ^4He undergo a phase separation when the temperature is lowered below 0.8 K. Below this temperature, a concentrated phase of pure ^3He floats on a dilute phase that is 94% ^4He and 6% ^3He . This phase separation remains in equilibrium down to absolute zero and is necessary for dilutive cooling [Lou79]. In a dilution refrigerator (Figure 4.3), the phase separation occurs in the mixing chamber. A tube extends from the dilute phase in the mixing chamber to the still so that an unbroken column of the dilute phase fills the still.

The still temperature is kept in the range 0.6 - 1.0 K by a heater because the vapor pressure of ^3He is 1000 times greater than that of ^4He at those temperatures. When the still is pumped on, the majority of gas pumped out is ^3He . By removing ^3He atoms from the dilute phase, the equilibrium has been destroyed. There is a chemical potential gradient

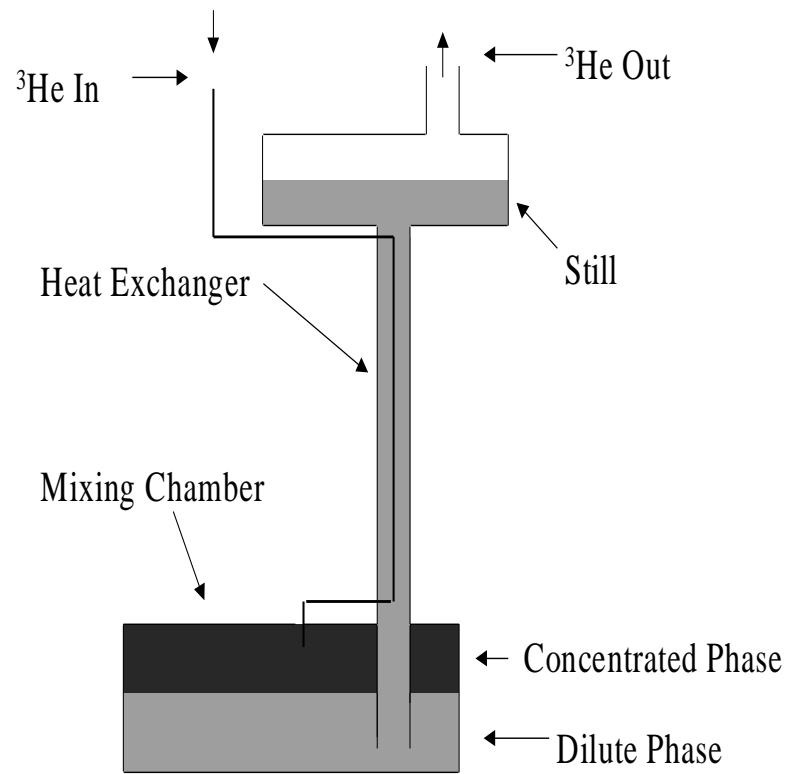


Figure 4.3: A simple dilution refrigerator.

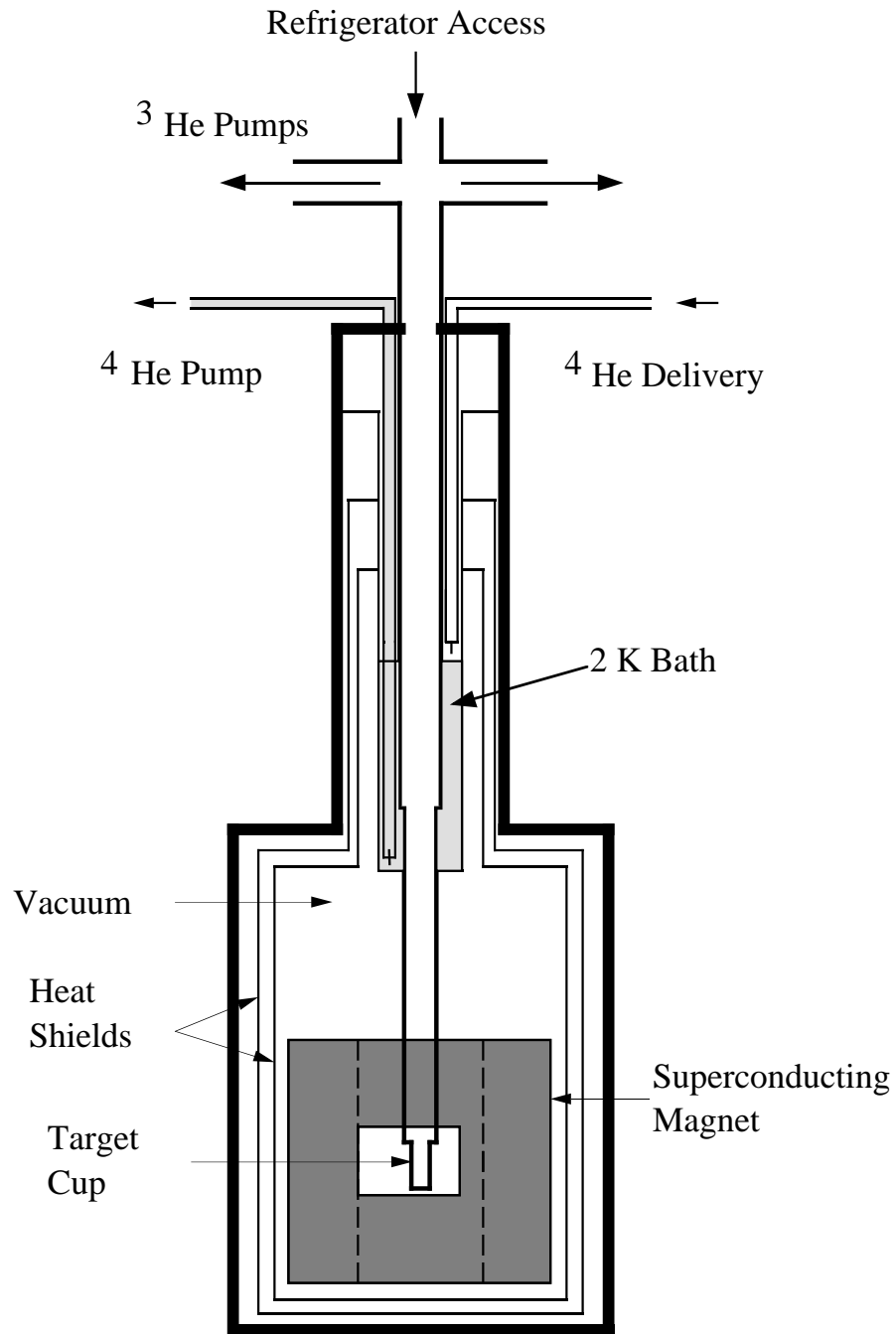
between the mixing chamber and the still that is created by their difference in temperature. ^3He atoms from the dilute phase in the mixing chamber travel up to the still because of the potential gradient. ^3He atoms cross the phase separation from the concentrated phase to the dilute phase and cooling occurs. The ^3He is recirculated and passes through a liquid nitrogen trap before re-entering the refrigerator. The incoming ^3He gas is condensed and is cooled by a heat exchanger before it enters the mixing chamber.

The dilution refrigerator used in this experiment is based on a PSI design [vdB90] and consists of three main components: the ^4He cryostat, the dilution refrigerator insert, and the target insert. This particular design is very modular, in that the dilution refrigerator is completely separate from the ^4He cryostat. The cryostat is cooled to 2 K by pumping on a bath of liquid ^4He and is described in Section 4.2.2. The dilution refrigerator condenser is in good thermal contact with the 2 K bath and condenses the returning ^3He . The dilution refrigerator cools the target to 250 mK. The refrigerator and target inserts fit inside the cryostat in a concentric manner and are described in Sections 4.2.3 and 4.2.4.

4.2.2 ^4He Cryostat

The cryostat is described extensively in [Rai97] and [Wal98] and will be briefly reviewed here. It consists of a vacuum jacket, a central 4.9 cm diameter stainless steel tube, the liquid helium dewar, and the 2.5 T split-coil superconducting magnet. The magnet is connected to the liquid helium space by two stainless steel bellows. The cryostat is shown in Figure 4.4.

The liquid helium space is filled every 30 minutes and average helium usage, including boiloff, pumping, and transfers is 1.6 *l/hr*. The liquid level is held between 7 and 13 cm via an automated transfer system. A superconducting liquid helium level sensor sends a signal to a process meter that has been programmed to control a 12 V solenoid valve. The solenoid controls the nitrogen gas that is used to open the pneumatic valve in the liquid helium transfer tube. When the valve opens, liquid helium is transferred from a commercial storage dewar to the cryostat dewar. The transfer ends when the level reaches

Figure 4.4: The ^4He cryostat.

a programmed upper limit and the sensor sends a signal to the process meter to close the nitrogen solenoid. The process meter also controls the backpressure in the storage dewar.

The ^4He bath is cooled to 2 K by pumping through a needle valve that is immersed in the bath. By pumping away the vapor above this small amount of liquid, the entire bath is slowly cooled. The 2 K pump is an Alcatel 2033 mechanical pump with a pumping speed of $35\text{ m}^3/\text{hr}$. The needle valve was adjusted to keep the inlet pressure to the pump at approximately 9.5 torr.

The central tube accepts the dilution refrigerator insert and acts as the ^3He pumping line. The upper half of the tube is surrounded by the 2 K bath and the heat exchange for the dilution refrigerator condenser takes place across this interface.

4.2.3 Dilution Refrigerator Insert

The dilution refrigerator insert consists of the condenser, flow impedance, a continuous heat exchanger, and mixing chamber and is based on the refrigerator described in [vdB90]. The insert has a 2.54 cm diameter axial opening that is sealed with the target insert (described in the next section). The condenser provides 250 cm^2 of surface area that is in good thermal contact with the 2 K bath through a close-tolerance slip fit. The condenser is constructed of two concentric stainless-steel cylinders that have been welded to flanges at the top and bottom of the cylinders. A flow impedance after the condenser ensures that the ^3He pressure is high enough for condensation. The flow impedance is a 65" long piece of 0.004" inner diameter copper-nickel tubing. The impedance of the tubing was determined by flowing 6 PSIG ^4He gas into the impedance and measuring the volumetric flow rate by collecting the gas in an upside down graduated cylinder that was submerged in water [Ric88]. The measured flow rate for 20 PSIG of ^4He gas was $3.5 \times 10^{-3}\text{ cm}^3/\text{s}$, which indicates an impedance of $4 \times 10^{11}\text{ cm}^{-3}$.

After passing through the impedance, the liquid enters a copper-nickel tube that is wrapped around the still several times and then enters the continuous heat exchanger. The heat exchanger is made of 0.028" inner diameter Teflon tubing with a 0.006" wall

thickness. Teflon tubing was used because its Kapitza resistance is four to six times smaller than that for copper-nickel or brass, which means that for the same amount of area, the heat exchanged will be four to six times larger for a Teflon exchanger [Fro92]. The heat exchange between two different media is inversely proportional to the Kapitza resistance, which depends on the nature of the media in contact. The Kapitza resistance for the ^3He -Teflon interface is almost an order of magnitude smaller than for ^3He -CuNi or ^3He -brass at 200 mK. A 4'6" length of the tubing was wrapped around a 3/32" diameter rod and heated for 10 minutes with a heat gun while being pressurized with 10 PSI nitrogen gas. The tubing was left on the rod overnight and was carefully transferred to the groove on the dilution refrigerator bobbin. The bobbin is made of Vespel SP22 and it has a spiral groove around it that is 0.16" wide and 0.16" deep. The heat exchanger rests in this groove and carries the ^3He down to a piece of copper-nickel tubing that delivers the liquid to the mixing chamber. The impedance of the flow impedance and the heat exchanger in series was found to be $11 \times 10^{11} \text{cm}^{-3}$.

The mixing chamber is a 0.812" x 0.812" copper box with no bottom. The liquid drips through the mixing chamber and into the bottom of the stainless steel tube surrounding the refrigerator insert. Because the target insert has sealed the axial space inside the refrigerator bobbin, the liquid flows up around the outside of the Vespel. The dilute phase that is flowing up the outside of the bobbin cools the incoming ^3He inside the Teflon tubing. The dilute phase rises to the level of the still which is heated to remain at 0.8 - 0.95 K. The still is a 4.24 cm tall stainless steel cylinder with 12 equally spaced holes drilled through its surface. The liquid passes through these holes into the central volume of the refrigerator, which is the pumping line. The vapor is pumped away by a 600 m^3/hr and a 300 m^3/hr roots blowers in series, backed by a hermetically sealed Alcatel 2063H mechanical pump.

4.2.4 Target Insert

The target insert supports the NMR cable, the microwave guide tube, the Vespel plug, and the target holder. The target holder is made from Kel-F, chosen for its lack of

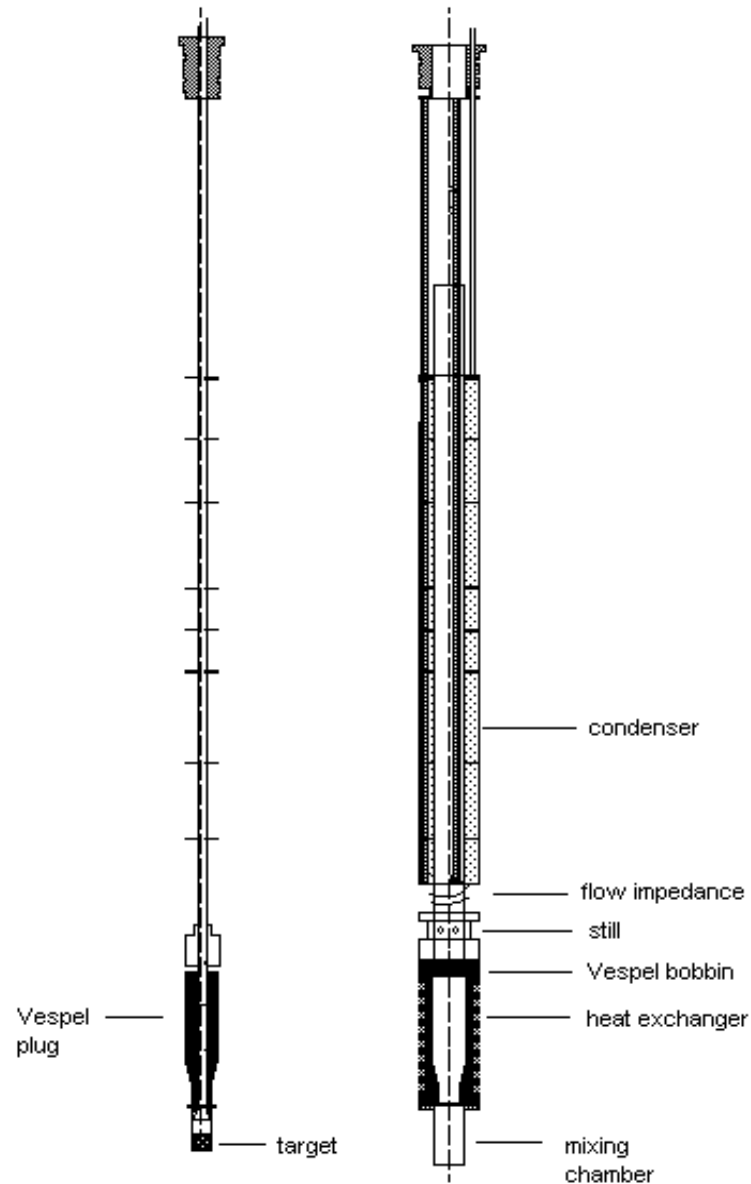


Figure 4.5: The target insert and dilution refrigerator insert. The target insert fits inside the dilution refrigerator and the Vespel plug separates the still from the mixing chamber, creating two distinct volumes. The microwave horn is located just below the Vespel plug and above the target material.

free polarizable hydrogens. The inner dimensions of the holder are 1.4 x 1.4 x 1.4 cm. The NMR coil is wrapped around the target holder and is held in place by grooves cut into the outside of the holder. Two grooves cut into the Vespel plug fit around alignment pins in the refrigerator and set the position of the target holder. The plug is used to separate the mixing chamber and the still, creating two distinct volumes. An excellent seal is created by a 5° conical step. The microwave guide tube goes through the center of the plug and terminates in the microwave horn directly above the target holder and material. Several copper heat shields are soldered along the central support tube and are cooled by the cold gas being pumped out. The dilution refrigerator and target insert are shown in Figure 4.5.

4.2.5 Operating Procedures and Characteristics

The ^4He cryostat is precooled with liquid nitrogen and is allowed to equilibrate overnight. The liquid helium transfer is started the next day, lasts about 2 1/2 hours, and uses approximately 30 liters of liquid. While the cryostat equilibrates at 4 K, the target material is loaded into the target cup. The target insert is inside a glove bag in a helium atmosphere and the beads are loaded into the target cup under liquid nitrogen. After the target insert is inside the cryostat, the refrigerator needs about 4 - 5 hours to equilibrate. Once the refrigerator is at 35 K, the 2 K valve is opened to pump on the ^4He bath. After about three hours, the bath reaches 2 K. Then the ^3He - ^4He mixture is condensed through the pumping line. Approximately 100 liters of ^3He - ^4He gas were used for the dilution refrigerator. This volume includes 5 liters of gas for the liquid nitrogen cold trap and 5 liters for the back of the 2063H sealed ^3He recirculating pump. The total volume of liquid in the refrigerator was 73 cm³. Recirculation is started by slowly opening a needle valve between the pumping line and the sealed mechanical pump. Until the returning gas started condensing, the condenser pressure was kept below one atmosphere. Once the needle valve was completely open, the main pumping valve was opened and the roots pumps were started. The still heater is a 100 Ω film resistor and provided 5 mW of heat to the still. It typically took about 30 minutes for the mixing chamber to cool from 1 K to 250 mK.

Table 4.1: Typical operating parameters for the dilution refrigerator.

Parameter	Typical Value
Condenser Pressure (torr)	600
Mixing Chamber (mK)	280
Still (K)	0.850
Condenser (K)	1.21
^3He Flow Rate (slpm)	0.25

The ^3He flow rate was measured using a Hastings model HFM mass flowmeter. Typical operating parameters are listed in Table 4.1.

4.3 Thermometry

Temperatures of various parts of the cryostat and refrigerator are measured with resistance thermometers. Ruthenium oxide resistors are used to measure the temperatures of the still and the dilute phase leaving the mixing chamber. Because the RuO near the mixing chamber has a high magnetoresistance and is not in the path of the microwaves, it can be used even when polarizing the target. A commercially calibrated germanium resistor (see Figure 4.6) is situated above the target cup and is immersed in liquid in the mixing chamber. This thermometer was used to calibrate the RuO with no microwaves and no magnetic field.

Two 1000 Ω platinum resistors located at the top and the bottom of the magnet are used for cooling from room temperature down to 70 K. A carbon glass resistor and a 476 Ω carbon Speer resistor are located on the ^4He dewar and are useful in the 2-6 K range. Another Speer is located on the condenser. Resistances are measured using a four lead resistance bridge and are read by a personal computer running Labview, which converts the resistance to temperature.

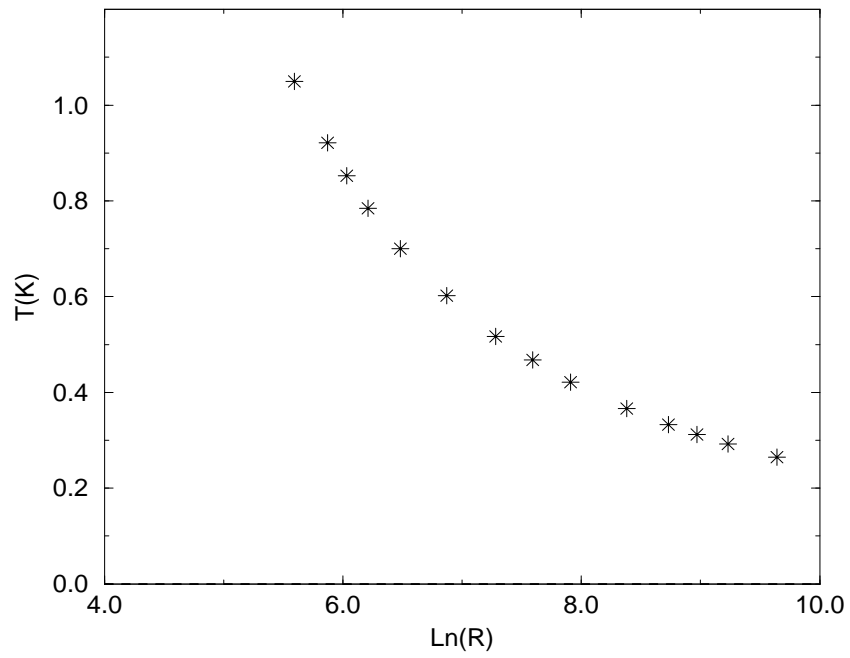


Figure 4.6: Calibration curve for the germanium resistance thermometer provided by the manufacturer. Temperature is calculated from the resistance using a Chebychev polynomial.

4.4 Target Material

The target material is fully deuterated 1,2-propanediol (D8) which has been doped with EHBA/CrV complex to provide free electrons for DNP. The dopant concentration for the samples used for taking neutron data was 5.1×10^{21} spins/ml. Other samples were prepared with 4×10^{19} spins/ml and will be discussed in Section 4.4.1. The material is prepared according to the recipe in [Kru79] and the procedure in [Cov02]. This preparation provides a high concentration of polarizable deuterons. The target material is frozen in 1 mm diameter beads and the beads are stored under liquid nitrogen. The target thickness was determined after each experiment by melting and weighing the target material.

4.4.1 Target Material Batch Comparisons

A batch of target material was made in July 2003 with a dopant concentration of 4×10^{19} spins/ml for the purpose of comparison to batches made with a higher dopant concentration. It was found that it was more difficult to tune the microwave frequency to get sizable target polarization and different klystron settings were tested in order to get a better microwave tune. However, no settings were found that reproduced the high polarization values from the target material with the higher spin concentrations. The polarizations with this target material were found to be 85% of the maximum achieved with the 10^{21} spins/ml samples.

4.4.2 Determination of Target Thickness

The target thickness was determined by weighing the target material after the experiment. The target was removed from the cryostat before the temperature reached 77 K and was kept under liquid nitrogen while the target cup was removed from the target insert. The entire target cup was then put into a 50 ml beaker and was sealed and the target beads were allowed to melt. The beaker and its contents were weighed and then the propanediol was cleaned out of the target cup and beaker. The beaker and its contents, minus the

propanediol, were weighed again and subtracted from the first measurement. The volume of the sample was calculated using measurements of the target cup and was found to be $2.729 \pm 0.006 \text{ cm}^3$ and the length in the beam direction was measured to be $1.405 \pm 0.003 \text{ cm}$.

The fraction of the dopant in the material (m_{dopant}/m_{total}) and the fraction of propanediol (m_{D8}/m_{total}) were determined by the chemical composition of the material (0.0356 g EHBA-CrV per 1 gram of propanediol). The propandiol contained eight deuterons per molecule and Avagadro's number of molecules per mole. The molecular weight of propanediol is 84.16 g.

The target area was calculated by dividing the target volume by the beam length and was found to be $(1.942 \pm 0.006) \times 10^{24}$ barns. Dividing the total number of deuterons by the area in barns gives the target thickness. Table 4.2 contains the data for the target thickness calculations for the October and December experiments.

Table 4.2: Values used in the calculation of the target thickness for each experiment.

Parameter	October	December
Total target weight (g)	2.0200 ± 0.0001	1.9434 ± 0.0001
Fraction of propanediol	0.965	0.965
Mass of propanediol (g)	1.950	1.875
Mass of EHBA/CrV (g)	0.0694	0.0668
Total number of deuterons	1.116×10^{23}	1.073×10^{23}
Total number of protons	2.49×10^{21}	2.39×10^{21}
Deuteron Target thickness (nuclei/barn)	0.0574 ± 0.0010	0.0553 ± 0.0010
Proton Target thickness (nuclei/barn)	0.00128 ± 0.00010	0.00123 ± 0.00010

The EHBA/CrV complex contained 22 protons per molecule and the proton thickness was calculated in the same manner as the deuteron thickness. Because of the presence of the protons, a correction must be applied to the calculation of $\Delta\sigma_L$ for the $\vec{n} - \vec{d}$ interaction. The ratio of $P_T x$ of the protons to the deuterons scaled the $\Delta\sigma_L$ value for the $\vec{n} - \vec{p}$ interaction and was subtracted from the value of $\Delta\sigma_L$ determined from the neutron

transmission experiment using

$$(\Delta\sigma_L)_d = \frac{2\bar{\epsilon}}{P_n P_d x_d} - \frac{P_p x_p}{P_d x_d} (\Delta\sigma_L)_p. \quad (4.11)$$

The second term on the right-hand side of the equation is referred to as the “correction term”, $(\Delta\sigma_L)_C$.

4.5 Nuclear Magnetic Resonance

Target polarization is measured using Nuclear Magnetic Resonance (NMR). A material’s magnetic susceptibility determines its response to RF radiation [Cra97] and can be measured with NMR. When the spin system is irradiated by an RF field at the Larmor frequency, it either absorbs some energy or the RF induces the system to emit energy. The inductance of the NMR coil is modified by the presence of the target material and is given by

$$L = L_o[1 + 4\pi Q\chi(\omega)] \quad (4.12)$$

where L_o is the inductance of the empty NMR coil, Q is the filling factor, and χ is the complex magnetic susceptibility $\chi(\omega) = \chi'(\omega) - i\chi''(\omega)$, which is a function of the applied RF field. Polarization is proportional to the imaginary part of the susceptibility, χ'' integrated over all frequencies,

$$P = K \int_0^\infty \chi''(\omega) d\omega \quad (4.13)$$

where K is a constant that depends on the nucleus being polarized.

The NMR electronics are shown in Figure 4.7 and consist of a Wavetek fast-switching frequency synthesizer controlled by the target PC running Labview, a tuned LRC circuit of the Liverpool design [Cou93], a coaxial cable, and the NMR coil. The Liverpool circuit was shielded with a copper box which was kept at 10° C with a temperature controlled recirculating water loop. The diode output of the NMR circuit was used. The NMR coil is four turns of bare copper wire that are wound around the target cup. It is connected to a cryogenic coaxial $\lambda/2$ cable. This cable is connected at room temperature to the NMR

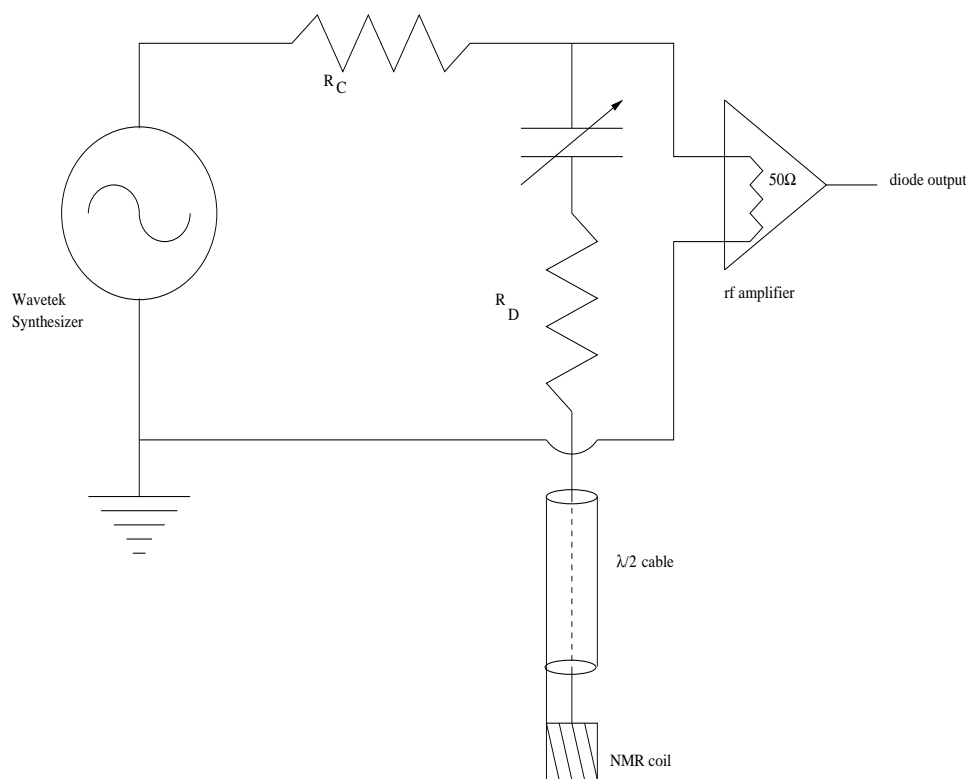


Figure 4.7: The TUNL polarized deuteron target NMR system.

circuit and is made of UT85 cryogenic cable with PTFE insulator and a copper tube outer conductor. The circuit response is measured and displayed with Labview. The LRC circuit is tuned to 16.35 MHz, which is the Larmor frequency of deuterons in a 2.5 T magnetic field. The frequency is swept ± 300 MHz around the resonant frequency.

4.5.1 Signal Acquisition

Normally, at least one NMR signal was saved for every neutron run of 1024 8-step spin-flip sequences. A measurement of the circuit response (Q-curve) is made with no microwaves, saved to the hard drive of the PC, and used for background subtraction during data acquisition. The Labview program saves each signal as a data file, which is used for off-line analysis. The data file contains the signal as it was recorded on-line, along with a header that contains the name of the background that was used online, the time, the gain,

the base frequency, the 10 torr baratron, the temperature of the RuO, and the number of sweeps. A typical signal was averaged over 1300 sweeps. A third order polynomial fit was applied to the first and last 60 channels of the sweep in order to get a more accurate calculation of the online signal areas.

4.5.2 Shape Fitting and Signal Analysis

The Fortran program dnmrarea3 reads and removes the header from the data file, does a third order least-squares polynomial fit to the wings of the signal, subtracts the fit, and calculates the area of the signal. This area is called the off-line area. A new data file is created containing subtracted signal. Because of the deuteron's small magnetic moment, its thermal equilibrium signal is hard to observe. Therefore, the deuteron polarization is determined from the signal asymmetry ratio. The lineshape is fitted according to the procedures in [Ham81] and [Spe87].

The energy splitting of a deuteron in a magnetic field is shown in Figure 4.8. The deuteron is a spin 1 nucleus and has three magnetic substates: $m = -1, 0, \text{ and } 1$. If only the magnetic field is considered, then the level splitting due to the interaction of the deuteron's magnetic moment, μ_D , with the field B is

$$\Delta = \mu_d B. \quad (4.14)$$

However, the deuteron has an electric quadrupole moment that interacts with the electric field gradient in the solid and produces an additional splitting,

$$\delta = eqQ(1 - 3\cos^2\theta) \quad (4.15)$$

where e is the electronic charge, q is the electrical field gradient, Q is the quadrupole moment, and θ is the angle between the magnetic field and the electric field gradient. The populations of the three substates p_- , p_0 , and p_+ determine the nuclear polarization. The deuteron vector polarization is defined as

$$P_d = \langle I_z \rangle = p_+ - p_- \quad (4.16)$$

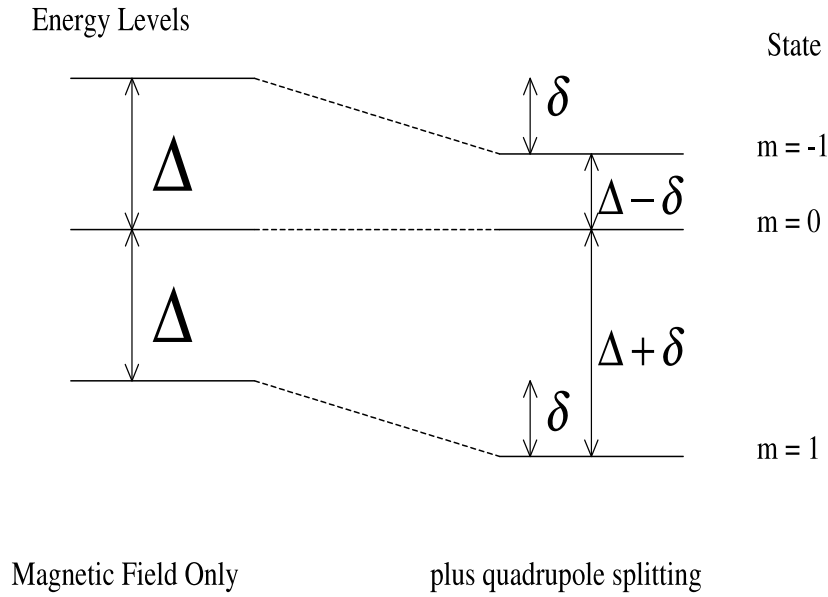


Figure 4.8: Energy-level splitting of a deuteron in a magnetic field.

assuming the populations are normalized by

$$p_+ + p_0 + p_- = 1. \quad (4.17)$$

It is assumed that the deuteron system is in internal equilibrium and can be described by a spin temperature, T_s . This assumption has been proved to be accurate by [Bor71]. In this equilibrium case, the relative populations of the magnetic substates are given by the Boltzmann distribution,

$$r = \frac{p_+}{p_0} = \frac{p_0}{p_-} = e^{\frac{h\nu}{kT_s}} \quad (4.18)$$

where p_0 , p_+ , p_- are the populations of the three substates, ν is the deuteron Larmor

frequency, h is Planck's constant, and k is Boltzmann's constant. To determine the polarization, the ratio r must be determined from the deuteron signal lineshape. The deuteron lineshape consists of two peaks corresponding to the $1 \leftrightarrow 0$ and the $0 \leftrightarrow -1$ transitions. The molecules are randomly oriented with respect to the magnetic field and this causes the two peaks to overlap each other. The ratio of the transition intensities I_+ and I_- is

$$\frac{I_+}{I_-} = \frac{p_+ - p_0}{p_0 - p_-} = \frac{r - 1}{1 - 1/r} = r. \quad (4.19)$$

Once r has been determined, the deuteron vector and tensor polarizations can be determined from Equation 4.18 and the normalization condition given in Equation 4.17:

$$p_z = p_+ - p_- = \frac{r^2 - 1}{r^2 + r + 1} \quad (4.20)$$

$$p_{zz} = 1 - p_0 = \frac{r^2 - 2r + 1}{r^2 + r + 1} \quad (4.21)$$

Because the propanediol molecule has eight deuterons, the deuteron NMR signal is actually a combination of two transitions in two different bonds. The C-D bond provides a different quadrupole coupling than the O-D bond and the deuterons in the O-D bond produce the shoulders just outside of the peaks.

The fitting program uses five free parameters to perform a least-squares fit to the experimental lineshape. These parameters are the polarization, a scale factor, two constants for fitting a polynomial to the background, and a channel offset. This fitting method takes into account the dispersive part of the susceptibility, which affects the signal lineshape significantly [Spe87]. This is done by calculating χ' from the Kramers-Kronig relations. The impedance of the NMR circuit, including the cable, is also calculated and used in the theoretical lineshape. A typical NMR signal is shown in Figure 4.9. The central frequency is 16.35 MHz.

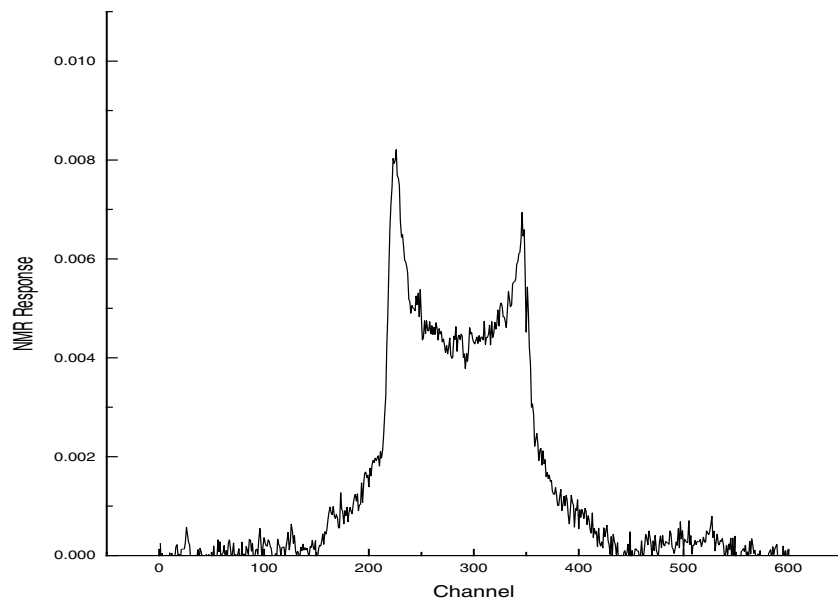


Figure 4.9: A plot of a typical NMR signal.

Chapter 5

Data Acquisition

This chapter will discuss the neutron detectors and collimation and the associated electronics. The main detector will be discussed in Section 5.1.1 and the monitor detector will be described in Section 5.1.2. The data acquisition electronics are discussed in Section 5.2.

5.1 Neutron Detectors and Electronics

5.1.1 Zero Degree Main Detector

The zero degree main neutron detector is located approximately 240 cm behind the polarized deuteron target. The detector views a 2.0 ms solid angle defined by a polyethylene collimator located directly behind the target cryostat. A schematic of the collimator and detectors is seen in Figure 2.2. The collimator was used to insure that only neutrons that passed through the target material were detected. The entrance to the collimator was located 19 cm from the neutron production cell and had an opening that was 1.2×1.2 cm. The collimator bore tapered to an exit that was 9×9 cm and 128.3 cm downstream. Behind the collimator, a stack of wax blocks shielded the neutron detector from the fringing fields of the superconducting magnet.

The detector itself is contained in a polyethylene block and is a scintillation detector

optically coupled to a photomultiplier tube (PMT). The scintillating material is a proton-rich organic liquid containing linked or condensed benzene-ring structures [Leo94]. The neutrons are detected by scattering from the protons in the scintillator material. The recoiling protons interact with the scintillation material via excitation. The scintillation light arises from transitions made by the free valence electrons of the molecules. This light strikes the photocathode of the PMT and causes electrons to be emitted. A chain of dynodes held at increasing potentials amplified the electron current via photomultiplication. The current was collected at the anode. The PMT was biased to -2200 V.

Because gamma rays are also created by the neutron production reactions and are detected by the scintillator, pulse-shape discrimination was used to distinguish these gammas from neutrons. The overall decay time of the detector signal depends on the type of ionizing radiation. The neutrons had a longer decay time and only detector events which met this criteria were counted and used in the neutron asymmetry calculation.

The production cell, polarized target, collimator, and detector were aligned using radiography. An x-ray film was placed at the exit of the collimator and a copper block with a hole through its center was placed in the target cup. The cryostat was cooled to 77 K so that the majority of thermal contraction had taken place. The film was exposed to radiation produced with 1.5 μA of 4 MeV deuteron beam from the Direct Extraction Negative Ion Source (DENIS) incident on the neutron production cell. The image of the hole in the copper target could be clearly seen on the film and confirmed the alignment of the experimental apparatus. This was important because any neutrons that were detected that had not passed through the target material would dilute the measured asymmetry.

5.1.2 Monitor Detector

A neutron monitor detector was placed between the neutron production cell and the polarized target cryostat to measure the incident neutron flux for the ${}^2\text{H}(\vec{d}, \vec{n}){}^3\text{He}$ reaction. This detector measured the neutron asymmetries due to deuteron beam current asymmetry, deuteron beam tensor polarization, and differences in polarization between the two states.

The neutron monitor asymmetry was measured and subtracted from the main detector asymmetry to remove beam current and neutron production effects.

The monitor detector consisted of a small ($2.5 \times 1.3 \times 2.5$ cm thick) liquid organic scintillator coupled to a photomultiplier tube by a one meter long light pipe. The light pipe moved the PMT away from the magnetic field produced by the magnet in the target cryostat. The light pipe had a 90° bend so that the pipe and PMT mounted above the beam line. The monitor PMT was biased to -1900 V and was very similar to the PMT used for the main detector. Events in the monitor detector were not pulse-shape analyzed, but had to meet an energy threshold.

5.2 Data Acquisition Electronics

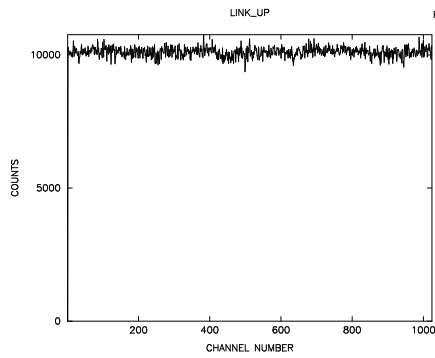
NIM and CAMAC modules were used for data acquisition and were interfaced to a μ -VAX computer via a multiple branch driver (MBD). The data acquisition software package XSYS [Gou81] was used for sorting and online analysis of data.

The main neutron detector events were pulse-shape analyzed by a Link 5020 PSD [Lin] module which could also set upper and lower thresholds. The Link module had separate outputs for gammas and neutrons, in addition to an output that displayed both sets of signals. The separate neutron and gamma signals were sent to a Phillips 794 gate and delay generator and then to a 706 veto module. Because the Link module needs 300 ns to differentiate between gammas and neutrons, a dead-time correction is applied to the number of detected neutron events. The live-time output of the Link module is combined with the signal from the 100 kHz pulser so that “gated” and “ungated” pulser signals are produced. The live-time output is inhibited when the Link is busy and a dead-time correction is calculated. The signals pass through the veto module and into the scaler.

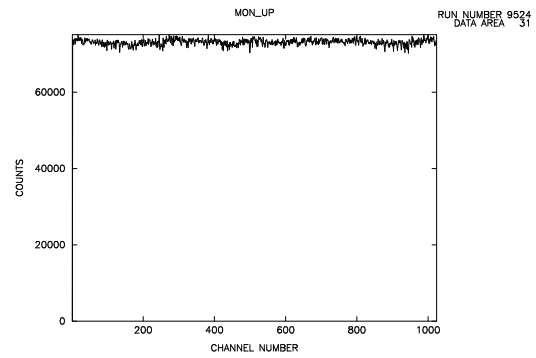
Data are vetoed during the 2 ms before and the 5 ms after the beam spin flip to allow the polarization to stabilize. The beam polarization is flipped at a rate of 10 Hz by the TUNL Spin State Controller (SSC). It controls the rf transition units in the ABPIS through

a set of fiber optic cables and produces signals specifying the spin state for the purpose of data sorting. An analog-to-digital converter (ADC) reads the spin-routing signals and alerts the MBD that a spin-reversal has occurred. The computer reads all the CAMAC scalers and stores the data according to spin-state. The beam polarization is flipped in a special 8-step sequence (+ - - + - + + -) which helps eliminate any detector drifts that are linear or quadratic in time. Precision timing is used to insure that the same amount of time is spent in each spin state. The SSC is driven by an external clock input from the data acquisition computer. At the end of each 8-step spin-flip sequence, the SSC decrements a count-down scaler, which was preset by XSYS to 1024. When the countdown scaler reaches zero, the “run” ends, data acquisition is inhibited, data are saved to disk, and neutron asymmetries are calculated for the run. Each run lasts approximately 15 minutes. Data are stored in the computer in histograms, which, for each spin-state, are filled up channel by channel, producing histograms of neutron counts vs. time. Each time channel corresponds to one 8-step spin-flip sequence. Data collection is also inhibited when the beam current drops below a user-determined level. A beam current integrator (BCI) is used to calculate a beam current asymmetry for offline correction of neutron asymmetries. Sample online histograms of main, monitor, and BCI data areas are shown in Figure 5.1 for spin-up beam polarization. Similar histograms were recorded for spin-down beam polarization. The deuteron beam current for this particular run was 750 nA.

Items of the data acquisition software are recorded in the appendices. The program `npinit.com` (Appendix D) was used to allocate the data areas for the histograms and set up the rest of the software. Appendix E contains the code `go.com`, which is used to start the data acquisition process. The program `neutasym.for` is found in Appendix F and is used to calculate the average asymmetry for each run and the standard deviation. After each run ends, the asymmetries are written to a file and are averaged over all of the previous runs for that particular target polarization state.



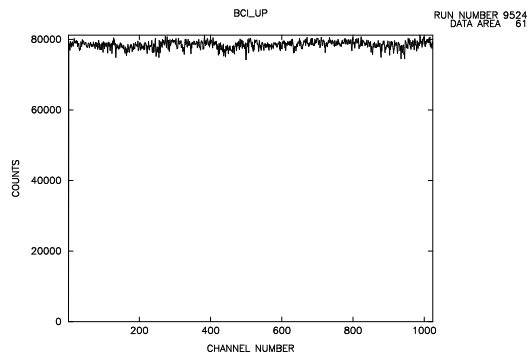
DT81 8-MAY-2004 1405



DT81 8-MAY-2004 1407

(a) Spin-up neutron counts in the main detector.

(b) Spin-up neutron counts in the monitor detector.



DT81 8-MAY-2004 1409

(c) Histogram of BCI counts.

Figure 5.1: Online histograms of main and monitor detectors and BCI counts for spin-up beam polarization.

Chapter 6

Data and Analysis

The determination of $\Delta\sigma_L$ required several different measurements. This chapter summarizes the data collected and the analysis that was performed on each data set. Experiments were performed in October and December 2003. The October experiment produced the 5.0, 6.88, and 9.0 MeV data sets and the neutron polarimetry. The 1.18 MeV and the proton polarimetry data were taken during the December experiment. Section 6.1 tabulates the beam polarization data and Section 6.2 details the target polarization measurements. The neutron asymmetries are found in Section 6.3 and the calculation of $\Delta\sigma_L$ is found in Section 6.4.

6.1 Beam Polarization

In this experiment, neutron beam polarization was calculated from proton beam polarization or it was measured directly, depending on which neutron production reaction was used.

6.1.1 Proton Beam Polarization

Proton beam polarimetry was performed during the data run in December 2003. The proton beam polarization is determined from the left-right elastic scattering asymme-

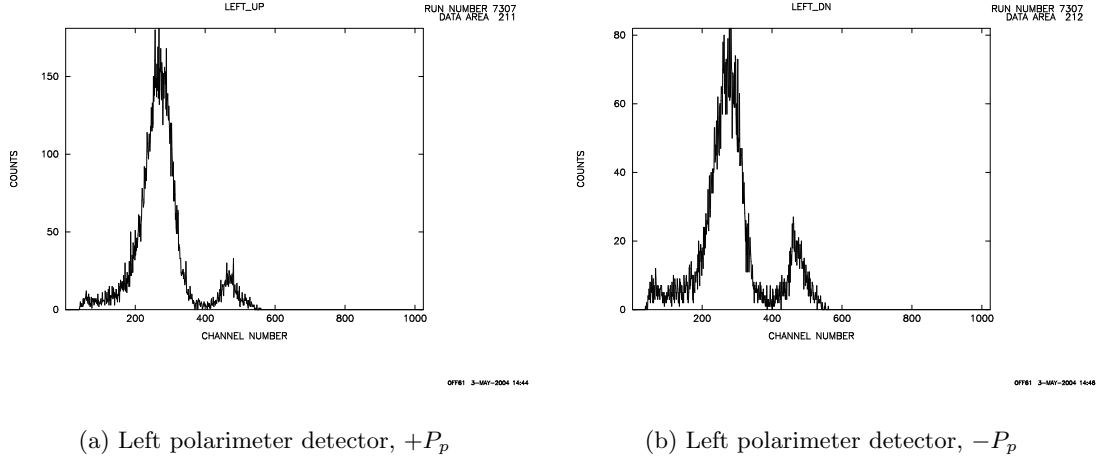


Figure 6.1: Energy spectra for 2.52 MeV protons elastically scattered from ^4He into the left polarimeter detector for spin-up and spin-down beam polarizations. The smaller peak at higher energy is produced by protons scattering from Havar.

Table 6.1: Proton beam polarization measurements taken during the $E_n = 1.18$ MeV experimental run in December 2003.

E_p (MeV)	Angle	Run #	ϵ_p	A_y	P_p
2.52	75°	7307	0.363 ± 0.007	0.721 ± 0.007	0.503 ± 0.010
2.52	75°	7308	0.352 ± 0.007	0.721 ± 0.007	0.488 ± 0.010
average:					0.495 ± 0.007

try from the $^4\text{He}(\vec{p}, p)^4\text{He}$ reaction. The axis of the beam polarization was rotated to be transverse to the beam momentum by using the Wien filter in the ABPIS. Each detector counts spin-up and spin-down scattered protons. Sample spectra are shown in Figure 6.1 for spin-up and spin-down protons detected by the left detector. The neutron beam polarization is then calculated from the proton polarization and the polarization transfer coefficient for the $^3\text{H}(\vec{p}, \vec{n})^3\text{He}$ reaction. The data for the proton polarimetry are found in Table 6.1. Uncertainty in A_y comes from estimates in the error in the proton beam energy and the angle of the detectors. As mentioned on Section 3.3, we do not include the 2% systematic error from [Sch71].

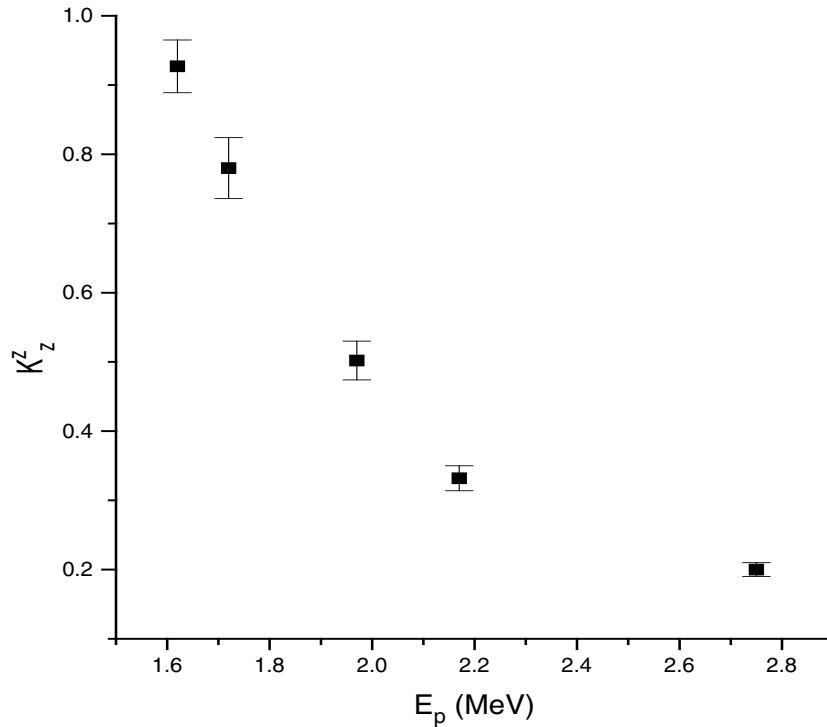


Figure 6.2: $K_z^{z'}(0^\circ)$ data from [Wal98] for the ${}^3\text{H}(\vec{p}, \vec{n}){}^3\text{He}$ neutron production reaction.

6.1.2 Neutron Beam Polarization

After the proton beam polarization was measured, the neutron polarization was calculated. The longitudinal polarization transfer coefficient, $K_z^{z'}(0^\circ)$, was found from the data in [Wal98], shown in Figure 6.2. From this data set, $K_z^{z'}(0^\circ)$ for $E_p = 1.98$ MeV was found to be 0.502 ± 0.028 . The neutron beam polarization is the product of the proton beam polarization and $K_z^{z'}(0^\circ)$ and was found to be 0.248 ± 0.014 .

Proton polarimetry data were also taken with the beam polarization axis in the longitudinal direction. This was done to check for a transverse polarization component and to verify magnetic field settings in the Wien filter. Data from this test can be found in

Appendix C.

The neutron beam polarization was measured directly for the 5.0, 6.88, and 9.0 MeV data. The measurement was performed for $E_n = 6.88$ MeV with the polarization axis transverse to the beam momentum. A left-right scattering asymmetry was measured. Spectra for the left neutron polarimeter detector are shown in Figure 6.3 for spin-up and spin-down detected neutrons. PSD was performed to separate neutrons from gammas. Data from this measurement are shown in Table 6.2. Because the polarization transfer coefficients and the analyzing powers for the longitudinal and transverse ${}^2\text{H}(\vec{d}, \vec{n}){}^3\text{He}$ reactions are different, the measured transverse neutron polarization for $E_n = 6.88$ MeV was used to calculate P_z and P_{zz} for the deuteron beam using the known analyzing power, $A_{zz}(0^\circ)$, and the known transverse polarization transfer coefficient, $K_y^{y'}(0^\circ)$. P_z and P_{zz} were assumed to be equal. Then, the longitudinal neutron polarization was calculated for neutron energies of 5.0, 6.88, and 9.0 MeV using the longitudinal polarization transfer coefficients $K_z^{z'}(0^\circ)$ and analyzing powers $A_{zz}(0^\circ)$ (Table 6.3).

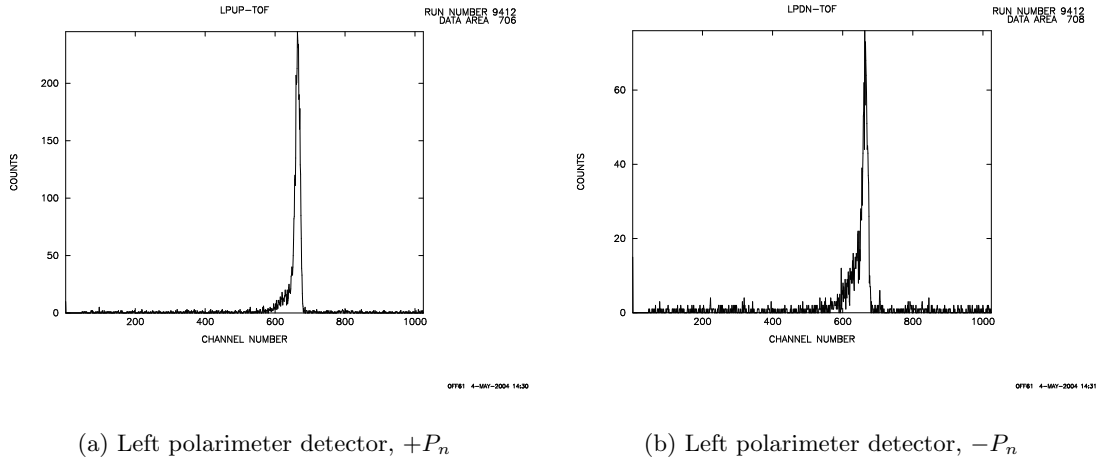


Figure 6.3: Energy spectra for 6.88 MeV neutrons elastically scattered from ${}^4\text{He}$ into the left polarimeter detector for spin-up and spin-down beam polarizations.

There is some uncertainty about the value of $K_z^{z'}(0^\circ)$ for incident deuteron energies less than 3.25 MeV because it has not been measured below that energy. Calculations have been made [Hal98], but have not been experimentally verified. A fit to the lowest energy

Table 6.2: Neutron beam polarization measurements taken during the experimental run in October 2003 for $E_n = 6.88$ MeV with the polarization axis transverse to beam momentum.

E_n (MeV)	Angle	Run #	ϵ_n	A_y	P_n
6.88	116°	9409	0.520±0.040	0.92±0.01	0.565±0.043
6.88	116°	9410	0.527±0.034	0.92±0.01	0.572±0.037
6.88	116°	9411	0.549±0.025	0.92±0.01	0.596±0.028
6.88	116°	9412	0.551±0.020	0.92±0.01	0.598±0.022
6.88	116°	9558	0.479±0.063	0.92±0.01	0.520±0.068
6.88	116°	9559	0.509±0.024	0.92±0.01	0.553±0.026
6.88	116°	9560	0.514±0.024	0.92±0.01	0.558±0.026
average:					0.578±0.014

Table 6.3: Longitudinal neutron beam polarization calculations for data taken during the October 2003 experiment using the ${}^2\text{H}(\vec{d}, \vec{n}){}^3\text{He}$ reaction. The first row for $E_d = 1.78$ is calculated using Hale's predictions of $K_z^{z'}(0^\circ)$ and $A_{zz}(0^\circ)$. The second row value of $K_z^{z'}(0^\circ)$ is from a fit to Salzman's $K_z^{z'}(0^\circ)$ data and the $A_{zz}(0^\circ)$ value is from Lisowski. The rest of the $K_z^{z'}(0^\circ)$ values are from [Sal73] and the $A_{zz}(0^\circ)$ values are from [Lis75].

E_d (MeV)	E_n (MeV)	$K_z^{z'}(0^\circ)$	$A_{zz}(0^\circ)$	P_{zz}	P_n
1.78	5.00	0.419±0.020	-0.622±0.020	0.651±0.023	0.511±0.029
1.78	5.00	0.345±0.123	-0.520±0.024	0.651±0.023	0.404±0.144
3.60	6.88	0.403±0.020	-0.474±0.007	0.651±0.023	0.464±0.027
5.79	9.00	0.455±0.014	-0.465±0.013	0.651±0.023	0.521±0.022

data in [Sal73] produces a significantly different value than [Hal98]. Both values have been included in Table 6.3 for comparison. It's important to note that [Wal98] used Hale's $K_z^{z'}(0^\circ)$ prediction for 5 MeV neutron energy, but Walston's result for $\Delta\sigma_L$ does not validate the prediction. Using the value of $K_z^{z'}(0^\circ)$ from the fit does not alter Walston's $\Delta\sigma_L$ result significantly. A plot of $K_z^{z'}(0^\circ)$ vs. deuteron energy for Hale's predictions and the lowest energy data from [Sal73] is shown in Figure 6.4. While it is true that Salzman's 3.28 MeV data point agrees well with Hale, Salzman's other two data points suggest a significantly different behavior than the predictions. Also, the transverse polarization transfer coefficient for the ${}^2\text{H}(\vec{d}, \vec{n}){}^3\text{He}$ reaction, $K_y^{y'}(0^\circ)$, continually decreases below 4 MeV [Lis75] and shows

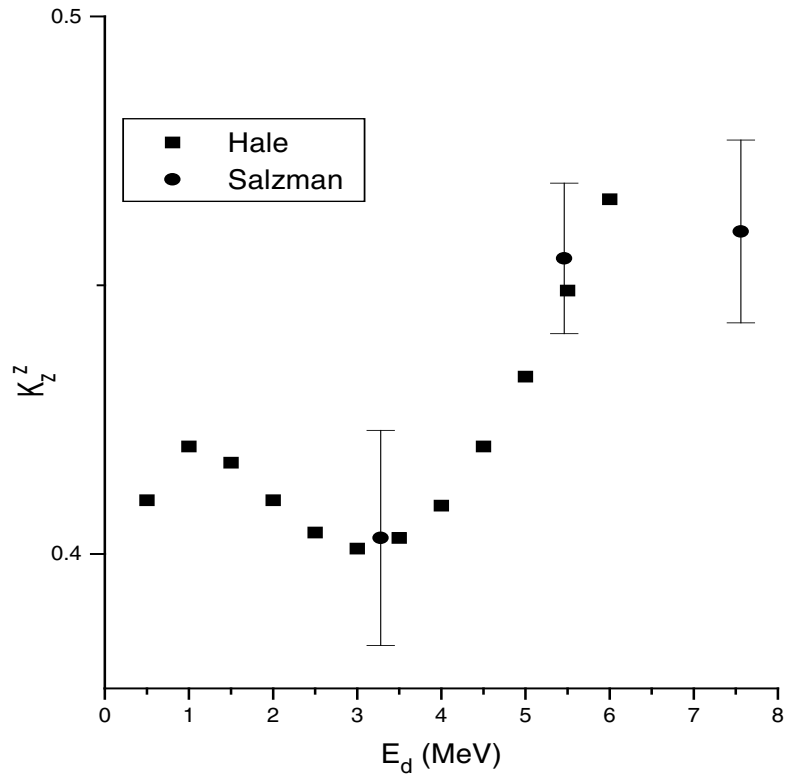


Figure 6.4: Comparison of $K_z^{z'}(0^\circ)$ predictions from [Hal98] with data from [Sal73] for the ${}^2\text{H}(\vec{d}, \vec{n}){}^3\text{He}$ neutron production reaction.

no “hump” like Hale’s prediction of $K_z^{z'}(0^\circ)$.

6.2 Target Polarization

The target polarization was monitored during the neutron transmission experiments using NMR. Signals were saved during the data acquisition and were analyzed offline. Typically, one signal was saved per 15 minute data run. The signals were analyzed according to the procedure in Section 4.5.2. The NMR measurement of the target polarization was calibrated by a low-energy neutron transmission experiment. The transmission asymmetry

was measured and a theoretical value of $\Delta\sigma_L$ was used to calculate the spin temperature of the target by substituting Equations 4.6 and 4.7 for P_p and P_d in Equation 4.11. The theoretical value for $(\Delta\sigma_L)_d$ used in the normalization was obtained from a fit to the CD Bonn NN calculations. It should be noted, however, that if one uses the average of $\Delta\sigma_L$ obtained from the NN interactions and the NN+3NF interactions found in [Wit99], then the result changes by only 0.02%. The value of $(\Delta\sigma_L)_p$ was determined from a fit to the $\vec{n} - \vec{p}$ $\Delta\sigma_L$ data in [Wal98]. Then the proton and deuteron polarizations were calculated and the deuteron polarization was used to calculate the polarization per area constant for calibration of the NMR signals.

Table 6.4: Calculation of the spin temperature of the target material. The calculation was performed numerically by Maple. Data are from the December 2003 experiment with $E_n = 1.18$ MeV and asymmetries are $\times 10^{-4}$.

Parameter	7165–7231	7232–7306
$(\Delta\sigma_L)_d$ (mb)	-2170	-2170
$\bar{\epsilon}$	-12.3 ± 3.5	-30.2 ± 4.4
P_n	0.248 ± 0.014	0.248 ± 0.014
x_d (b^{-1})	0.0552 ± 0.0010	0.0552 ± 0.0010
x_p (b^{-1})	0.00123 ± 0.00010	0.00123 ± 0.00010
$(\Delta\sigma_L)_p$ (mb)	3082	3082
T_{ss} (mK)	5.39	2.24

Table 6.5: Calculation of NMR calibration constant. Data are from the December 2003 experiment.

Data Runs	T_{ss} (mK)	P_d	P_p	\bar{A}	P_d/\bar{A}
7165–7231	5.39	0.096	0.441	0.488 ± 0.019	0.198 ± 0.019
7232–7306	2.24	0.228	0.814	0.775 ± 0.020	0.294 ± 0.020
weighted average:					0.246 ± 0.013

The calculation of P_T/A is found in Table 6.5. Once the polarization per area constant was known, the average target polarization for the October neutron transmission experiment could be calculated. Table 6.6 contains the calculation of the target polarization

Table 6.6: Calculation of average target polarizations for October experiment.

E_n (MeV)	$ \bar{A} $	P_d	A_d	T_{ss} (mK)	P_p
5.0	1.23 ± 0.01	0.302 ± 0.016	0.0696 ± 0.0050	1.67 ± 0.14	0.910 ± 0.022
6.88	1.06 ± 0.01	0.260 ± 0.014	0.0513 ± 0.0040	1.95 ± 0.14	0.864 ± 0.024
6.88	0.897 ± 0.036	0.220 ± 0.014	0.0366 ± 0.0030	2.33 ± 0.23	0.799 ± 0.061
9.0	1.20 ± 0.01	0.295 ± 0.015	0.0663 ± 0.0040	1.71 ± 0.13	0.903 ± 0.025

Table 6.7: Summary of neutron asymmetry measurements.

E_n (MeV)	Use	Runs	P_T Sequence
1.18	P_T/A	7165–7306	+ - + -
5.00	$\Delta\sigma_L$	9470–9517	- +
6.88	$\Delta\sigma_L$	9350–9469	+ - + -
9.00	$\Delta\sigma_L$	9518–9556	+ -

and alignment. The alignment is non-zero, but does not affect the measurement.

6.3 Neutron Asymmetries

Neutron transmission asymmetries were measured for four different energies. Data were taken in two week-long blocks of beam time, in October and December 2003. Table 6.7 lists the neutron beam energy, the observable, the run numbers, and the target polarization sequence for each measurement. The 1.18 MeV data were used to calibrate the NMR measurement of the target polarization. By using a theoretical value for $\Delta\sigma_L$ and measuring the neutron transmission asymmetry, we calculated a constant for converting NMR signal area to deuteron polarization.

As mentioned in Section 5.2, neutron counts were stored in histograms for each spin-state. These histograms are used for the asymmetry calculation. The first step in the analysis is the elimination of any 8-step spin-flip sequences that did not include equal times in spin-up and spin-down polarizations. Then a channel-by-channel raw asymmetry

is calculated, along with monitor- and BCI-normalized asymmetries. Then the data are processed by a program which makes cuts that depend on user-defined ranges. This is useful for removing spin-flip sequences which contain abnormal beam current, monitor detector, or neutron production asymmetries. Table 6.8 lists the lower and upper allowed limits on the BCI, monitor, and neutron asymmetries for the October 2003 data. In the next step, the monitor detector asymmetry is subtracted from the main detector asymmetry and the difference is plotted vs. the BCI asymmetry. The data are fit to a line and the intercept of the line (where $\epsilon_I = 0$) is the asymmetry for that block of runs. A typical plot of neutron asymmetry vs. BCI asymmetry is shown in Figure 6.5. For the 1.18 MeV data, the raw asymmetries were calculated because the ${}^3\text{H}(\vec{p}, \vec{n}){}^3\text{He}$ reaction was used and the proton beam does not have any tensor polarization.

Table 6.8: Acceptable ranges for October 2003 BCI and monitor asymmetries and neutron yield asymmetry. The neutron yield asymmetry is calculated from the average of the BCI normalized spin-up and spin-down counts in the Link module.

ϵ_I	ϵ'_n	ϵ_N
-0.02–0.02	-0.1–0.1	-0.1–0.1

Table 6.9: Neutron asymmetry data. All asymmetries are $\times 10^{-4}$.

E_n (MeV)	$\epsilon_n^+ \pm \sigma_{\epsilon_n^+}$	$\epsilon_n^- \pm \sigma_{\epsilon_n^-}$	$\bar{\epsilon}_n \pm \sigma_{\bar{\epsilon}_n}$
1.18	-0.717 ± 4.8	23.93 ± 5.3	-12.31 ± 3.5
1.18	-27.15 ± 3.8	32.22 ± 8.1	-29.68 ± 4.4
5.00	-14.1 ± 0.85	27.3 ± 0.76	-20.7 ± 0.57
6.88	-12.6 ± 0.38	13.5 ± 0.54	-13.0 ± 0.33
6.88	-14.9 ± 0.53	3.5 ± 0.49	-9.22 ± 0.36
9.00	-18.6 ± 0.57	-4.86 ± 0.60	-6.87 ± 0.41

Data were taken for 6-8 hours per target polarization state and approximately 25 runs were taken in each state. When target polarization is flipped, it typically takes around 2 hours to achieve significant target polarization in the new state. Data that were taken during this 2 hour period were not used in calculations of $\Delta\sigma_L$.

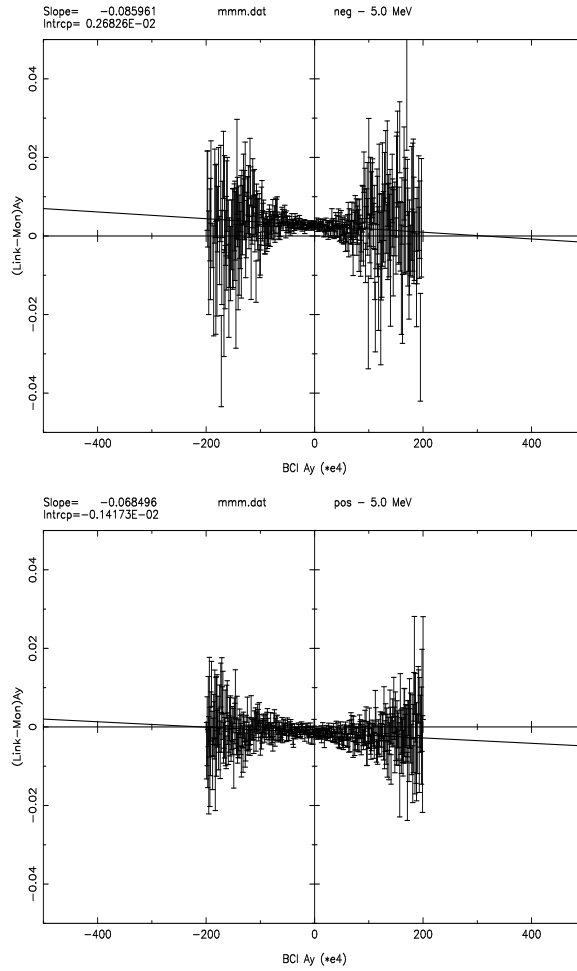


Figure 6.5: Plot of $(\epsilon_n - \epsilon'_n)$ vs. ϵ_I and the least squares fit, which gives the slope and intercept above the plot. The top plot is for negative target polarization and the bottom is for positive.

The neutron asymmetries for each target polarization state were averaged over the runs taken in that state. Separate neutron transmission asymmetries are calculated for positive and negative target polarizations, respectively. The average asymmetry is calculated using Equation 2.25 and is used in the calculation of $\Delta\sigma_L$. Table 6.9 contains the asymmetries for positive and negative target polarizations and the average for each neutron energy. The difference in the values for the + state at 1.18 MeV is due to the large difference in target polarizations (See Table 6.5).

6.4 Calculation of $\Delta\sigma_L$

The calculation of $\Delta\sigma_L$ was performed for each energy using Equation 4.11. Table 6.10 contains the data used to calculate the correction to $\Delta\sigma_L$ from the protons in the EHBA/CrV in the target material. Table 6.11 lists the values for each parameter that was used in the calculation, along with the values of $\Delta\sigma_L$.

A plot of $\Delta\sigma_L$ vs. E_n is shown in Figure 6.6 along with the calculations from [Wit99]. Our data agree well with predictions at 6.88 and 9.0 MeV but are not precise enough to distinguish between two and three body force effects. The error bars on the 5.0 MeV data point are due to the uncertainty in the polarization transfer coefficient, $K_z^{z'}(0^\circ)$, for the ${}^2\text{H}(\vec{d}, \vec{n}){}^3\text{He}$ reaction at 1.78 MeV incident deuteron energy. Figure 6.7 includes the 1.18 MeV calibration point normalized to the average of the values calculated in [Wit99]. Figure 6.8 shows the data taken at TUNL in 1998-99 along with the new measurement.

Table 6.10: Calculation of the correction term $(\Delta\sigma_L)_C$ due to the protons in the target material.

E_n (MeV)	$x_d(b^{-1})$	P_d	$x_p(b^{-1})$	P_p	$(\Delta\sigma_L)_p$ (mb)	$(\Delta\sigma_L)_C$ (mb)
5.00	0.0574 ± 0.001	0.302 ± 0.016	0.00128 ± 0.0001	0.910 ± 0.022	94.0 ± 10.8	6.3 ± 0.9
6.88	0.0574 ± 0.001	0.260 ± 0.014	0.00128 ± 0.0001	0.864 ± 0.024	-1.96 ± 1.78	-0.14 ± 0.12
6.88	0.0574 ± 0.001	0.220 ± 0.014	0.00128 ± 0.0001	0.799 ± 0.061	-1.96 ± 1.78	-0.15 ± 0.13
9.00	0.0574 ± 0.001	0.295 ± 0.015	0.00128 ± 0.0001	0.903 ± 0.025	-27.6 ± 3.1	-1.88 ± 0.27

Table 6.11: Calculation of $\Delta\sigma_L$. All asymmetries are $\times 10^{-4}$.

E_n (MeV)	$\bar{\epsilon}_n \pm \sigma_{\bar{\epsilon}_n}$	P_n	P_d	$x_d(b^{-1})$	$(\Delta\sigma_L)_C$ (mb)	$(\Delta\sigma_L)_d$ (mb)
5.00	-20.7 ± 0.57	0.404 ± 0.144	0.302 ± 0.016	0.0574 ± 0.001	6.3 ± 0.9	-597 ± 219
6.88	-13.0 ± 0.33	0.464 ± 0.027	0.260 ± 0.014	0.0574 ± 0.001	-0.14 ± 0.12	-375 ± 32
6.88	-9.22 ± 0.36	0.464 ± 0.027	0.220 ± 0.014	0.0574 ± 0.001	-0.15 ± 0.13	-315 ± 30
9.00	-6.87 ± 0.41	0.521 ± 0.022	0.295 ± 0.015	0.0574 ± 0.001	-1.88 ± 0.27	-154 ± 14

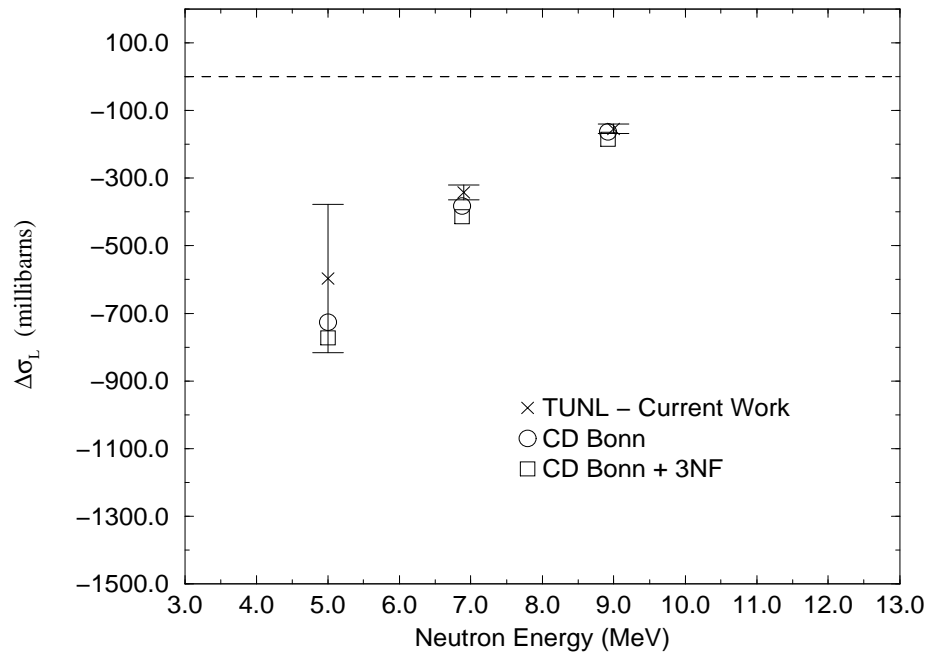


Figure 6.6: Plot of $\Delta\sigma_L$ vs. E_n . The CD-Bonn and CD-Bonn + TM 3NF predictions are also included for comparison. The 6.88 MeV value is the weighted average of the two values found in Table 6.11.

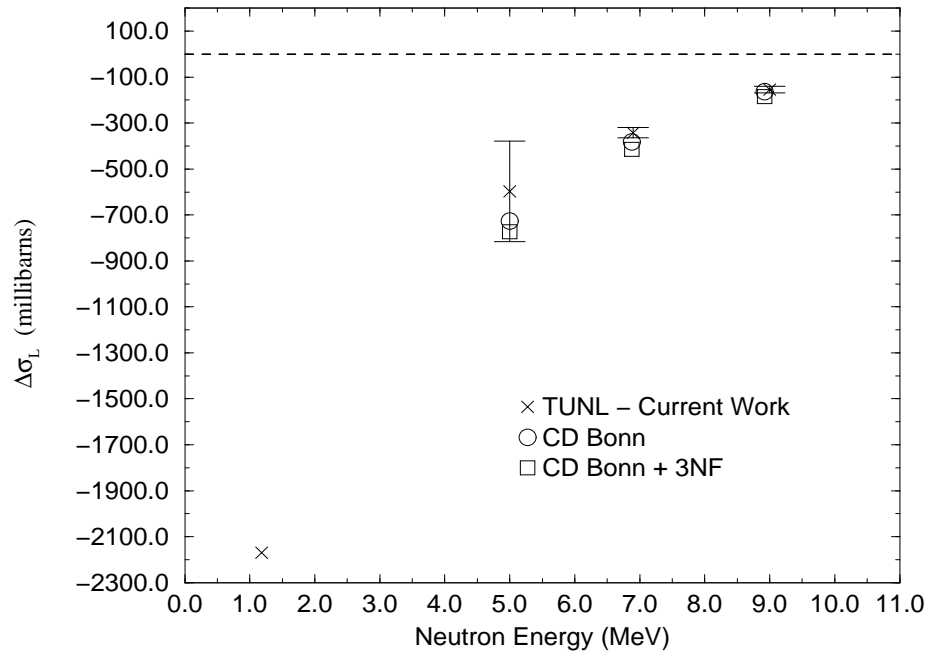


Figure 6.7: Plot of $\Delta\sigma_L$ vs. E_n . The CD-Bonn and CD-Bonn + TM 3NF predictions are also included for comparison. The 6.88 MeV value is the weighted average of the two values found in Table 6.11. This plot includes the 1.18 MeV point that was used for the NMR calibration.

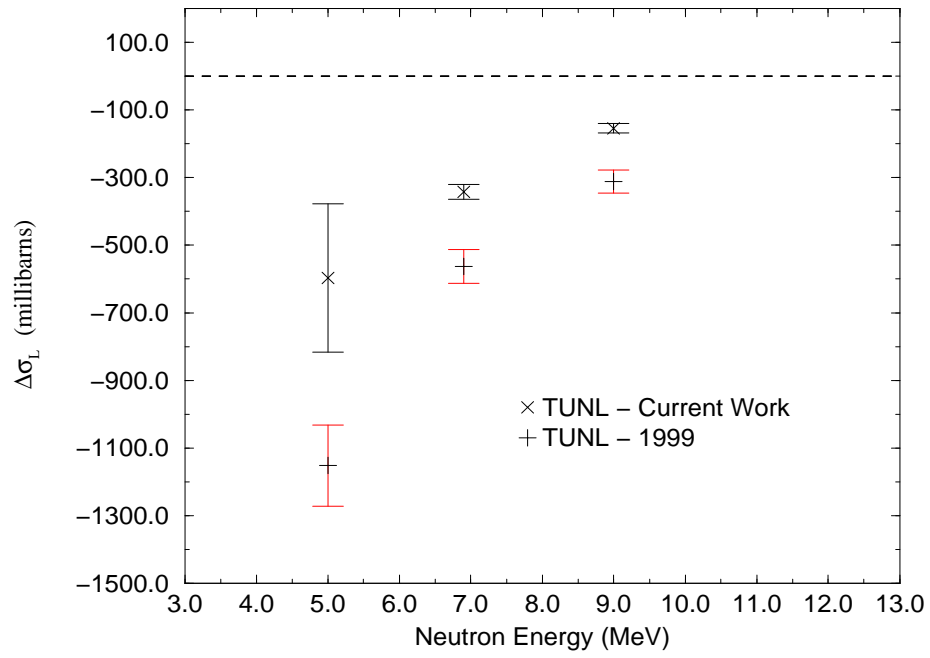


Figure 6.8: Plot of $\Delta\sigma_L$ vs. E_n . This plot is a comparison of the current work with the data from [Mar99].

Chapter 7

Summary and Discussion

The longitudinal spin-dependent total cross section difference, $\Delta\sigma_L$, has been measured for $\vec{n} - \vec{d}$ scattering at neutron energies of 5.0, 6.88, and 9.0 MeV using a dynamically polarized deuteron target. Neutron transmission asymmetries were measured for neutron energy of 1.18 MeV for the purpose of calibrating the NMR target polarization measurement. The existing ^3He evaporation refrigerator was converted to a ^3He - ^4He dilution refrigerator to achieve lower target temperatures producing higher target polarizations. The dilution refrigerator cooled the target to 250 mK and a superconducting magnet provided a 2.5 T magnetic field. Dynamic nuclear polarization was achieved with 69 GHz microwaves. The target material used was fully deuterated 1,2-propanediol frozen into 1 mm diameter beads. Target polarization was determined by nuclear magnetic resonance.

Charged particle beams were produced by the Atomic Beam Polarized Ion Source and accelerated by the TUNL Van de Graaff electrostatic accelerator. The polarized neutron beam was produced via the $^3\text{H}(\vec{p}, \vec{n})^3\text{He}$ or $^2\text{H}(\vec{d}, \vec{n})^3\text{He}$ reaction. Neutron beam polarization was determined either by measuring the proton beam polarization and calculating the neutron polarization or by measuring the neutron beam polarization directly.

Neutrons that passed through the polarized target were detected at 0° with a scintillation detector coupled to a photomultiplier tube. A neutron transmission asymmetry was measured for transmitted spin-up and spin-down neutrons and was used to calculate

$\Delta\sigma_L$.

Excluding the 5.0 MeV value, the data have a precision of 12%, a significant improvement over the previous measurement [Mar02]. We show that there are no large discrepancies with theory such as those seen in the A_y puzzle. However, the results are not precise enough to discern the presence or absence of 3NF effects.

We found no significant factors that would explain the disagreement between these data and those of [Mar02]. However, our figure of merit $(P_T x)^2$ is much larger than in the previous experiment. We also have benchmarked our higher energy measurements to the 1.18 MeV $\Delta\sigma_L$ and we rechecked various factors such as target position. We therefore believe that the present results are the more definitive.

Appendix A

Nucleon-Nucleon Potential Models

In the last few decades, quantum chromodynamics (QCD) has replaced meson-exchange theory as the fundamental theory of the nuclear strong force. However, QCD is not yet a practical method for solving problems as complicated as few body nuclear systems. There are two main reasons why nuclear phenomena cannot be calculated as a many-body problem involving the interactions of quarks and gluons. First, perturbative methods cannot be used because of the large coupling constant for the strong interaction ($\alpha_S \gtrsim 1$). Second, gluons can interact with each other, creating a much more complex calculation and today's computational capabilities are not powerful enough to solve a system with so many degrees of freedom. Therefore, meson-exchange theory is still very useful as an effective description of the nuclear strong force at low energies. The best theoretical predictions of experimental nuclear physics observables come from effective potential models that are based on meson exchange.

First, some necessary features of the nuclear force model will be discussed. All models that attempt to describe the NN interaction must account for the following properties [Mac89]:

1. Finite or short range - The Coulomb force is all that is needed to explain interactions among nuclei in molecules, so the upper limit of the nuclear force range must be

on the order of the interatomic distances. However, a lower, more precise limit can be found by studying the saturation properties of nuclei. Electron scattering shows that the nuclear density is roughly constant with the radius of heavy nuclei being proportional to $A^{1/3}$. Each nucleon seems to only attract its nearest neighbors. Also, it has been found that the binding energy per nucleon is constant for $A > 4$. It has been concluded that the range of the nuclear force is roughly 1.7 fm.

2. Attractive at intermediate distances - The total range of the nuclear force is divided into three parts: short-, intermediate-, and long-range. Without the attractive intermediate part, nuclear binding would not occur because the Coulomb repulsion from the protons would tear the nucleus apart. Also, for energies below 300 MeV, the phase shifts for NN scattering are positive, indicating an attractive potential.
3. A repulsive core - A qualitative argument for a repulsive core can be made based on the constant nuclear density; adding more nucleons does not increase the nuclear density, so something keeps the nucleons from getting too close together. Quantitatively, at higher scattering energies smaller distance scales are probed and the phase shifts are negative, which indicates a repulsive potential. Data from [Mac69] show that the phase shift for neutron - proton scattering changes sign around 300 MeV. Calculations show that the radius of this repulsive core is approximately 0.5 fm.
4. A tensor part - The observed quadrupole moment for the ground state of the deuteron is evidence for a tensor component of the nuclear force. If the deuteron was purely an s-state ($l = 0$) and spherically symmetric, then the quadrupole moment would vanish. A noncentral potential is required to mix the s- and d-states of the deuteron in order to produce the nonzero quadrupole moment and to accurately calculate the magnetic moment of the deuteron.
5. A spin-orbit part - A spin-orbit term must be added to the central and tensor nuclear force components in order to reproduce the triplet p-waves from phase shift analyses at high energies.

The exchange force model has been shown to be very adequate in describing the NN interaction and meets all of the previously listed criteria. The mediation of the nuclear force via massive particle exchange was first proposed by Yukawa in 1935 and the theoretical framework was put in place by Taketani, Nakamura, and Sasaki (TNS) in 1951 after the discovery of the pion in 1947/48. TNS developed the concept of the long-range ($r \gtrsim 2$ fm), intermediate-range ($1 \text{ fm} \lesssim r \lesssim 2 \text{ fm}$), and short-range ($r \lesssim 2 \text{ fm}$) parts of the nuclear force with the range being tied to the mass of the exchanged particle. One-pion exchange dominates the long-range interaction and two-pion exchange takes over in the intermediate range, though heavier mesons such as ω play a role. For the short-range region, there are many different processes that contribute, including multi-pion exchange, heavy mesons, and from QCD, quark-gluon exchange.

Yukawa followed the example of quantum electrodynamics (QED) in that he carried out his work in the framework of classical field theory. In QED, the electromagnetic interaction is carried by a field of massless particles known as photons, which satisfy a field equation known as the Poisson equation. In the static approximation,

$$-\nabla^2 V(\mathbf{r}) = e\delta^{(3)}(\mathbf{r}) \quad (\text{A.1})$$

with the solution being the well-known Coulomb potential

$$V(r) = \frac{e}{4\pi} \frac{1}{r}. \quad (\text{A.2})$$

Similarly, in meson-exchange theory, a field of particles with *nonzero* mass m must satisfy the Klein-Gordon equation

$$(\square + m^2)\varphi(x) = g\bar{\psi}(x)\psi(x) \quad (\text{A.3})$$

where \hbar and c have been set to 1 for simplicity and \square is the d'Alembertian operator

$$\square = \frac{1}{c^2} \frac{\partial^2}{\partial t^2} - \nabla^2. \quad (\text{A.4})$$

Assuming the source of the meson field (the nucleon, represented by $\psi(x)$) is infinitely heavy and fixed at the origin, we obtain

$$(-\nabla^2 + m^2)\varphi(\mathbf{r}) = \mathbf{g}\delta^{(3)}(\mathbf{r}) \quad (\text{A.5})$$

with the solution

$$\varphi(r) = \frac{g}{4\pi} \frac{e^{-mr}}{r} \quad (\text{A.6})$$

which is the Yukawa potential. The exponential factor gives the correct finite range and it reduces to the Coulomb potential for a massless particle.

The most important mesons, in terms of the nuclear force, are the π , ρ , and ω mesons. The pion is the lightest meson and provides the long-range part of the nuclear force and because of its pseudoscalar nature, the tensor part. The ρ meson reduces the tensor interaction at short range and the ω meson provides the spin-orbit component and the short-range repulsion. These three mesons describe all of the properties of the NN interaction listed earlier, except for the intermediate-range attraction. This attraction could be explained theoretically by a scalar-isoscalar boson with a mass of 500 - 700 MeV, but experiments have failed to produce any evidence for this particle. The intermediate attraction is instead understood as a 2π -exchange process. Because of the simplicity of a potential based solely on one boson exchange (OBE), theorists have used a fictitious scalar boson known as the σ meson to reproduce the effects of multiple-meson exchange by adjusting its mass and coupling constant to fit the NN experimental data.

Realistic NN calculations should be able to accurately fit pp and np scattering data and reproduce the properties of the deuteron. The four NN interactions that are considered in the present work are the same ones used in [Wit99] and produce an excellent fit to pp and np scattering data below 350 MeV. Each potential model will be briefly discussed and some important properties of the potentials are summarized in Table A.1. All of these NN potentials can be put into the general form

$$v(NN) = v^{EM}(NN) + v^{\pi}(NN) + v^R(NN) \quad (\text{A.7})$$

where $v^R(NN)$ is the intermediate- and short-range part of the interaction and includes some number of parameters (N_{param} in Table A.1) which are determined by a fitting procedure to NN scattering data and the deuteron binding energy. $v^{\pi}(NN)$, the one-pion-exchange (OPE) potential, and $v^{EM}(NN)$, the electromagnetic part, represent the long-

range part of the potentials. These potentials have been fit to the np and pp data sets below 350 MeV from the 1992 NN database.

The Argonne v_{18} (AV18) [Wir95] potential was fitted to pp and np data, as well as low-energy nn scattering parameters and deuteron properties. The EM part of AV18 includes one- and two-photon Coulomb terms, the Darwin-Foldy term, vacuum polarization, and the magnetic moment interaction, each with appropriate form factors. The intermediate- and short-range part of the potential is written as the sum of central, L^2 , tensor, spin-orbit, and quadratic spin-orbit terms which all use the *average* pion mass. The charge-dependent structure of the OPE potential is given by

$$\begin{aligned} v^\pi(pp) &= f_{pp}^2 v_\pi(m_\pi^0), \\ v^\pi(np) &= f_{pp} f_{nn} v_\pi(m_\pi^0) + (-)^{T+1} 2f_c^2 v_\pi(m_\pi^\pm), \\ v^\pi(nn) &= f_{nn}^2 v_\pi(m_\pi^0), \end{aligned} \quad (\text{A.8})$$

where T is the isospin and

$$v_\pi(m) = \left(\frac{m}{m_s}\right)^2 \frac{1}{3} mc^2 [Y_\mu(r) \sigma_i \cdot \sigma_j + T_\mu(r) S_{ij}] \quad (\text{A.9})$$

where the scaling mass, m_s , is introduced to make the coupling constant dimensionless and is equal to the charged-pion mass, m_{π^\pm} . $Y_\mu(r)$ and $T_\mu(r)$ are the Yukawa and tensor functions

$$Y_\mu(r) = \frac{e^{-\mu r}}{\mu r} (1 - e^{-cr^2}), \quad (\text{A.10})$$

$$T_\mu(r) = \left(1 + \frac{3}{\mu r} + \frac{3}{(\mu r)^2}\right) \frac{e^{-\mu r}}{\mu r} (1 - e^{-cr^2})^2 \quad (\text{A.11})$$

where $\mu = mc/\hbar$. Partial-wave analysis of NN scattering data below 350 MeV done at Nijmegen finds very little difference between the coupling constants [Sto93], so they are chosen to be charge independent so that $f_{pp} = -f_{nn} = f_c = f$, with $f^2 = 0.075$. The result is that all charge dependence in Equation A.8 is due to the charged- and neutral-pion mass differences.

The CD-Bonn potential [Mac01] is constructed from three NN interactions, a proton-proton (pp), a neutron-proton (np), and a neutron-neutron (nn) potential, making it charge-dependent (thus, the CD in CD-Bonn). This makes it very useful for studying charge-symmetry breaking (CSB) and charge-independence breaking (CIB). This potential adjusts two fictitious σ bosons individually for each partial wave. The most realistic meson model for the nuclear force includes all important meson exchanges so that the σ -boson stands for the sum of all higher order meson exchanges, not just 2π -exchange. A distinctive feature of this model is its “off the energy shell” (off-shell) behavior. “On the energy shell” processes are those in which the total energy of the two nucleons is conserved such as in free-space NN scattering. For $A > 2$ systems, the total energy of the system is conserved, but the energy is not necessarily conserved in a particular interaction between two nucleons in the nucleus. The two nucleons may have different energies before and after the interaction. When the nuclear binding energy is calculated for $A > 2$ systems, off-shell processes must be included. However, these cannot be tested by experiments; only theory can provide this information. One result from including off-shell processes is that the calculated triton binding energy is increased and is closer to its experimental value.

The Nijmegen potentials [Sto94] explicitly distinguish between neutral- and charged-pion masses. This means that the isovector np and pp OPE potentials are different and charge independence is broken. However, the model assumes that the pion-nucleus coupling constants obey charge independence. The Nijm92pp potential is used as the basis for the construction of Nijm I and Nijm II. By adjusting separately a few parameters in each partial wave, a very high-quality potential model is formed. The Nijm I potential contains momentum-dependent terms, which in configuration space produce a nonlocal structure. Nijm II omits these momentum-dependent terms and is thus a purely local potential. In a sense, these potentials are alternative partial-wave analyses.

As can be seen in Table A.1, the NN potential models fall short of predicting the correct triton binding energy of 8.48 MeV. By adding three-nucleon forces (3NF) to the NN interaction models, the correct triton binding energy can be calculated. Appendix B

Table A.1: Summary of properties and predictions of NN interaction models.

NN Potential Model	Character	N_{param}	$\chi^2/datum$	E_t (MeV)
AV18	Local	40	1.09	7.576
CD Bonn	Nonlocal	43	1.03	8.00
Nijmegen I	Nonlocal	41	1.03	7.731
Nijmegen II	Local	47	1.03	7.709

describes the two-pion-exchange three-nucleon force.

Appendix B

The Two-Pion-Exchange Three-Nucleon Force

A three-body force is defined as a force that depends in an irreducible way on the simultaneous coordinates, momenta, spins, and internal quantum numbers of the three interacting particles. Since the OPE described the long-range part of the NN interaction so well, it was only natural that the 3NF was first constructed as a 2π -exchange force. Two-pion exchange, as illustrated in Figure B.1, was first proposed by Fujita and Miyazawa [Fuj57] and consisted of the exchange of two pions with an intermediate Δ -isobar. In the figure, only the part of the 3NF for which nucleon 1 is the middle nucleon (i. e., the nucleon at which the virtual pion scattering takes place) is shown. This configuration is called $V_4^{(1)}$, with V_{1-3} being the three parts of the NN potential shown in Equation A.7. The complete 3NF is given by

$$V_4 = V_4^{(1)} + V_4^{(2)} + V_4^{(3)}. \quad (\text{B.1})$$

The most widely used 3NF, the Tucson-Melbourne (TM) model [Coo79], treats off-shell effects in a detailed manner. The various parameters of this model incorporate phenomenology in a more meaningful way than the Fujita-Miyazawa model. The pions are

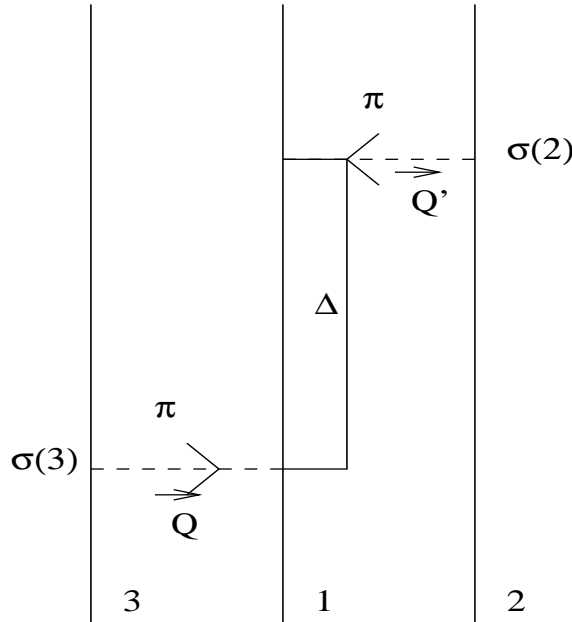


Figure B.1: The two-pion-exchange 3NF force with a Δ isobar.

off-mass-shell while the nucleons are on their mass shells and all three nucleons are allowed to move freely. In the two decades since the TM model was published, several other 3NF models have appeared, including the Urbana-Argonne [Car83], the RuhrPot [Ede96], the Brazil [Coe83], and the Texas [Ord92] models. It should be noted that the Urbana-Argonne model is based on Δ -isobars, the Brazil and RuhrPot models are based on relativistic field theories, and the Texas model is based on chiral perturbation theory. Only the TM 3NF model is discussed in this work.

Early 3NF models based only on 2π -exchange overbound the triton by 1.5 MeV [Che86]. A more recent version of the TM 3NF [Coo93] has included ρ -meson exchange because the ρ interactions provide a repulsive contribution to the binding energy, cancelling out some of the 2π attraction. However, it was shown that the triton binding energy could be correctly predicted, even without the ρ -exchange, by combining the 3NF with the NN potential models and properly adjusting the cutoff parameter Λ . Each NN potential model then requires a different value for the cutoff parameter to correctly predict the triton binding energy. Λ acts as a strength factor in the TM 3NF so that the three-nucleon binding energy

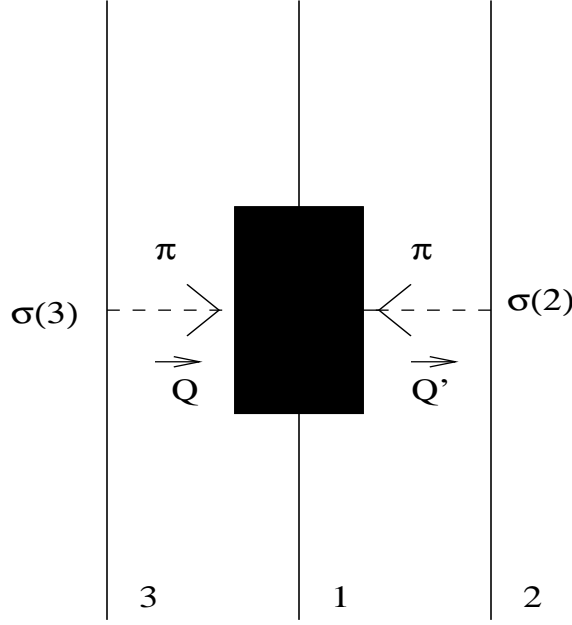


Figure B.2: General two-pion-exchange three-nucleon force. The dark rectangle represents any contribution except a forward-propagating nucleon state.

is very sensitive to it. For example, a variation in Λ of one pion mass causes differences in the 3N binding energy of 1.5 MeV [Nog97].

Once the case for a 3NF has been made, one must consider the mechanism that is responsible for this force. The situation in Figure B.1 is not the most general process for 2π -exchange. The myriad of ways to accomplish this interaction is indicated by the dark rectangle in Figure B.2. The TM 3NF is based on a low momentum expansion of the π -nucleon off-mass-shell scattering amplitude and has the form

$$\begin{aligned}
 V_4^{(1)} &= \frac{1}{(2\pi)^6} \frac{g_{\pi NN}^2}{4m_N^2} \left(\frac{\vec{\sigma}_2 \cdot \vec{Q}}{\vec{Q}^2 + m_\pi^2} \right) \left(\frac{\vec{\sigma}_3 \cdot \vec{Q}'}{\vec{Q}'^2 + m_\pi^2} \right) F(\vec{Q}^2) F(\vec{Q}'^2) \\
 &\times \{ \vec{\tau}_2 \cdot \vec{\tau}_3 [a + b\vec{Q} \cdot \vec{Q}' + c(\vec{Q}^2 + \vec{Q}'^2)] \\
 &+ di\vec{\tau}_3 \times \vec{\tau}_2 \cdot \vec{\tau}_1 \vec{\sigma}_1 \cdot \vec{Q} \times \vec{Q}' \}. \tag{B.2}
 \end{aligned}$$

Here, \vec{Q} and \vec{Q}' are the pion momenta and $\vec{\tau}_i$ are the nucleon isospins. $a = 1.13/m_\pi$, $b = -2.58/m_\pi^3$, $c = 1.0/m_\pi^3$, and $d = -0.753/m_\pi^3$ are strength parameters and are fixed by theory. They incorporate the physics resulting from, among other things, an intermediate

Table B.1: The cutoff parameter Λ used in the given potential combinations.

NN Potential Model	Λ
AV18 + TM	5.215
CD Bonn + TM	4.856
Nijmegen I + TM	5.120
Nijmegen II + TM	5.072

Δ . The π NN $F(\vec{Q}^2)$ form factors have the form

$$F(\vec{Q}^2) = \left(\frac{\Lambda^2 - m_\pi^2}{\Lambda^2 + \vec{Q}^2} \right) \quad (\text{B.3})$$

where Λ is the adjustable cut-off parameter used to calculate the correct triton binding energy in conjunction with the various NN force models. Values for Λ for each NN interaction are found in Table B.1.

Appendix C

Proton Polarimetry Test

These measurements were taken with the proton beam polarization axis in the longitudinal orientation. I_B and B are the Wien filter current and magnetic field, respectively. The detectors were at 75° and the analyzing power was 0.721 ± 0.007 . These data were taken to confirm the Wien filter settings for the longitudinal orientation. These measurements should be compared to those in Table 6.1, which were taken with $I_B = 16.11$ A and $B = 217$ G. The result indicates that the longitudinally polarized beam was polarized slightly off axis.

Table C.1: Proton-beam polarization measurements taken in the longitudinal orientation during the $E_n = 1.18$ MeV experimental run in December 2003.

E_p (MeV)	Run #	ϵ_p	I_B (A)	B (G)	P_p
2.52	7309	0.021 ± 0.003	46.57	-633.0	0.029 ± 0.004
2.52	7310	0.029 ± 0.003	46.57	-633.0	0.040 ± 0.004
2.52	7311	0.029 ± 0.013	47.96	-652.5	0.041 ± 0.018
2.52	7312	0.011 ± 0.005	47.96	-652.5	0.015 ± 0.006

Appendix D

The program npinit.com

```
$ ! npinit.com
$ !   initialization program for delta sigma l data acquisition
$ !
$ !   lifted from wsw
$ !   modified 5/7/96 by BWR and JRW to accomodate time of flight gating
$ !   of neutrons, new code rtof.evl, .dap
$ !   modified 12/8/95 DSJ, JRW, BEC for KE 3610 scalers instead of Phillips
$ !   1/96 restored filenames to original: removed *2.*
$ !
$ !!!!!!!!!!!!!!!!!!!!!!!!!!!!!!!!!!!!!!!!!!!!!!!!!!!!!!!!!!!!!!!!!!!!!
$ !
$ !   REQUIRED PROGRAMS:
$ ! CLEAR.COM      ! crate initialization
$ ! BOXUSR.FOR     ! user defined box
$ ! BOXSET.COM     ! initializes box
$ ! FLAGON.COM
$ ! FLAGOFF.COM
$ ! ?????VOLTREAD.FOR ! gets last data and sum of spectrum
$ !
$ ! NEUTRON SUBPROCESS
$ ! ROUT.EVL      ! sorting for neutrons
$ ! ROUT.DAP      ! subprocess for neutrons
$ ! NEUTDUMP.COM  ! dump file for neutrons
$ ! NEUTASYM.FOR ! calcs neutron asymmetries in npdump
$ !
$ ! POLARIMETER SUBPROCESS
$ ! DPOL.EVL      ! sorting for deuterons
$ ! DPOL.DAP      ! subprocess for deuterons
$ ! DPOLDUMP.COM  ! dump file for deuterons
```

```

$ ! DPOLASYM.FOR ! calcs deuteron polarizations in npdump
$ !
$ ! COUNTDOWN SUBPROCESS
$ ! PSCL.DAP ! subprocess for countdown scaler
$ !
$ !!!!!!!!!!!!!!!!!!!!!!!!!!!!!!!!!!!!!!!!!!!!!!!!!!!!!!!!!!!!!!!!!!!!!!!!!!!!!
$ !
$ ! PUT 1 ! download GDAP into the MBD
$ !
$ INQUIRE JUMP "Define spectra and gates?"
$ IF JUMP .EQS. "N" THEN GOTO THERE
$ !!!!!!!!!!!!!!!!!!!!!!!!!!!!!!!!!!!!!!!!!!!!!!!!!!!!!!!!!!!!!!!!!!!!!!!!!!!!!
$ ! allocate spectra !
$ !!!!!!!!!!!!!!!!!!!!!!!!!!!!!!!!!!!!!!!!!!!!!!!!!!!!!!!!!!!!!!!!!!!!!!!!!!!!!
$ !
$ DMEM ALL
$ !
$ ! spectra for NEUTRONS
$ !
$ AMEM 11 1024 I*4 1D LINK_UP ! main det LINK neutrons up
$ AMEM 12 1024 I*4 1D GAMMA_UP ! main det gammas up
$ AMEM 13 1024 I*4 1D CANB_UP ! main det CANBERRA neutrons up
$ AMEM 14 1024 I*4 1D GA_PUL_UP ! main detector DTC up
$ AMEM 21 1024 I*4 1D NEUT_DN ! main det LINK neutrons down
$ AMEM 22 1024 I*4 1D GAMMA_DN ! main det gammas down
$ AMEM 23 1024 I*4 1D CANB_DN ! main det CANBERRA neutrons down
$ AMEM 24 1024 I*4 1D GA_PUL_DN ! main detector DTC down
$ AMEM 31 1024 I*4 1D MON_UP ! monitor det up
$ AMEM 32 1024 I*4 1D MON_DN ! monitor det dn
$ AMEM 51 1024 I*4 1D F_PUL_UP ! 50 MHz pulser up
$ AMEM 52 1024 I*4 1D F_PUL_DN ! 50 MHz pulser down
$ AMEM 53 1024 I*4 1D S_PUL_UP ! 100 kHz pulser up
$ AMEM 54 1024 I*4 1D S_PUL_DN ! 100 kHz pulser down
$ AMEM 61 1024 I*4 1D BCI_UP ! BCI up
$ AMEM 62 1024 I*4 1D BCI_DN ! BCI down
$ AMEM 71 1024 I*4 1D SPIN_UP ! spin up's per 8 step sequence
$ AMEM 72 1024 I*4 1D SPIN_DN ! spin dn's per 8 step sequence
$ AMEM 91 1024 I*4 1D EXTRA1 ! Extra area if needed
$ AMEM 92 1024 I*4 1D EXTRA2 ! Extra area if needed
$ AMEM 93 1024 I*4 1D EXTRA3 ! Extra area if needed
$ AMEM 94 1024 I*4 1D EXTRA4 ! Extra area if needed
$ AMEM 95 1024 I*4 1D EXTRA5 ! Extra area if needed
$ AMEM 100 1024 I*4 1D DTC-DEF ! XSYS Areas
$ AMEM 101 1024 I*4 1D SCALERS ! XSYS Areas
$ !

```

```

$ ! spectra for DPOL
$ !
$     AMEM 201 1024 I*4 1D ZERO_UP
$     AMEM 202 1024 I*4 1D ZERO_DN
$     AMEM 211 1024 I*4 1D LEFT_UP
$     AMEM 212 1024 I*4 1D LEFT_DN
$     AMEM 221 1024 I*4 1D RIGHT_UP
$     AMEM 222 1024 I*4 1D RIGHT_DN
$     AMEM 251 1024 I*4 1D SPN_ROUT
$ !
$ !!!!!!!!!!!!!!!!!!!!!!!!!!!!!!!!!!!!!!!!!!!!!!!
$ !       allocate gates           !
$ !!!!!!!!!!!!!!!!!!!!!!!!!!!!!!!!!!!!!!!!!!!!!!!
$ !
$     GATE NEW                      ! remove all old gates
$     GATE 11                      ! main det up n gate
$     GATE 12 1 11                 ! main det up g gate
$     GATE 13 1 11                 ! main det up n gate
$     GATE 14 1 11                 ! main det up DTC gate
$     GATE 21 1 11                 ! main det dn n gate
$     GATE 22 1 11                 ! main det dn g gate
$     GATE 23 1 11                 ! main det dn n gate
$     GATE 24 1 11                 ! main det dn DTC gate
$     GATE 31 1 11                 ! monitor det up gate
$     GATE 32 1 11                 ! monitor det down gate
$     GATE 51 1 11                 ! fast pulser up gate
$     GATE 52 1 11                 ! fast pulser down gate
$     GATE 53 1 11                 ! slow pulser up gate
$     GATE 54 1 11                 ! slow pulser down gate
$     GATE 61 1 11                 ! BCI up gate
$     GATE 62 1 11                 ! BCI down gate
$     GATE 71 1 11                 ! spin up gate
$     GATE 72 1 11                 ! spin down gate
$ !
$     GATE 201 1                    ! dpol zero deg up gate
$     GATE 202 1 201                ! dpol zero deg down gate
$     GATE 211 1                    ! dpol left up gate
$     GATE 212 1 211                ! dpol left down gate
$     GATE 221 1                    ! dpol right up gate
$     GATE 222 1 221                ! dpol right down gate
$ !
$     GATE SET 11 1 2 1023
$     GATE SET 201 1 2 1023
$ !
$ !!!!!!!!!!!!!!!!!!!!!!!!!!!!!!!!!!!!!!!!!!!!!!!

```

```

$ !
$ there:
$ !
$ !!!!!!!!!!!!!!!!!!!!!!!!!!!!!!!!!!!!!!!!!!!!!!!
$ !   set up countdown scaler      !
$ !!!!!!!!!!!!!!!!!!!!!!!!!!!!!!!!!!!!!!!!!!!!!!!
$ !
$     SCAL NEW ! Clear scalar def.
$     SCAL HEAD 1 REGISTER ! Assign header for register
$     SCAL BOX 1 2 ! Put in box 2
$     SCAL NUMB 1 16 1 REGISTER ! CNA address for register
$ !
$ !!!!!!!!!!!!!!!!!!!!!!!!!!!!!!!!!!!!!!!!!!!!!!!
$ !   set up subprocesses        !
$ !!!!!!!!!!!!!!!!!!!!!!!!!!!!!!!!!!!!!!!!!!!!!!!
$ !
$ !   ROUT subprocess handles reading detector scalers from
$ !           KE 3610 scalers, BiRa count up register, BiRa 6712, and Borer 1241
$ !   DPOL subprocess handles reading charged particle polarimeter spectra
$ !           from Norther ADC
$ !   PSCL subprocess handles preset scaler countdown
$ !
$ WRITE SYS$OUTPUT "setting up subprocesses"
$     @CLEAR ! slow init to not freeze Phillips 7132
$     EVOP SE DPOL ! Subprocess using DPOL.EVL & .DAP
$     EVOP SE ROUT ! Subprocess using ROUT.EVL & .DAP
$     SCAL SE PSCL ! Scaler subprocess using PSCL.DAP
$ !
$ !!!!!!!!!!!!!!!!!!!!!!!!!!!!!!!!!!!!!!!!!!!!!!!
$ !   define commands            !
$ !!!!!!!!!!!!!!!!!!!!!!!!!!!!!!!!!!!!!!!!!!!!!!!
$ !
$ GO      :== @GO.COM
$ DPOL    :== @DPOL.COM
$ PPOL    :== @PPOL.COM
$ XSYSDAT :== "DUA0:[ONLINE1]"
$ XLINK   :== "@XSYSDIR:LINK"
$ FLAGON  :== "$ XSYSDAT:FLAGON"
$ FLAGOFF :== "$ XSYSDAT:FLAGOFF"
$ !
$ !!!!!!!!!!!!!!!!!!!!!!!!!!!!!!!!!!!!!!!!!!!!!!!
$ !   general set up            !
$ !!!!!!!!!!!!!!!!!!!!!!!!!!!!!!!!!!!!!!!!!!!!!!!
$ !
$ CL ALL ! clears all data areas

```

```

$ SCLBUFF CLEAR ALL ! clears all scalar buffers
$ CL FLAGS ! clears flags
$      LMEM ! lists data areas
$      GATE LIST ! lists gate assignments
$      SCAL LIST ! lists scalar definitions
$      INQUIRE/GLOBAL RUN "Initial run number?"
$ RN 'RUN'
$      INQUIRE/GLOBAL ENGY "Neutron energy at center of gas cell?"
$ !
$ !!!!!!!!!!!!!!!!!!!!!!!!!!!!!!!!!!!!!!!!!!!!!!!
$ !  compile,link, and run box  !
$ !!!!!!!!!!!!!!!!!!!!!!!!!!!!!!!!!!!!!!!!!!!!!!!
$ !
$ INQUIRE JUMP "Link subroutines?"
$ IF JUMP .EQS. "N" THEN GOTO THERE2
$ !
$ WRITE SYS$OUTPUT "compiling BOXUSR"
$ FORTRAN BOXUSR
$ WRITE SYS$OUTPUT "compiling NEUTASYM"
$ FORTRAN NEUTASYM
$ WRITE SYS$OUTPUT "compiling DPOLASYM"
$ FORTRAN DPOLASYM
$ WRITE SYS$OUTPUT "compiling FLAGON"
$ FORTRAN FLAGON
$ WRITE SYS$OUTPUT "compiling FLAGOFF"
$ FORTRAN FLAGOFF
$ WRITE SYS$OUTPUT "linking NEUTASYM"
$ XLINK NEUTASYM
$ WRITE SYS$OUTPUT "linking DPOLASYM"
$ XLINK DPOLASYM
$ WRITE SYS$OUTPUT "linking FLAGON"
$ XLINK FLAGON
$ WRITE SYS$OUTPUT "linking FLAGOFF"
$ XLINK FLAGOFF
$ WRITE SYS$OUTPUT "linking BOXUSR"
$ BOXLINK
$ DELETE *.OBJ;*
$ PURGE *.EXE
$ there2:
$ WRITE SYS$OUTPUT "running BOXSET"
$ @BOXSET                ! get box subprocess running
$ BOX I 1 X_RUN
$ BOX R 12 'ENGY'
$ !
$ SHOW TIME

```

```
$ WRITE SYS$OUTPUT " "  
$ WRITE SYS$OUTPUT "NPINIT successfully completed"  
$ BOX M 4 NPINIT successfully completed
```

Appendix E

The program go.com

```
$ ! go.com
$ !
$ ! This command file is used to begin taking neutron data
$ !
$ ! modified 12/8/95 by DSJ, BEC to use KE 3610 scalars instead of the
$ ! problematic Phillips 7132 - see also rout2.dap/evl, pcvx2.dap/evl,
$ ! and substart2.com
$ ! 12/9/95 bwr modify neutdump.com: doesn't clear scaler, should work now
$ ! 1/96 restore filenames to original: get rid of *2.*
$ !
$ CLEAR ALL ! Clear all data areas
$ SCAL CLEAR ALL ! Clear all scalars
$ SCLBUFF CLEAR ALL ! Clear all scalar buffers
$! CNAF 1 11 4 11 ! Clear Phillips scalar
$ CNAF 1 19 0 9 ! Clear 3610 scalars
$ CNAF 1 19 1 9
$ CNAF 1 19 2 9
$ CNAF 1 19 3 9
$ CNAF 1 19 4 9
$ CNAF 1 19 5 9
$ CNAF 1 20 0 9 ! Clear 3610 scalars
$ CNAF 1 20 1 9
$ CNAF 1 20 2 9
$ CNAF 1 20 3 9
$ CNAF 1 20 4 9
$ CNAF 1 20 5 9
$ OUTPUT 2 14 0 16 2 ! Output bit 2 to RESET Spin State Controller
$ OUTPUT 2 14 1 16 2 !
$ OUTPUT 2 14 0 16 1 ! Output bit 1 to START Spin State Controller
```

```
$ !
$   SCAL PRESET 1024
$ !
$   FLAGON 20      ! a neutron run
$   DELETE DUMPFIL.COM;1
$   COPY NEUTDUMP.COM DUMPFIL.COM;1 ! mod original dump: doesn't cl scaler
$   ST NEW                ! Start new run
$   SHOW TIME            !
$   TIMESS = F$TIME()
$   BOX M 4 Run started 'TIMESS'
$   BOX M 1
$   BOX M 2
$   BOX M 3
$   BOX M 6
$   BOX M 7
$   BOX M 8
$   BOX M 9
$   BOX M 10
$ !
$ ! set up box for neutron run
$ !
$   BOX L 1 Run #
$   BOX L 2 Register
$   BOX L 3 Main AY
$   BOX L 4 Mon AY
$ !
$   BOX L 5 Neut up
$   BOX L 6 Pulsr up
$   BOX L 7 Canb up
$   BOX L 8 Mon up
$   BOX L 9 BCI up
$   BOX L 10 Mon-BCI
$   BOX L 11 Mon AY
$   BOX L 12 Energy
$ !
$   BOX L 13 Neut dn
$   BOX L 14 Pulsr dn
$   BOX L 15 Canb dn
$   BOX L 16 Mon dn
$   BOX L 17 BCI dn
$   BOX L 18
$   BOX L 19 BCI AY
$   BOX L 20
$ !
$   BOX L 21 NeYld up
```

```
$      BOX L 22 DTC up
$      BOX L 23 MoYld up
$      BOX L 24
$      BOX L 25
$      BOX L 26
$      BOX L 27 Canb AY
$      BOX L 28 n-m AY
$ !
$      BOX L 29 NeYld dn
$      BOX L 30 DTC dn
$      BOX L 31 MoYld dn
$      BOX L 32
$      BOX L 33 SPuls AY
$      BOX L 34 FPuls AY
$      BOX L 35 DTC AY
$      BOX L 36
```

Appendix F

The program neutasym.for

```
program neutasym
C
C This program extracts the data from the data areas, sums it
C for the entire run, and calculates the asymmetries and average
C asymmetries (with statistical errors and standard deviations).
C These values are written out to NEUTASYM.TMP, which is read by
C NPDUMP.COM and the results boxed.
C
INCLUDE 'XSYSDIR:XSCOM.FOR/NOLIST'
INCLUDE 'XSYSDIR:XERRDEF.FOR/NOLIST'
C
INTEGER*2 EOF,N
C
C counts
REAL*4 NEUT_UP,NEUT_DN,GAMMA_UP,GAMMA_DN,BOTH_UP,BOTH_DN,GATED_UP,
      >GATED_DN,MON_UP,MON_DN,FPULS_UP,FPULS_DN,SPULS_UP,SPULS_DN,
      >BCI_UP,BCI_DN
C dead time corrections, yields, and yield errors
REAL*4 DTC_UP,DTC_DN,DMON_UP,DMON_DN,NEYLD_UP,NEYLD_DN,GAYLD_UP,
      >GAYLD_DN,BOYLD_UP,BOYLD_DN,DNYLD_UP,DNYLD_DN,DGYLD_UP,
      >DGYLD_DN,DBYLD_UP,DBYLD_DN,moyld_up,moyld_dn,dmyld_up,
      >dmyld_dn
C asymmetries and asymmetry yields
REAL*4 NEUT_AY,DNEUT_AY,GAMM_AY,DGAMM_AY,BOTH_AY,DBOTH_AY,MON_AY,
      >DMON_AY
C averages
REAL*4 NEUTSUM1,NEUTSUM2,NEUTSUM3,GAMMSUM1,GAMMSUM2,GAMMSUM3,
      >BOTHSUM1,BOTHSUM2,BOTHSUM3,MONSUM1,MONSUM2,MONSUM3,
      >MEAN_NEUT_AY,UNCERT_NEUT_AY,STD_NEUT_AY,
```

```

    >MEAN_GAMM_AY,UNCERT_GAMM_AY,STD_GAMM_AY,
    >MEAN_BOTH_AY,UNCERT_BOTH_AY,STD_BOTH_AY,
    >MEAN_MON_AY ,UNCERT_MON_AY ,STD_MON_AY
REAL*4 SCALE
INTEGER*4 RUNNUM
C
CALL PARSE
C
C Use the map command to retrieve arrays. Then get moments.
C
CALL SHORTSUM(11,1,NEUT_UP)
CALL SHORTSUM(12,1,GAMMA_UP)
CALL SHORTSUM(13,1,BOTH_UP)
CALL SHORTSUM(14,1,GATED_UP)
CALL SHORTSUM(21,1,NEUT_DN)
CALL SHORTSUM(22,1,GAMMA_DN)
CALL SHORTSUM(23,1,BOTH_DN)
CALL SHORTSUM(24,1,GATED_DN)
CALL SHORTSUM(31,1,MON_UP)
CALL SHORTSUM(32,1,MON_DN)
CALL SHORTSUM(51,1,FPULS_UP)
CALL SHORTSUM(52,1,FPULS_DN)
CALL SHORTSUM(53,1,SPULS_UP)
CALL SHORTSUM(54,1,SPULS_DN)
CALL SHORTSUM(61,1,BCI_UP)
CALL SHORTSUM(62,1,BCI_DN)
C
C !!!!!!!!!!!!!!!!!!!!!!!!!!!!!!!!!!!!!!!!!!!!!!!
C ! Calculate dead-time corrections !
C !!!!!!!!!!!!!!!!!!!!!!!!!!!!!!!!!!!!!!!!!!!!!!!
C
IF (GATED_UP .NE. 0.0) THEN
DTC_UP=SPULS_UP/GATED_UP
ELSE
DTC_UP=1.0
END IF
C
IF (GATED_DN .NE. 0.0) THEN
DTC_DN=SPULS_DN/GATED_DN
ELSE
DTC_DN=1.0
END IF
C
C !!!!!!!!!!!!!!!!!!!!!!!!!!!!!!!!!!!!!!!!!!!!!!!
C ! Calculate detector yields      !

```

```

C !!!!!!!!!!!!!!!!!!!!!!!!!!!!!!!!!!!!!!!!!!!!!!!
C
C
DMON_UP = SQRT(MON_UP)
C
C
  IF (NEUT_UP .NE. 0.0) THEN
NEYLD_UP=(NEUT_UP/BCI_UP)*DTC_UP
DNYLD_UP=SQRT(1/NEUT_UP+1023*3/(4*BCI_UP**2))*NEYLD_UP
  ELSE
NEYLD_UP=0.0
DNYLD_UP=0.0
  END IF
c
  IF (mon_UP .NE. 0.0) THEN
moYLD_UP=(mon_UP/BCI_UP)
DmYLD_UP=SQRT(1/mon_UP+1023*3/(4*BCI_UP**2))*moYLD_UP
  ELSE
moYLD_UP=0.0
DmYLD_UP=0.0
  END IF
C
c canberra
  IF (both_UP .NE. 0.0) THEN
boYLD_UP=(both_UP/BCI_UP)
DbYLD_UP=SQRT(1/both_UP+1023*3/(4*BCI_UP**2))*boYLD_UP
  ELSE
boYLD_UP=0.0
DbYLD_UP=0.0
  END IF
C
C
DMON_DN = SQRT(MON_DN)
C
C
C Normalize to BCI, spin down
C
  IF (NEUT_DN .NE. 0.0) THEN
NEYLD_DN=(NEUT_DN/BCI_DN)*DTC_DN
DNYLD_DN=SQRT(1/NEUT_DN+1023*3/(4*BCI_DN**2))*NEYLD_DN
  ELSE
NEYLD_DN=0.0
DNYLD_DN=0.0
  END IF
c

```

```

      IF (mon_DN .NE. 0.0) THEN
moYLD_DN=(mon_DN/BCI_DN)
DmYLD_DN=SQRT(1/mon_DN+1023*3/(4*BCI_DN**2))*moYLD_DN
      ELSE
moYLD_DN=0.0
DmYLD_DN=0.0
      END IF
c
c canberra

      IF (both_DN .NE. 0.0) THEN
boYLD_DN=(both_DN/BCI_DN)
DbYLD_DN=SQRT(1/both_DN+1023*3/(4*BCI_DN**2))*boYLD_DN
      ELSE
boYLD_DN=0.0
DbYLD_DN=0.0
      END IF
C
C !!!!!!!!!!!!!!!!!!!!!!!!!!!!!!!!!!!!!!!
C! Calculate asymmetries !
C !!!!!!!!!!!!!!!!!!!!!!!!!!!!!!!!!!!!!!!
C
IF ((NEYLD_UP+NEYLD_DN) .NE. 0.0) THEN
NEUT_AY=(NEYLD_UP-NEYLD_DN)/(NEYLD_UP+NEYLD_DN)
DNEUT_AY=(2.0/(NEYLD_UP+NEYLD_DN)**2)*SQRT((NEYLD_UP*DNYLD_DN)
>**2+(NEYLD_DN*DNYLD_UP)**2)
ELSE
NEUT_AY=0.0
DNEUT_AY=0.0
END IF
c
c canberra
IF ((boYLD_UP+boYLD_DN) .NE. 0.0) THEN
both_AY=(boYLD_UP-boYLD_DN)/(boYLD_UP+boYLD_DN)
Dboth_AY=(2.0/(boYLD_UP+boYLD_DN)**2)*SQRT((boYLD_UP*DbYLD_DN)
>**2+(boYLD_DN*DbYLD_UP)**2)
ELSE
both_AY=0.0
Dboth_AY=0.0
END IF
C
bci_ay=(bci_up-bci_dn)/(bci_up+bci_dn)
c
IF ((Moyld_UP+MOyld_DN) .NE. 0.0) THEN
MON_AY=(MOyld_UP-MOyld_DN)/(MOyld_UP+MOyld_DN)

```

```

DMON_AY=(2.0/(M0yld_UP+M0yld_DN)**2)*SQRT((M0yld_UP*DMyld_DN)
      >**2+(M0yld_DN*DMyld_UP)**2)
ELSE
MON_AY=0.0
DMON_AY=0.0
END IF
C
SCALE = 10000.0
NEUT_AY = NEUT_AY*SCALE
c gamm_ay contains bci ay
GAMM_AY = bci_AY*SCALE
c both_ay contains canb ay
BOTH_AY = BOTH_AY*SCALE
MON_AY = MON_AY*SCALE
C
DNEUT_AY = DNEUT_AY*SCALE
DGAMM_AY = 1.0
DBOTH_AY = DBOTH_AY*SCALE
DMON_AY = DMON_AY*SCALE
C
C !!!!!!!!!!!!!!!!!!!!!!!!!!!!!!!!!!!!!!!!!!!!!!!
C ! append asymmetries to NEUTASYM.LIS !
C !!!!!!!!!!!!!!!!!!!!!!!!!!!!!!!!!!!!!!!!!!!!!!!
C
OPEN(UNIT=2,NAME='NEUTASYM.LIS',ACCESS='APPEND',TYPE='UNKNOWN')
C
WRITE(2,120)X_RUN,NEUT_AY,DNEUT_AY,GAMM_AY,DGAMM_AY,
      >      BOTH_AY,DBOTH_AY,MON_AY,DMON_AY
C
120 FORMAT(X,I5,8(X,F12.6))
C
CLOSE(UNIT=2)
C
C !!!!!!!!!!!!!!!!!!!!!!!!!!!!!!!!!!!!!!!!!!!!!!!
C ! calculate average asymmetries !
C !!!!!!!!!!!!!!!!!!!!!!!!!!!!!!!!!!!!!!!!!!!!!!!
C
N=0
NEUTSUM1=0.0
GAMMSUM1=0.0
BOTHSUM1=0.0
MONSUM1 =0.0
NEUTSUM2=0.0
GAMMSUM2=0.0
BOTHSUM2=0.0

```

```

MONSUM2 =0.0
NEUTSUM3=0.0
GAMMSUM3=0.0
BOTHSUM3=0.0
MONSUM3 =0.0
C
C !!!!!!!!!!!!!!!!!!!!!!!!!!!!!!!!!!!!!!!
C !   first calculate sums           !
C !!!!!!!!!!!!!!!!!!!!!!!!!!!!!!!!!!!!!!!
C
OPEN (UNIT=2,NAME='NEUTASYM.LIS',TYPE='OLD')
C
DO WHILE (EOF .EQ. 0)
READ(2,120,IOSTAT=EOF)RUNNUM,NEUT_AY,DNEUT_AY,GAMM_AY
  >,DGAMM_AY,BOTH_AY,DBOTH_AY,MON_AY,DMON_AY
C
IF (EOF .EQ. 0) THEN
C
N=N+1
C
IF (DNEUT_AY .NE. 0.0) THEN
NEUTSUM1 = NEUTSUM1 + 1/(DNEUT_AY**2)
NEUTSUM2 = NEUTSUM2 + NEUT_AY/(DNEUT_AY**2)
NEUTSUM3 = NEUTSUM3 + (NEUT_AY/DNEUT_AY)**2
END IF
C
IF (DGAMM_AY .NE. 0.0) THEN
GAMMSUM1 = GAMMSUM1 + 1/(DGAMM_AY**2)
GAMMSUM2 = GAMMSUM2 + GAMM_AY/(DGAMM_AY**2)
GAMMSUM3 = GAMMSUM3 + (GAMM_AY/DGAMM_AY)**2
END IF
C
IF (DBOTH_AY .NE. 0.0) THEN
BOTHSUM1 = BOTHSUM1 + 1/(DBOTH_AY**2)
BOTHSUM2 = BOTHSUM2 + BOTH_AY/(DBOTH_AY**2)
BOTHSUM3 = BOTHSUM3 + (BOTH_AY/DBOTH_AY)**2
END IF
C
IF (DMON_AY .NE. 0.0) THEN
MONSUM1 = MONSUM1 + 1/(DMON_AY**2)
MONSUM2 = MONSUM2 + MON_AY/(DMON_AY**2)
MONSUM3 = MONSUM3 + (MON_AY/DMON_AY)**2
END IF
C
END IF

```

```

END DO
C
CLOSE (UNIT=2)
C
C !!!!!!!!!!!!!!!!!!!!!!!!!!!!!!!!!!!!!!!!!!!!!!!
C ! then calculate averages          !
C !!!!!!!!!!!!!!!!!!!!!!!!!!!!!!!!!!!!!!!!!!!!!!!
C
IF (NEUTSUM1 .GT. 0.0) THEN
MEAN_NEUT_AY=NEUTSUM2/NEUTSUM1 !Bevington 5-14
UNCERT_NEUT_AY=1/SQRT(NEUTSUM1) !Bevington 5-15
IF (N .GT. 1) THEN
STD_NEUT_AY=SQRT((NEUTSUM3*NEUTSUM1-NEUTSUM2**2)
    >/(N-1))/NEUTSUM1
ELSE
STD_NEUT_AY=0.0
END IF
ELSE
MEAN_NEUT_AY=0.0
UNCERT_NEUT_AY=0.0
STD_NEUT_AY=0.0
END IF
C
IF (GAMMSUM1 .GT. 0.0) THEN
MEAN_GAMM_AY=GAMMSUM2/GAMMSUM1 !Bevington 5-14
UNCERT_GAMM_AY=1/SQRT(GAMMSUM1) !Bevington 5-15
IF (N .GT. 1) THEN
STD_GAMM_AY=SQRT((GAMMSUM3*GAMMSUM1-GAMMSUM2**2)
    >/(N-1))/GAMMSUM1
ELSE
STD_GAMM_AY=0.0
END IF
ELSE
MEAN_GAMM_AY=0.0
UNCERT_GAMM_AY=0.0
STD_GAMM_AY=0.0
END IF
C
IF (BOTHSUM1 .GT. 0.0) THEN
MEAN_BOTH_AY=BOTHSUM2/BOTHSUM1 !Bevington 5-14
UNCERT_BOTH_AY=1/SQRT(BOTHSUM1) !Bevington 5-15
IF (N .GT. 1) THEN
STD_BOTH_AY=SQRT((BOTHSUM3*BOTHSUM1-BOTHSUM2**2)
    >/(N-1))/BOTHSUM1
ELSE

```

```

STD_BOTH_AY=0.0
END IF
ELSE
MEAN_BOTH_AY=0.0
UNCERT_BOTH_AY=0.0
STD_BOTH_AY=0.0
END IF
C
IF (MONSUM1 .GT. 0.0) THEN
MEAN_MON_AY=MONSUM2/MONSUM1 !Bevington 5-14
UNCERT_MON_AY=1/SQRT(MONSUM1) !Bevington 5-15
IF (N .GT. 1) THEN
STD_MON_AY=SQRT((MONSUM3*MONSUM1-MONSUM2**2)
>/(N-1))/MONSUM1
ELSE
STD_MON_AY=0.0
END IF
ELSE
MEAN_MON_AY=0.0
UNCERT_MON_AY=0.0
STD_MON_AY=0.0
END IF
C
C !!!!!!!!!!!!!!!!!!!!!!!!!!!!!!!!!!!!!!!!!!!!!!!!!!!!!!!!!!!!!!!!!!!!!!!
C ! write averages to file to give them to NEUTDUMP.COM !
C !!!!!!!!!!!!!!!!!!!!!!!!!!!!!!!!!!!!!!!!!!!!!!!!!!!!!!!!!!!!!!!!!!!!!!!
C
OPEN (UNIT=1,NAME='NEUTASYM.TMP',TYPE='NEW')
SCALE = 1.0
BWR1 = SCALE*MEAN_NEUT_AY
BWR2 = SCALE*UNCERT_NEUT_AY
BWR3 = SCALE*STD_NEUT_AY
WRITE (1,200) 'Main AY',BWR1,BWR2,BWR3
BWR1 = SCALE*MEAN_GAMM_AY
BWR2 = SCALE*UNCERT_GAMM_AY
BWR3 = SCALE*STD_GAMM_AY
WRITE (1,200) 'BCI AY ',BWR1,BWR2,BWR3
BWR1 = SCALE*MEAN_BOTH_AY
BWR2 = SCALE*UNCERT_BOTH_AY
BWR3 = SCALE*STD_BOTH_AY
WRITE (1,200) 'Canb AY',BWR1,BWR2,BWR3
BWR1 = SCALE*MEAN_MON_AY
BWR2 = SCALE*UNCERT_MON_AY
BWR3 = SCALE*STD_MON_AY
WRITE (1,200) 'Mon AY ',BWR1,BWR2,BWR3

```

```
200 FORMAT (a7,1x,F7.2,'+/-',F5.2,'( ',F5.2,')')
CLOSE (UNIT=2)
C
CALL SYS$EXIT(%VAL(1))
END
```

Bibliography

- [Abr61] A. Abragam. *Principles of Nuclear Magnetism*. Oxford University Press, 1961.
- [Ade96] B. Adeva et al. *Large enhancement of deuteron polarization with frequency modulated microwaves*. Nuclear Instruments and Methods in Physics Research, **A372**(1996) 339–343.
- [Bla03] T. C. Black, P. R. Huffman, W. M. Snow, K. Schoen, M. Arif, H. Kaiser, S. K. Lamoreaux, and S. A. Werner. *Precision Neutron Interferometric Measurement of the nd Coherent Neutron Scattering Length and Consequences for Models of Three-Nucleon Forces*. Physical Review Letters, **90**(2003) 192502-1–192502-4.
- [Bor71] M. Borghini and K. Scheffler. *A Butanol Polarized Deuteron Target*. Nuclear Instruments and Methods, **95**(1971) 93–98.
- [Car83] J. Carlson, V. R. Pandharipande, and R. B. Wiringa. *Three-nucleon interaction in 3-, 4-, and ∞ -body systems*. Nuclear Physics, **A401**(1983) 59–85.
- [Che86] C. R. Chen, G. L Payne, J. L. Friar, and B. F. Gibson. *Faddeev calculations of the 2π - $3N$ force contribution to the 3H binding energy*. Physical Review C, **33**(1986) 1740–1752.

- [Cle95a] T. B. Clegg, H. J. Karwowski, S. K. Lemieux, R. W. Sayer, E. R. Crosson, W. M. Hooke, C. R. Howell, H. W. Lewis, A. W. Lovette, H. J. Pfutzner, K. A. Sweeton, and W. S. Wilburn. *A New Atomic Beam Polarized Ion Source for the Triangle Universities Nuclear Laboratory: Overview, Operating Experience, and Performance*. Nuclear Instruments and Methods, **A357**(1995) 200–211.
- [Cle95b] T. B. Clegg, W. M. Hooke, E. R. Crosson, A. W. Lovette, H. L. Middleton, H. G. Pfutzner, and K. A. Sweeton. *ECR and cesium ionizer systems for the Triangle Universities Nuclear Laboratory atomic beam polarized ion source*. Nuclear Instruments and Methods, **A357**(1995) 212–219.
- [Coe83] H. T. Coelho, T. K. Das, and M. R. Robilotta. *Two-pion-exchange three-nucleon force and the ^3H and ^3He nuclei*. Physical Review C, **28**(1983) 1812–1828.
- [Coo79] S. A. Coon, M. D. Scadron, P. C. McNamee, B. R. Barrett, D. W. E. Blatt, and B. H. J. McKellar. *The Two-Pion Exchange Three-Nucleon Potential and Nuclear Matter*. Nuclear Physics, **A317**(1979) 242–278.
- [Coo81] S. A. Coon and W. Glöckle. *Two-pion-exchange three-nucleon potential: Partial wave analysis in momentum space*. Physical Review C, **23**(1981) 1790–1802.
- [Coo93] S. A. Coon and M. T. Peña. *Momentum and coordinate space three-nucleon potentials*. Physical Review C, **48**(1993) 2559–2575.
- [Cou93] G. R. Court, D. W. Gifford, P. Harrison, W.G. Heyes, and M. A. Houlden. *A high precision Q-meter for the measurement of proton polarization in polarized targets*. Nuclear Instruments and Methods in Physics Research, **A324**(1993) 433–440.
- [Cov02] Stephanie Covert and Sarah Schuster *unpublished*.
- [Cra97] D.G. Crabb and W. Meyer. *Solid Polarized Targets for Nuclear and Particle*

- Physics Experiments*. Annual Review of Nuclear and Particle Science, **47**(Dec 1997) 67–109.
- [deB76] W. de Boer. *Dynamic Orientation of Nuclei at Low Temperatures*. Journal of Low Temperature Physics, **22**(1976) 185–212.
- [Ede96] J. A. Eden and M. F. Gari. *Does the 3N force have a hard core?* Physical Review C, **53**(1996) 1510–1518.
- [Fro92] Georgio Frossati. *Experimental Techniques: Methods for Cooling Below 300 mK*. Journal of Low Temperature Physics, **87**(1992) 595–633.
- [Fuj57] J.-I. Fujita and H. Miyazawa. Progress in Theoretical Physics, **17**(1957) 360.
- [Glo96] W. Glöckle, H. Witała, D. Hüber, H. Kamada and J. Golak. *The three-nucleon continuum: achievements, challenges and applications*. Physics Reports, **274**(1996) 107–285.
- [Gou81] C. R. Gould, L. L. Holzswieg, S. E. King, Y. C. Lau, R. V. Poore, N. R. Robertson, and S. A. Wender. *The xSYS Data Acquisition System at Triangle Universities Nuclear Laboratory*. IEEE Trans. on Nucl. Sci., **NS-28**(1981) 3708–3714.
- [Hal98] G. M. Hale, 1998. Private Communication.
- [Ham81] O. Hamada, S. Hiramatsu, S. Isagawa, S. Ishimoto, A. Masaike, and K. Morimoto. *Analysis of Deuteron NMR Spectrum in Propanediol for Polarization Measurement*. Nuclear Instruments and Methods, **189**(1981) 561–568.
- [Hni94] V. Hnizdo. *Observables for polarized neutrons transmitted through polarized targets*. Physical Review C, **50**(1994) 2639–2642.
- [Hub98] D. Hüber and J. L. Friar. *The A_y puzzle and the nuclear force*. Physical Review C, **58**(1998) 674–685.
- [Jar74] J. J. Jarmer, J. C. Martin, G. G. Ohlsen, G. C. Salzman, and J. E. Simmons.

- Longitudinal Polarization Transfer in the ${}^3\text{H}(\vec{p}, \vec{n}){}^3\text{He}$ Reaction.* Physics Letters, **48B**(1974) 215–217.
- [Kei94] C. D. Keith. *Total Cross Section Measurements for the Scattering of Polarized Neutrons from Polarized ${}^3\text{He}$.* Ph.D. thesis, North Carolina State University, 1994.
- [Kru79] M. Krumpolc and J. Roček. *Synthesis of Stable Chromium(V) Complexes of Tertiary Hydroxy Acids.* Journal of the American Chemical Society, **101:12**(1979) 3206–3209.
- [Leo94] W. R. Leo. *Techniques for Nuclear and Particle Physics Experiments.* Springer-Verlag, Berlin, 1994.
- [Lin] Link Analytical, Limited, Bucks, England. *Pulse Shape Discriminator and Gated Integrator, Model 5020.*
- [Lis75] P. W. Lisowski, R. L. Walter, C. E. Busch, and T. B. Clegg. *Polarization Transfer in the ${}^2\text{H}(\vec{d}, \vec{n}){}^3\text{He}$ Reaction at $\theta = 0^\circ$.* Nuclear Physics, **A242**(1975) 298–308.
- [Lou79] O. V. Lounasmaa. *Dilution Refrigeration.* Journal of Physics E: Scientific Instruments, **12 No. 8**(1979) 668–674.
- [Mac69] Malcolm H. MacGregor, Richard A. Arndt, and Robert M. Wright. *Determination of the Nucleon-Nucleon Scattering Matrix. X. (p,p) and (n,p) Analysis from 1 to 450 MeV.* Physical Review, **182**(1969) 1714–1728.
- [Mac89] R. Machleidt. *The Meson Theory of Nuclear Forces and Nuclear Structure.* Advances in Nuclear Physics, **19**(1989) 175–217.
- [Mac01] R. Machleidt. *High-precision, charge-dependent Bonn nucleon-nucleon potential.* Physical Review C, **63**(2001) 1–32.
- [Mar99] D. M. Markoff, R. D. Foster, C. R. Gould, D. G. Haase, J. O. Poole, B. W. Raichle, and W. Tornow. *Preliminary Measurements of the Longitudinal*

- $\vec{n} - \vec{d}$ Total Cross Section Difference. Triangle Universities Nuclear Laboratory Progress Report XXXVIII 1998–1999, pages 31–32.
- [Mar02] D. M. Markoff, R. D. Foster, C. R. Gould, D. G. Haase, J. O. Poole, B. W. Raichle, and W. Tornow. $\vec{n} - \vec{d}$ Scattering Measurements with the TUNL Dynamically Polarized Deuteron Target. In Vladimir P. Derenchuk and Barbara von Przewoski, editors, *Proceedings of the Ninth International Workshop on Polarized Sources and Targets*, pages 344–348, Indiana, 2002. World Scientific, Singapore.
- [Nog97] A. Nogga, D. Hüber, H. Kamada, and W. Glöckle. Triton Binding Energies for Modern NN Forces and the $\pi - \pi$ Exchange Three-Nucleon Force. *Physics Letters B*, **409**(1997) 19–25.
- [Ord92] C. Ordóñez and U. van Kolck. Chiral lagrangians and nuclear forces. *Physics Letters*, **B 291**(1992) 459–464.
- [Rai97] B. W. Raichle. *A Dynamically Polarized Proton Target for Measurements of the Transverse Spin-Dependent Total $\vec{n} - \vec{p}$ Cross Section Difference, $\Delta\sigma_L$* . Ph.D. thesis, North Carolina State University, 1997.
- [Ric88] R. C. Richardson and E. N. Smith. *Experimental Techniques in Condensed Matter Physics at Low Temperatures*. Addison-Wesley Publishing Company, 1988.
- [Sal73] G. C. Salzman, J. C. Martin, J. J. Jarmer, J. E. Simmons, Gerald G. Ohlsen, and T. R. Donoghue. Longitudinal Polarization Transfer in the ${}^2\text{H}(\vec{d}, \vec{n}){}^3\text{He}$ Reaction at 0° . *Physics Letters*, **45B**(1973) 123–126.
- [Sat83] G. R. Satchler. *Direct Nuclear Reactions*. Oxford University Press, 1983.
- [Sch71] P. Schwandt, T. B. Clegg, and W. Haeberli. Polarization Measurements and Phase Shifts for p - ${}^4\text{He}$ Scattering Between 3 and 18 MeV. *Nuclear Physics*, **A163**(1971) 432–448.

- [Spe87] F. Sperisen. *Extracting the Deuteron Target Polarization from the Magnetic Resonance Signal Line Shape*. Nuclear Instruments and Methods in Physics Research, **A260**(1987) 455–462.
- [Sto93] V. G. J. Stoks, R. Timmermans, and J. J. de Swart. *Pion-nucleon coupling constant*. Physical Review C, **47**(1993) 512–520.
- [Sto94] V. G. J. Stoks, R. A. M. Klomp, C. P. F. Terheggen, and J. J. de Swart. *Construction of high-quality NN potential models*. Physical Review C, **49**(1994) 2950–2962.
- [Tor03] W. Tornow, 2003. Private Communication.
- [VdG60] R. J. Van de Graaff. *Tandem Electrostatic Accelerators*. Nuclear Instruments and Methods, **8**(1960) 195–202.
- [vdB90] B. van den Brandt, J. A. Konter, and S. Mango. *A Compact Versatile Dilution Refrigerator with Top Loading Capability*. Nuclear Instruments and Methods in Physics Research, **A289**(1990) 526–531.
- [Wal98] J. R. Walston. *Determination of the Nucleon-Nucleon Tensor Force Through \vec{n} - \vec{p} Scattering Measurements*. Ph.D. thesis, North Carolina State University, 1998.
- [Wir95] R. B. Wiringa, V. G. J. Stoks, and R. Schiavilla. *Accurate nucleon-nucleon potential with charge-independence breaking*. Physical Review C, **51**(1995) 38–51.
- [Wit98] H. Witała, W. Glöckle, D. Hüber, J. Golak, and H. Kamada. *Cross Section Minima in Elastic Nd Scattering: Possible Evidence for Three-Nucleon Force Effects*. Physical Review Letters, **81**(1998) 1183–1186.
- [Wit99] H. Witała, W. Glöckle, J. Golak, D. Hüber, H. Kamada, and A. Nogga. *Scaling properties of the longitudinal and transversal asymmetries of the $\vec{n}\vec{d}$ total cross section*. Physics Letters B, **447**(1999) 216–220.